NTNU
Norwegian University of
Science and Technology

Fault-sill interaction: Implications for magma routing and overburden faulting in the Vøring Basin, Norwegian North Sea.

Einstein Sintong Anugrah Siregar

Preface

This thesis is submitted for the partial fulfilment of a Master Degree (Msc) in Petroleum Geosciences, specializing in Petroleum Geology during the spring semester of 2017 at the Norwegian University of Science and Technology. It mainly describes the complexity of fault, sill, and hydrothermal vent interaction in the Naglfar Dome, northernmost of the Vøring Basin.

Einstein Sintong Anugrah Siregar

Abstract

The role of pre-existing faults during magma transport and routing in the subsurface have received limited study in comparison with the dynamics, mechanisms and overall geometries of faults and magmatic sills. Seismic reflection data has allowed the full dimensionality of magmatic sills to be studied in the last few decades. However, seismic data has major drawbacks as it relates to the resolution and thickness of magmatic intrusions. To understand the connection between pre-existing faults, magmatic sills, post-emplacement faults and hydrothermal vents, this thesis has used a high-resolution, high-quality, 3-D seismic reflection data located in the Naglfar Dome, Vøring Basin, to provide detailed information on the process of magma routing through faults and how magmatic intrusions can create overburden faulting. Magmatic sills in the study area are positive high amplitude anomalies with similar polarity as the seabed reflection. The sills have saucer, transgressive and concave-up geometries occurring at three principal stratigraphic intervals but importantly formed an interconnected sill complex at depth of about -5000 ms TWTT. Sill-sill interactions are identified based on sill-sill junction types. Area coverage of magmatic sills in this study area ranges from 15.2 to 94.3 km^2 for shallow sills, 8.8 to 186.4 km^2 for intermediate sills and 48.4 to 186.4 km^2 for the deeper sills. There is evidence for lateral migration of sills for longer distances upon ascent from the magma chamber.

To understand the importance of fault-sill interactions, 136 faults associated with magmatic sills were interpreted and studied for their throw-depth (T-z) and displacement (D-x) characters. Magmatic sills in the Naglfar Dome show disparate relationship with faults. At fault-sill junctions, C-type junctions are predominant. The propagation of magma through pre-existing faults causes formation of inclined sheets, intrusive steps, and reorientation of magma flow along faults' strike. Thirteen magmatic sills associated with hydrothermal vents in the study area have eye-, dome-, crater-, and pyramid-shaped upper parts. Vertical ascent of hydrothermal fluids caused local perturbation of the stress state within the overlying polygonal faults creating radial faults at the tops of the vents.

This thesis describes the complexity of fault-sills interaction in magma-rich basins and represents a good case study to understand the role of faults during subsurface magma plumbing. This thesis has broader implications for regional tectonic history, mineral exploration and hydrocarbon prospectivity.

Acknowledgement

~ For everything there is a time ~

Table of Contents

List of Figures

Chapter 5: Discussions and Conclusions

List of Tables

Chapter 1

Introduction

1.1 Background to the study

Over the past decades, significant studies have proved that pre-existing structures within magma-rich continental margins are one of the major channels for magma emplacement (Joppen and White, 1990; Schofield et al., 2012; Magee et al., 2013b; Magee et al., 2013c; Magee et al., 2016). These structures can also influence the geometry of the intrusive rocks either by reorienting magma direction to become orthogonal to fault strike (Magee et al., 2013b), or classifying the intrusive into brittle or non-brittle processes (Schofield et al., 2012). In the short-term, the emplacement of the intrusive rocks may influence basin deformation, host-rock alteration due to gas and fluid interaction, and triggered fluid eruptions creating hydrothermal vent formations (Planke et al., 2005). While in the long term, the emplacement of magma may create compartments that may become impediments for hydrocarbon migrations (Planke et al., 2005; Holford et al., 2012; Magee et al., 2013c).

Consequently, shortly after the emplacement of the intrusive, fluid overpressure may occur due to the interaction between the molten magma and the sedimentary host rock, which may ultimately initiate an expulsion process leading to the formation of hydrothermal vents (Jamtveit et al., 2004; Hansen and Cartwright, 2006a). Expulsion may increase the vertical stress provoking the formation of radial and crestal faults. To date, the character of crestal and keystone faults formed through such process remains barely investigated (Omosanya et al., in press). On the contrary, significant investigation has over the past decade been devoted to studies of such radial and crestal faults associated with salt-diapirs and stocks (Carruthers et al., 2013).

Propagation of intrusive dikes are considered to transform into intrusive sills, after the dike crosscuts a stress or perturbation barrier, such as a strong unit or oddity unit (Bédard et al., 2012). Beyond the tip of the intrusive is thought to contain such a pressure as the result of the emplacement that may generate tensile stress which is sufficient to create structures in the host-rock unit (Delaney et al., 1986). While on each side or near to the tip of the intrusive, the pressure is sufficient enough to generate tensile maxima (Delaney et al., 1986). As the stress increases, the structures near the intrusive are considered to increase (Delaney et al., 1986).

Consequently, the magma may invade the older structures at the time of intrusion with respect to the principal stress direction, or will create its own hydraulic 'new structures' that are perpendicular to the least compressive stress orientation (Delaney et al., 1986). The invasion of magma within the older structures is considered to occur depending on two mechanisms: if the lateral principal stresses are less than the magmatic driving pressure, and if the structures are almost perpendicular to the orientation of least compressive regional stress. However, if the older structures are absent, the pervasive magma must fill the 'new structures' (Delaney et al., 1986).

At different stages, the channel for magma invasion may have opened periodically during the propagation of new intrusive magma from the mantle (Bédard et al., 2012). This invasion may breach the overlying strata or reactivate the primitive structures, hence elevating the sill roof and opening the fault channel, allowing magma to invade to higher sequences (Bédard et al., 2012). At the first stage, the channel may have to narrow for large amount of magma to transport upwards, therefore only partial amounts are able to ascend (Bédard et al., 2012). Such a situation would have built up the magma pressure, widening the channel and allowing a large amount of magma to accumulate (Bédard et al., 2012). Through time, the channel may close as the time of magmatic flux shrinks, and the pressure in the channel lessens (Bédard et al., 2012). The other mechanism may relate to the merging of different fault systems that could trigger the excision or obliteration of the channel systems. Hence, it is imperative to understand the role of pristine structures during magma emplacement.

To understand the processes leading to the formation of several fault families around magmatic rocks and the role of primitive structures during magma routing, this thesis has chosen a natural laboratory where several evidences for magmatic emplacement have been documented. The emplacement of multiple magmatic sills in the Naglfar Dome, on the mid-Norwegian continental margin during opening of the Norwegian-Greenland Seas in the Early Cenozoic (Lundin and Doré, 2002), makes it a suitable case study area to test the interaction between pre-existing basinal structures and how these control the routing of magma during continental break-up. Previous authors in the proposed study area suggested that at least two periods of magmatic intrusive occurred in the region during Late Palaeocene and Early Eocene, both related to extensional events during the opening of the Norway and Greenland Seas (Hansen, 2004; Cartwright and Hansen, 2006; Hansen and Cartwright, 2006a).

1.2 Research questions

The aims of this thesis are to perform a detailed three-dimensional seismic interpretation and analysis of magmatic sills and hydrothermal vents, and their relationship with fault systems. On the basis of the research aims and review of previous research works, the following research questions are proposed:

- How are polygonal, radial and crestal faults associated with magmatic rocks formed?
- What are the characters of magmatic sills and hydrothermal vents emplaced or formed adjacent to fault systems?
- How can the timing of magmatic intrusions and formation of hydrothermal vents be established?

1.3 Aims and objectives of the study

The overall aim of this thesis is to investigate the interaction between magmatic sills, hydrothermal vents and fault systems within the Naglfar Dome, Northern Vøring Basin, in order to recognize their characteristic, nature, distribution, and implication for basin history. These overall aims are performed by addressing several key objectives as follows:

1. To account for the typical geometrical style of the magmatic sills and hydrothermal vents on three-dimensional seismic data.
2. To characterize the interrelationship between magmatic sills and hydrothermal vents facilitated by fault systems.
3. To discuss the controls behind the emplacement of magmatic sills and morphologies of hydrothermal vents.
4. To evaluate the implication of these magmatic processes for hydrocarbon prospectivity in the Northern part of the Vøring Basin.

1.4 Location of the study area

Geographically, the Vøring Basin is situated in the mid-Norwegian continental margin between latitude 62° and 69° (Figure 1.1a), dominated by deep Cretaceous sequences and several magmatic rocks e.g., sills (Figure 1.1b). The geodynamic evolution of the mid-Norwegian continental margin is linked to extension events related to the breakup of the Norway and Greenland Seas in Late Palaeocene and compressional events in Early Eocene to Oligocene, leading to the formation of several Paleogene domes in the Vøring Basin (Lundin and Doré, 2002; Mjelde et al., 2003; Faleide et al., 2008). Following continental breakup, series of

magmatic rocks are believed to have been emplaced into the Cretaceous sequence in the Vøring Basin.
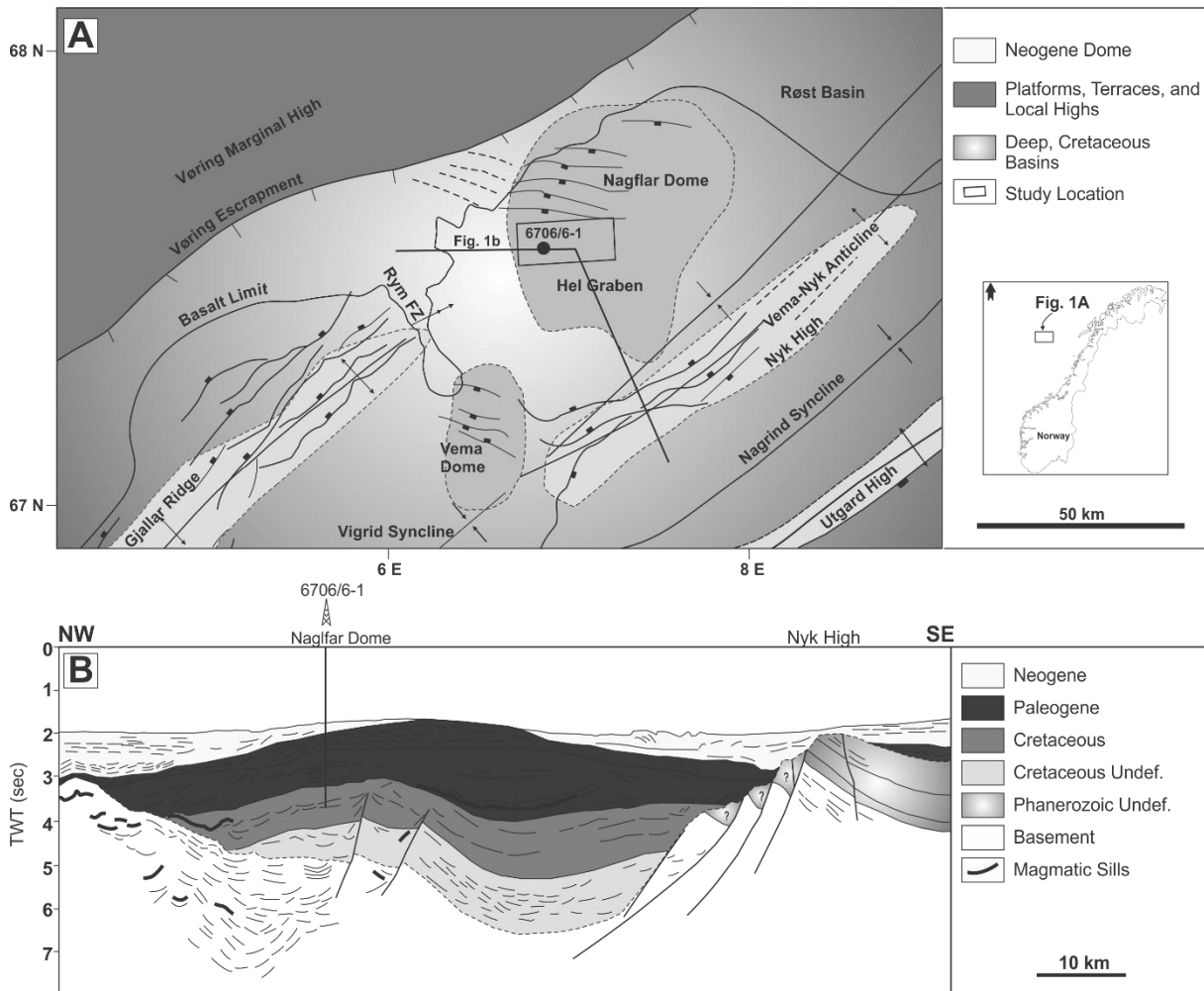
Figure 1.1 – (A) Geographical context of the study area (Modified after Lundin et al. (2013)). (B) Seismic profile across Naglfar Dome (SE Hel Graben) and Nyk High with well 6706/6-1 (Modified after Lundin et al. (2013)).

The study area is the Naglfar Dome, located at the northernmost part of the Vøring Basin (Figure 1.1a). The Naglfar Dome was proposed to be collapsed in Palaeocene, comprised an unusual thick Palaeocene sequences with pervasive emplacement of magmatic sills (Lundin et al., 2013) (Figure 1.1b), and experienced tectonic inversion in Middle Miocene (Doré et al., 2008). The borehole 6706/6-1 in the study area revealed that the lithostratigraphy extend from the Quaternary Naust Formation to Cretaceous Nise Formation (Omosanya et al., 2017).

1.5 Structure of the thesis

The thesis is divided into five chapters (Figure 1.2). Chapters 1 and 2 are introduction to the thesis and literature review highlighting the tectonic evolution of the study area. Chapter 3 deals with the methods used in the thesis while the results and interpretation of the findings from the study are presented in Chapter 4. Chapter 5 contains discussion and conclusions of the overall study.
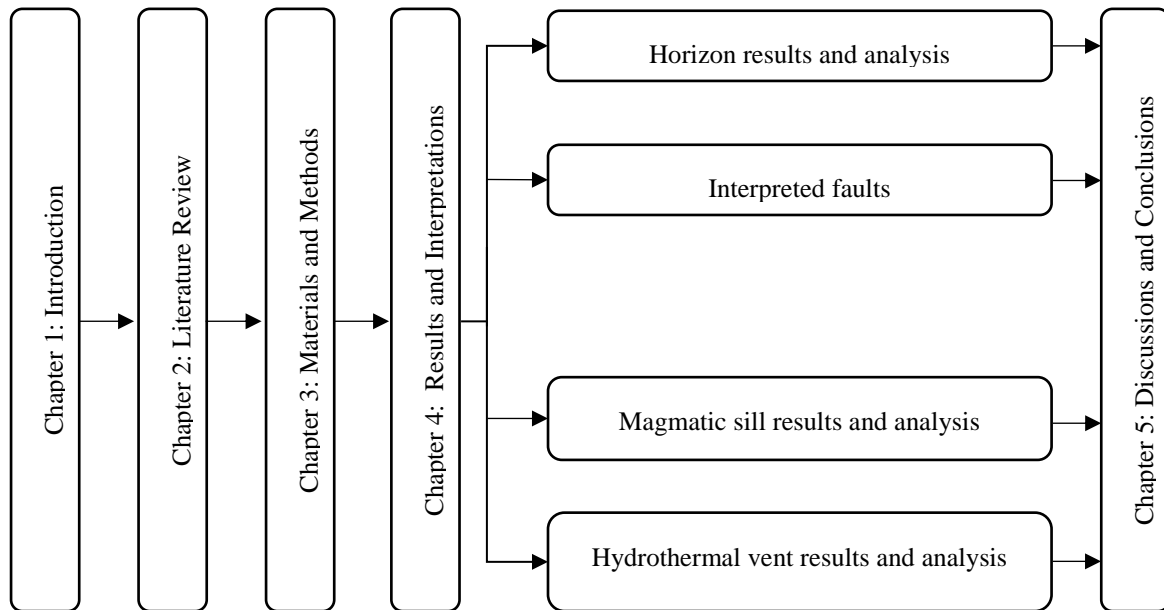
Figure 1.2 – The structure of the thesis.

Chapter 2

Literature Review

2.1 Geology of the study area

The area between latitude 62° and 69° N in the mid-Norwegian continental margin comprises a central province of deep Cretaceous basins, the Møre and Vøring Basins (Brekke et al., 1999). Geologically, the Vøring Basin is a large sedimentary basin that consists of structural highs, grabens, and sub-basins (Skogseid et al., 1992b). To the west, the Vøring Basin is delimited by the Vøring Escarpment, and the Vøring Marginal High, and to the east by the Trøndelag Platform and fault complexes (Brekke, 2000). In general, the Vøring Basin is divided by the Fles Fault Complex and the Bivrost Lineament to the north, and by the Jan Mayen Lineament to the south (Blystad et al., 1995; Travis et al., 1995; Brekke, 2000). The other important structure boundaries within the Vøring Basin are the Surt Lineament, which include the Rym Fault Zone. These lineaments are parallel to the Bivrost and Jan Mayen Lineaments with NW-SE trending (Blystad et al., 1995; Travis et al., 1995; Brekke, 2000). Brekke (2000) documented the evolution of the Vøring Basin into three main episodes: Mid-Jurassic to Late Cenomanian, Late Cenomanian to Early Palaeocene, and Early Palaeocene to the present (Figure 2.1). The geological evolution of the Vøring Basin is discussed below:

Late Mid-Jurassic to Late Cenomanian

The Fles Fault Complex is structurally important in the tectonic development of the region since Early Cretaceous (Brekke, 2000). The Fles Fault Complex presumably originated as a Mid- to Late Jurassic complex of normal fault complex (Brekke, 2000). The western part of the Flex Fault Complex consisting the present Någrind and Vigrid Synclines, the Hell Graben, and the Nyk High, coalesced into a single complex of Early Cretaceous Basin and is shallower than the Rås and Træna Basins (Brekke, 2000). Brekke (2000) stated that the western flank of the Early Cretaceous Basin was situated in the present area of the Gjallar Ridge. A shallower correlation of the Lower Cretaceous sequence to the west of the Fles Fault Complex typically showing a regional high, is known as Fulla Ridge (Eldholm et al., 1989; Skogseid et al., 1992a; Skogseid et al., 1992b). Furthermore, Brekke (2000) concluded that the Early Cretaceous Basin typically established as the result of thermal subsidence after a series of rifting events in the late Mid Jurassic to Early Cretaceous.

Late Cenomanian to Early Palaeocene

During the second episode, the amalgamation of the Halten and Dønna Terraces and several Early Cretaceous basins into one basin established the Vøring Basin (Blystad et al., 1995; Travis et al., 1995; Brekke, 2000). Westward of the Vøring Basin, the Gjallar Ridge was established in the Late Cenomanian to Early Turonian period. During this period, extensional system produced rotated fault blocks that are reflected as ridges, while the Revallet Fault Complex had established the eastern fault boundary of the Vøring Basin (Brekke, 2000). In Late Cretaceous, the Surt Lineament in the northern part of the Vøring Basin was an important structure (Dalland et al., 1988). The post-Cenomanian sequence in the Nyk High, the Hel Graben, and the Någrind Syncline generally has a constant thickness indicating that the Surt Lineament was a major depocentres in the period of Cenomanian to latest Campanian-Maastrichtian before the synclines and highs were established (Brekke, 2000). In the southern part of the Surt Lineament, compression and reactivation of the Fles Fault Complex had created an anticline in the central part of the Vøring Basin. The anticline was bounded by the Vigrid Syncline in western part and by the Rås Basin in the east (Brekke, 2000). In the northern part of the Surt Lineament, the Vøring Basin was structurally folded into NW-SE trending synclines i.e., the Någrind Syncline, the Hel Graben, and the Træna Basin and was divided by two anticlines, the Utgard and Nyk Highs, during Late Cretaceous extension and subsequent compression (Brekke, 2000). During the Mid-Jurassic, deposition into the western part of Halten Terrace initiated uplift and erosion in the western part of the Vøring Basin (Gjelberg et al., 1987; Brekke, 2000). At the end of the Cretaceous, the Nordland Ridge, the Utgard High, the Nyk High and the central anticline in the Fles Fault Complex may have been eroded and the Vøring Basin was uplifted at the beginning of the Palaeogene.

Early Palaeocene to the present.

Through most of the Palaeocene, uplift in the Vøring Basin continued allowing erosion of the higher areas. The Gjallar Ridge in the west, and the Nyk High, the Nordland Ridge, and north of Råd Basin to the east were eroded and onlapped by the Palaeocene and younger sediments (Brekke, 2000). During the Paleogene, the major events include deposition in the western part of the Vøring Basin, flanked by the Vøring Escarpment and reactivation of Fles Fault Complex, Jan Mayen, and Surt Lineaments in the west (Brekke, 2000). Tectonic extension during the Maastrichtian-Palaeocene initiated the separation of the continent and breakup of Norwegian and Greenland Seas (Skogseid et al., 1992b; Blystad et al., 1995; Brekke, 2000). The Vøring

Escarpment was initiated in Eocene as a result of tectonic reactivation of major lineaments and fault complexes (Brekke, 2000).

PERIOD				AGE	BREKKE (2000)	LUNDIN (2013)
Quaternary						
Neogene			Pliocene	10		Compressional Inversion: Nadlfar & Vema Domes
				20		
			Oligocene		Uplift: Vøring Marginal High, Bivrost, Jan Mayen Lineaments, and Lineaments, Fles Fault Complex	
Paleogene			Eocene	30		
				40		
				50	Break-up NE Atlantic: Sill, dikes, lava	Break-up NE Atlantic: Sill, dikes, lava
			Paleocene	60		Extensional Collapse: Hel Graben, Nyk High & Gjallar Ridge
Cretaceous	Late		Maastrichtian	70	Uplitft Vøring Basin	
			Campanian	80	Compressional and reactivation: Anticline in Fles Fault Complex	Compressional Inversion: Vema-Nyk Anticline & Någrind Syncline
			Conacian			
			Turonian	90	Extensional system: Gjallar Ridge	
			Cenomian	100		Compressional Inversion NE Greenland, W Barents Sea:
	Early		Albian	110		
			Aptian	120		Onset regional compression?: Vigrid Syncline, Gjallar Ridge & Utgard High
			Barremian	130		
			Hauterivian			
			Valanginian	140	Extensional NE Atlantic: Vøring Basin	Hyperextension NE Atlantic: Vøring Basin
			Berriasian			

Figure 2.1 – Geodynamic evolution of the Vøring Basin (Re-drawn from Brekke (2000) and Lundin et al. (2013)).

The Vøring Marginal High experienced further uplift in the latest Eocene-Early Oligocene and in the Late Miocene. At the same time, the Bivrost and Jan Mayen Lineaments, the Surt Lineament, and the Fles Fault Complex were established. Reactivation of faults and lineaments in the Vøring Basin during Eocene-Miocene resulted in the establishment of the Vema Dome, Naglfar Dome, the Helland-Hansen and Modgun Arches, and domes in the Træna Basin (Blystad et al., 1995; Brekke, 2000). Related to Norway and Greenland separation, the Vøring Basin experienced a magmatic event for about ~3 Ma which produced massive extrusive material in more than 2,600 km throughout the Early Palaeogene (Eldholm, 1991; Skogseid et al., 1992a). Uplift and erosion continued in the Norwegian mainland during Neogene and was

followed by sedimentation of Pliocene-Pleistocene sediments that create the present shelf edge (Blystad et al., 1995; Brekke, 2000).

2.2 Lithostratigraphy of the study

Stratigraphic formations in the Vøring Basin reflects an important information about the pre-Cenozoic intracontinental basin evolution in the mid-Norwegian continental margin. Strong reflectors in the deeper formation of the Vøring Basin indicate large-scale magmatic sills that were emplaced at about ~3 Ma consequent to continental breakup between Norway and Greenland (Skogseid et al., 1992a; Eldholm and Grue, 1994; Brekke, 2000; Lundin et al., 2013). Stratigraphic data from well 6706/6-1 provide information about four main formations in the study area (Figure 2.2):

Naust Formation

Uplift and glaciation at Late Pliocene-Pleistocene indicate that deep glacial erosion had removed 1-2 km of cover from the Norwegian onshore. The products of this erosional event were deposited as a wedge of glacio-marine sediments or Naust Formation (Riis and Fjeldskaar, 1992). Generally, the Naust Formation is characterized by clay-rich diamicton that is interbedded with medium-coarse grained sands (Eidvin et al., 1998). Riis and Fjeldskaar (1992) suggest that the Pliocene-Pleistocene sediments have triggered shale diapirism in the deeper part of the Vøring Basin.

Kai Formation

The distribution of the Kai Formation in the Vøring Basin is typically characterized by thinning to the east and thickening to the western part of the Vøring Basin. The Kai Formation is Early Miocene to Late Palaeocene in age, and was deposited in a marine setting. The Kai Formation comprises claystone, siltstone, and sandstone with blocky limestone. Pyrite, glauconite, and shell fragments are also recorded in this formation (Dalland et al., 1988).

Brygge Formation

The sediments of the Brygge Formation were deposited during the period from 36 Ma to 25 Ma. During this time, tectonic compression took place in the mid-Norwegian continental margin (Swiecicki et al., 1998). Dalland et al. (1988) stated that the Brygge Formation mainly contains claystone with minor sandstone, limestone, siltstone, and marl. These lithologies indicate that the Brygge Formation was deposited under marine conditions.
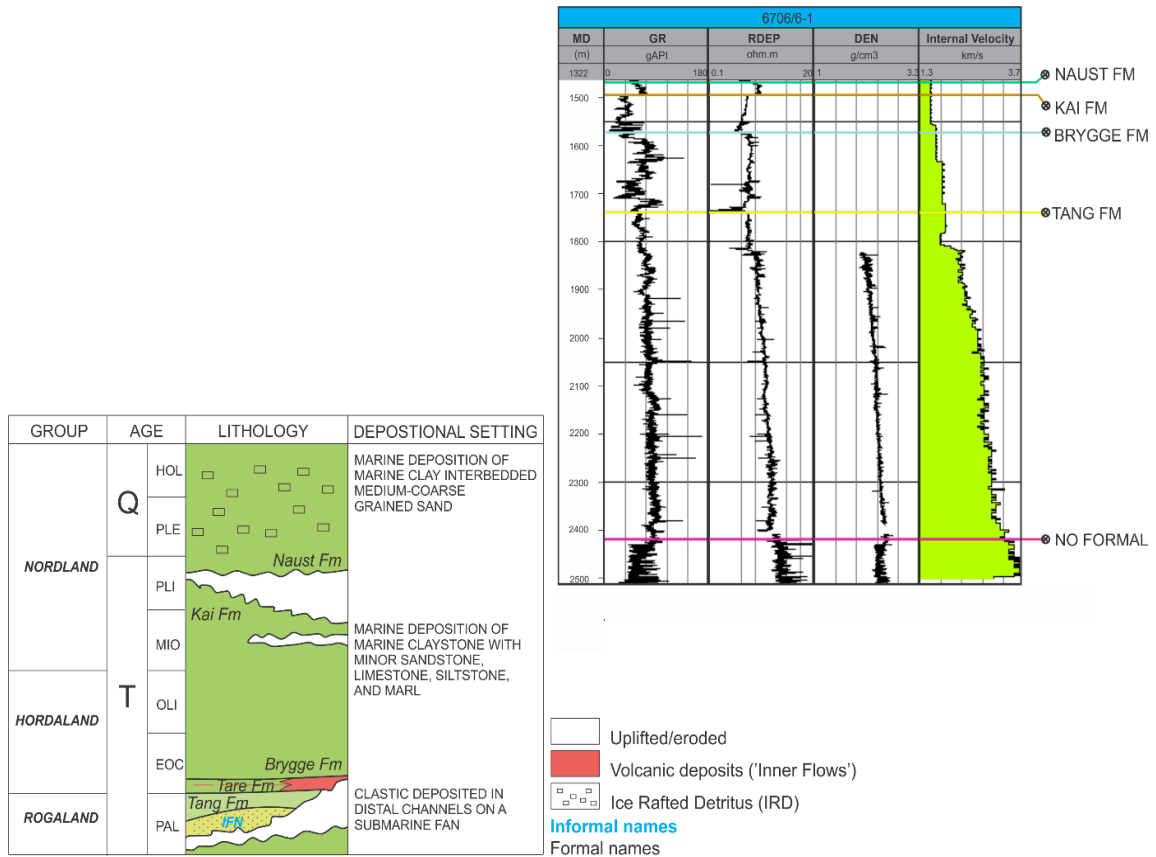
Figure 2.2 – Lithostratigraphic chart of the study area (Modified from NPD (2015)).

Tang Formation

The Late Palaeocene Tang Formation included in Egga member that was deposited in a deep marine environment (Martinsen and Dreyer, 2001; Hansen et al., 2011). The Tang Formation contains mainly sand with turbidite sandy mudstones thinning upwards, which represent distal channels on a submarine fan (Martinsen and Dreyer, 2001).

2.3 Tectonic evolution of the study area

The evolution of the Vøring Basin is inevitably connected to the evolution of the Mid-Norwegian continental margin. The margin is part of the NE Atlantic margin, which covers an area of about 150,000 km^2 with the sedimentary cover ranging in age from Late Palaeozoic to Cenozoic (Bukovics and Ziegler, 1985). The tectonic evolution of the Mid-Norwegian continental margin has been summarized by Brekke (2000). The tectonic events on the margin started with the Caledonian Orogeny that had two orogenic events: the Finnmarkian (Late Ordovician) and the Scandian (Late Silurian – Early Devonian). The Caledonian Orogeny was the result of continental convergence between the Laurentian and Fennoscandian plates. Brekke et al. (1999) identified three periods of rifting in the mid-Norwegian Sea continental margin to

include Carboniferous to Permian, Late Mid-Jurassic to Early Cretaceous, and Late Cretaceous to Early Eocene.
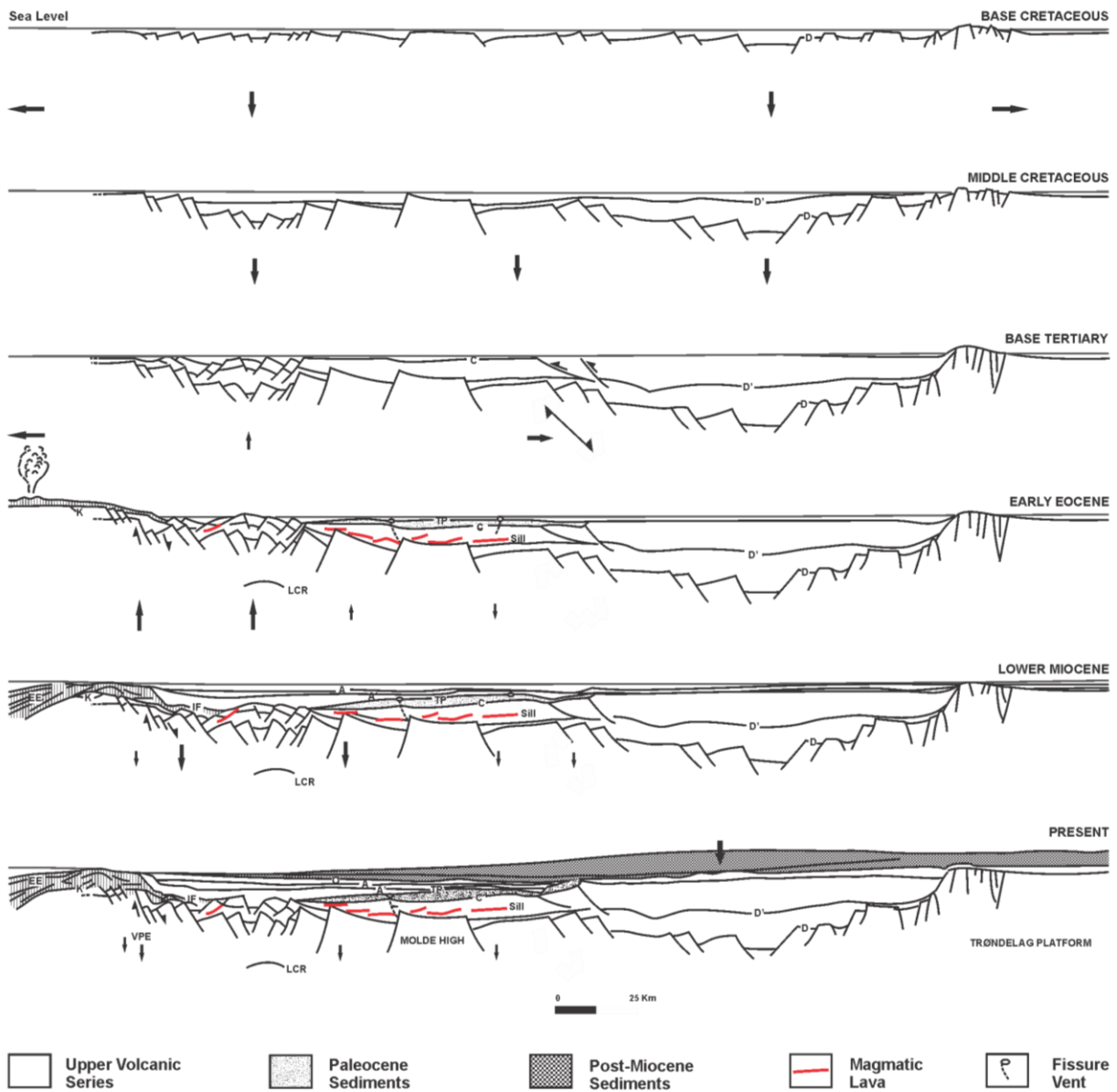
Figure 2.3 – The development of the Vøring Basin from Cretaceous to Cenozoic time (Redrawn from Eldholm et al. (1989)).

Extensional tectonics in the Carboniferous-Early Cretaceous are associated with the continental rifting, and in Late Cretaceous- Early Eocene was connected with the breakup and continental separation between Norway and Greenland (Eldholm et al., 1989; Eldholm, 1991; Skogseid et al., 1992a; Brekke, 2000) (Figure 2.3).

The two tectonic phases i.e., the Late Jurassic-Early Cretaceous followed by the Early Cenozoic rifting governed the structural and subsidence history of the Vøring Basin (Skogseid et al., 1992a). The extensional event during Late Jurassic-Early Cretaceous reactivated older structures to create rotated fault blocks in the basin (Eldholm et al., 1989; Skogseid et al., 1992b), while extension in Late Jurassic-Early Cretaceous had produced syn-tectonic listric faults in the basin (Skogseid et al., 1992a). The extensional events were followed by magmatic emplacement in the lower crust and uplift of the asthenosphere, accompanied by erosion and redeposition of sediments on the basin edge (Eldholm et al., 1989). During Palaeogene and Neogene, the Vøring Basin and the Norwegian mainland experienced intense uplift and erosion. These conditions favored the deposition of Pliocene-Pleistocene sediments in the western part into the shelf edge (Skogseid et al., 1992a).

2.4 Petroleum systems of the study area

In the Vøring Basin, the presence of gas has been found in several wells, but only minor oil presence. Brekke et al. (1999) stated that the source rock in this basin may be associated with water circulation from two different phases. The first phase during the Early Cretaceous in the Hel and Fenris Grabens and a second phase in the Palaeocene-Early Eocene at the time when the Vøring Basin was closed to Lofoten and Vesterålen (Skogseid et al., 1992a). The Jurassic and Early Cretaceous layers are too deep as hydrocarbon plays, except on the Vøring Marginal High has possible hydrocarbon accumulations beneath the Palaeogene sills (Brekke et al., 1999). The most promising reservoirs are the Turonian, Coniacian, and Early Campanian sandstones that are trapped in rotated fault block. The second promising reservoirs could be found in the Vema Dome, the Nyk High, Någrind and Vigrid Synclines which are associated with the Early Palaeocene sandstones (Brekke et al., 1999; Kittilsen et al., 1999). The massive magmatic activity in Paleogene in the Vøring Basin has probably altered the reservoir quality (Brekke et al., 1999). Rapid subsidence and deposition of marine shales during Late Paleogene-Neogene on the western part of the Vøring Basin led to the formation of cap rocks in this basin, whereas the traps are generally associated with Eocene-Miocene compressional domes and stratigraphic closure (Brekke et al., 1999).

2.5 Magmatic rocks in sedimentary basins

The following section briefly summarizes the character of magmatic intrusions, hydrothermal vents, crestal and radial faults based on previous research works.

2.5.1 Magmatic sills

2.5.1.1 Magmatic rocks on seismic reflection data

On seismic data, the density and compressional sonic velocity of intrusive rocks are high, compared to sedimentary rocks. These physical differences at the intrusion–host rock contacts result in a high acoustic impedance contrast (Smallwood and Maresh, 2002; Hansen, 2004; Planke et al., 2005; Hansen and Cartwright, 2006b; Hansen and Cartwright, 2006a; Thomson, 2007; Magee et al., 2013a; Magee et al., 2016), which reflects more seismic energy back to the surface than low impedance boundaries typically between sedimentary rocks (Brown, 2004). Hence, on seismic data, igneous bodies/magmatic sills are commonly expressed as high-amplitude reflections (e.g., Frey et al., 1998; Smallwood and Maresh, 2002; Planke et al., 2005; Magee et al., 2015). Seismic-stratigraphic relationships of high-amplitude reflections can be used to determine if they have an igneous origin or not. In particular, high-amplitude reflections attributed to igneous intrusions are commonly restricted in their lateral continuity and/or crosscut the host-rock strata (e.g., Mihut and Müller, 1998).

2.5.1.2 Sill Geometry

The geometry and attitude (Figure 2.4) of magmatic intrusions mainly depend on their relationship to the invaded rock formations and pre-existing structural complexity within basins (Duff and Duff, 1993). The molten magma is transported through fractures into the upper brittle crust to form tabular igneous bodies which are dis-concordant or concordant to the overlying formations (Hansen, 2004). Most magmatic intrusions in the crust are in the form of sheet-shaped bodies with a length of meters up to kilometers and thickness of several meters. Examples include laccoliths, plutons, stocks, and crypto-domes (Mathieu et al., 2008).
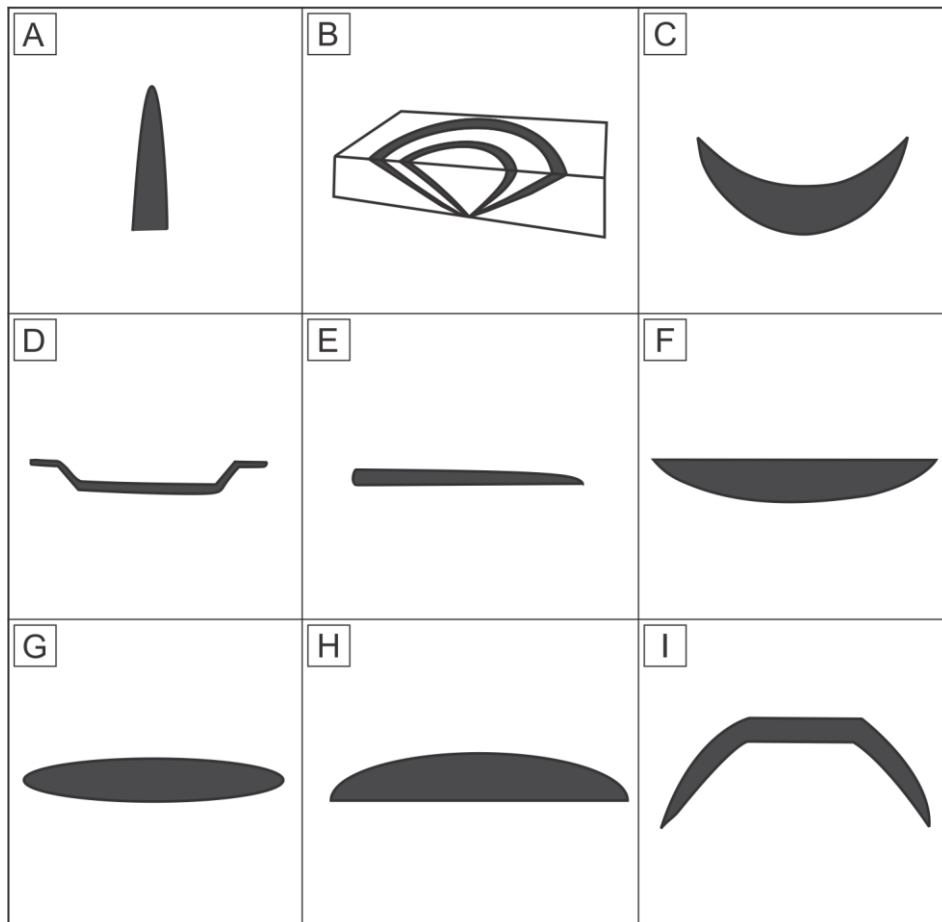
Figure 2.4 – Morphologic description of magmatic intrusions (Modified after Mathieu et al. (2008)): A) dyke; B) cone-sheet; C) cup-shaped intrusion; D) saucer-shaped intrusion; E) sill; F) lopolith; G) pluton; H) laccolith; I) ring.

Planke et al. (2005) in their work on the Vøring and Møre Basins divided sill facies into two main categories (Figure 2.5): the saucer-shaped and the layer parallel, which are distinguished based on the sill reflection, size, smoothness, paleo-surface depth, and continuity on seismic sections. The layer parallel could be sub-divided into five facies: smooth layer parallel (Figure 2.5A.i), basin parallel (Figure 2.5A.ii) layer parallel rough (Figure 2.5A.iii), and planar transgressive (Figure 2.5A.iv), whilst the saucer-shaped can be sub-divided into three facies: shallow intrusion or narrow saucer-shaped (Figure 2.5B.i), saucer-shaped rough (Figure 2.5B.ii), climbing saucer-shaped (Figure 2.5B.iii), and fault block facies (Figure 2.5B.iv). The transition between saucer-shaped and layer parallel can be sub-dived into slightly saucer shaped (Figure 2.5C). Planke et al. (2005) added that the magmatic sills in the Vøring Basin in general, are dominated by shallow intrusions, rough saucer-shaped, layer-parallel, planar transgressive, and layer-parallel rough sills. Omosanya et al. (2016) also documented the formation of eye-shaped sills that formed when a cup-shaped sill at the base merged with a saucer-shaped sill at the overlying layer (Figure 2.5D).
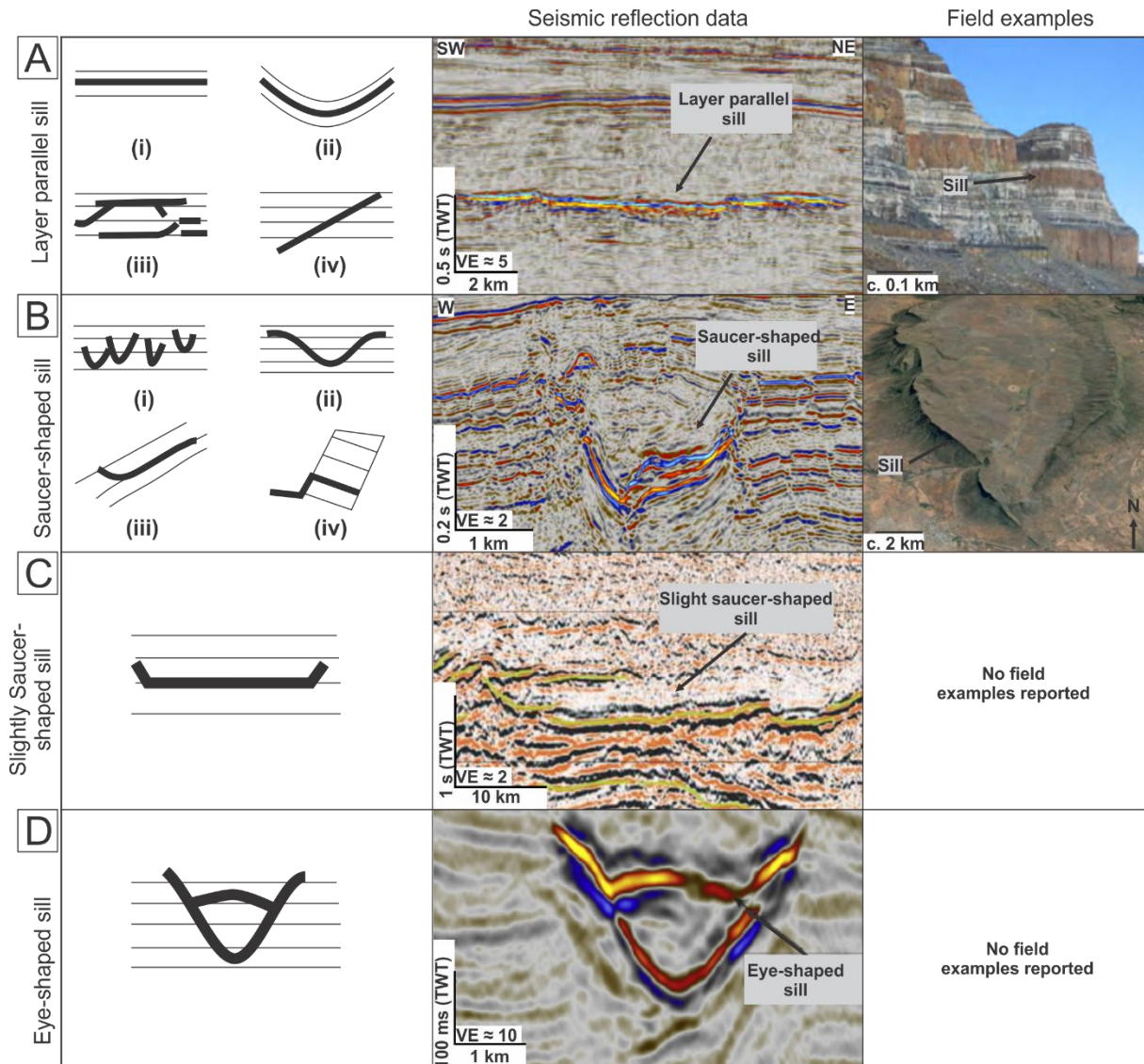
Figure 2.5 – (A) Layer parallel sill facies (Re-drawn based on Planke et al. (2005)). Seismic profile of layer parallel sill geometry in offshore southern Australia (After Jackson et al. (2013)) and the Theron Mountains, Antarctica (After Jackson et al. (2013)). (B) Saucer-shaped sill facies (Re-drawn based on Planke et al. (2005)). Seismic profile of saucer-shaped sill geometry in Exmouth sub-basin, northwest Australia and the Golden Valley Sill in South Africa (after Magee et al. (2015)). (C) Slightly saucer-shaped (Re-drawn based on Planke et al. (2005)). Seismic profile of slightly saucer-shaped geometry in the Møre Basin (Modified after Planke et al. (2005)), no field examples reported. (D) Layer parallel sill facies (Re-drawn based on Planke et al. (2005)). Seismic profile of eye-shaped geometry in the Stappen High, SW Barents Sea (Modified after Omosanya et al. (2016)), no field examples reported.

2.5.1.3 Sill emplacement

The emplacement of the magmatic sills in sedimentary basins remains contentious. Thomson et al. (2008), however, proposed four phases in magmatic sill emplacement: Phase 1- sill initiation; Phase 2- sill lateral growth; Phase 3- sill climbing; and Phase 4- sill flattening (Figure 2.6).

Phase 1- Sill initiation

The melting magma would propagate through the sedimentary layer until it reaches a ductile horizon, under neutral buoyancy. As a result of the contact, the heating would affect the ductile horizon, increase the pore fluid of the country rock, and reduce the effective stress. This process would allow the melting magma to intrude the sedimentary layer until the initial intrusion stage is finished by the overage pore pressure through fracturing at the top of the ductile horizon, or by the solidifying the sill margin that obstructs further intrusion.
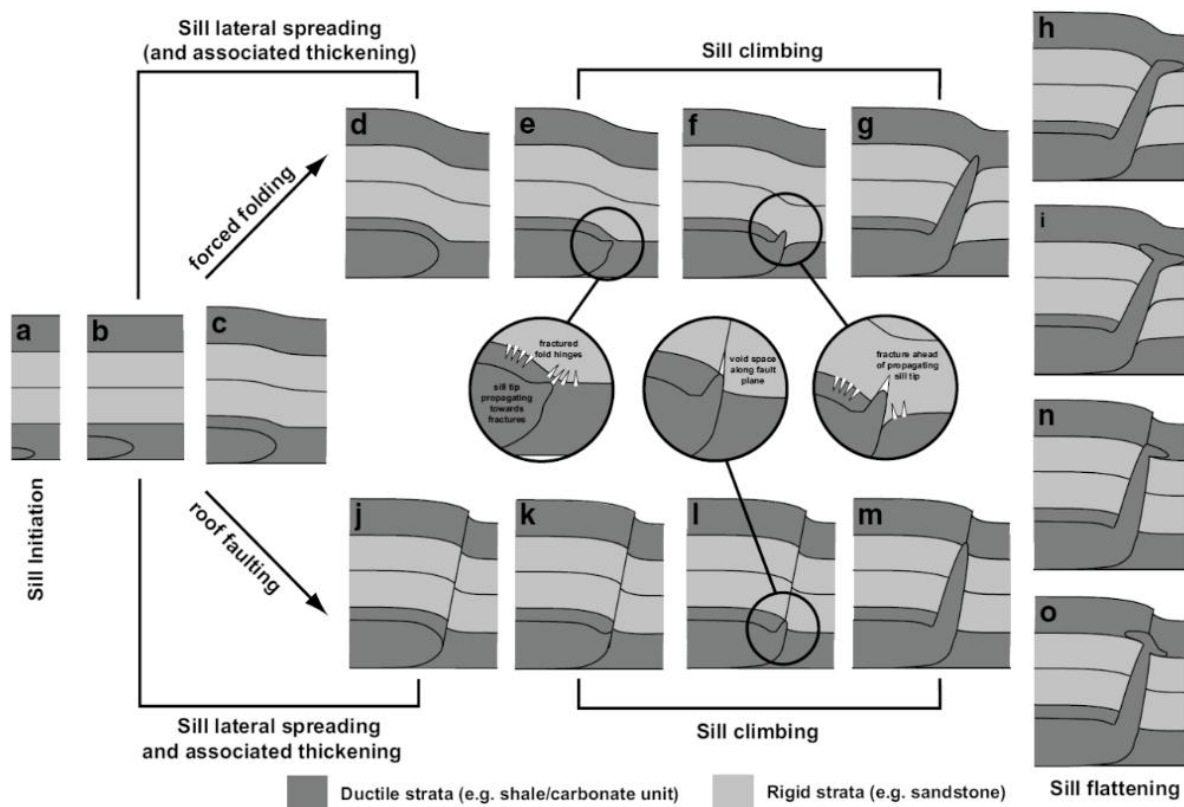
Figure 2.6 – Model of magmatic sill emplacement in sedimentary basins (After Thomson et al. (2008)). The intruded magma encounters a ductile horizon (a). Parallel spreading and thickening of the propagating magma takes place (b-d; b-j). The contact with the formation reduces the effective stress, volatiles the fluid within the horizon, and causes porosity loss. The expansion and thickening of the intrusion thus affect the faulting and/or forced folding of the overlying horizon. These structures create open fractures which are initiated by the sill climbing (e-g; k-m). As the intrusion propagates close to the shallower formations and encounters appropriate horizon, the sill would flatten (h-i; n-o). At this time, the flat outer rim (h and o), symmetrical intrusion (n and o) and a new radially symmetrical saucer may develop.

Phase 2. Sill lateral growth

The inflation at the time when melting magma already moved from the source. The magma inflation is limited, depending on the magma type and the characteristics of the rock. The

characteristics of the country rock include the ability to relieve the pore fluid pressure through fracturing, the elasticity, the fluidization, and the volatilization. Until reaching a suitable depth, these processes would occur peripheral to the sill. This process also may alter the country rock properties at certain depth. During this phase, the magma may be oriented into a steeper direction instead of following the parallel horizon.

Phase 3. Sill climbing

Structural activity at certain depth would lead to fracture of formations that dip against the sill. Affected by the neutral buoyancy, the melting magma would continue to climb and occupy these fractures. This process would create a number of independent, steeply climbing, melting magma bodies that at some point may consolidate to establish a semi-continuous layer.

Phase 4. Sill flattening

This phase is related to the development of the outer rim or new concave-upwards sill in some situations at/below neutral buoyancy. A restricted amount of local climbing develops throughout the sill perimeter, any steep magma would have the ability to create a splitting or branching at the new scale of emplacement in a breakout succession.

2.5.1.4 Sill junction

On seismic reflection data, the sills are typically characterized by very high amplitude and continuous reflections that display parallel and non-parallel relationship with the bedding plane. The geometrical relationship of the sills in the crust has been classified by Cartwright and Hansen (2006) into three main sill junctions as stated below:

Class A junctions

Here, two tips of sills are connected (Figure 2.7a). Three different characteristics are proposed to understand the development of this type of junction. The first model (Figure 2.7b) describes that the connection occurs as the result of sills that propagate towards each other. The second model (Figure 2.7c) is when the sills from the source propagate in bi-directional way. Whilst the third model (Figure 2.7d) occurs at the time that the secondary sill distributes from the adjacent early sill.
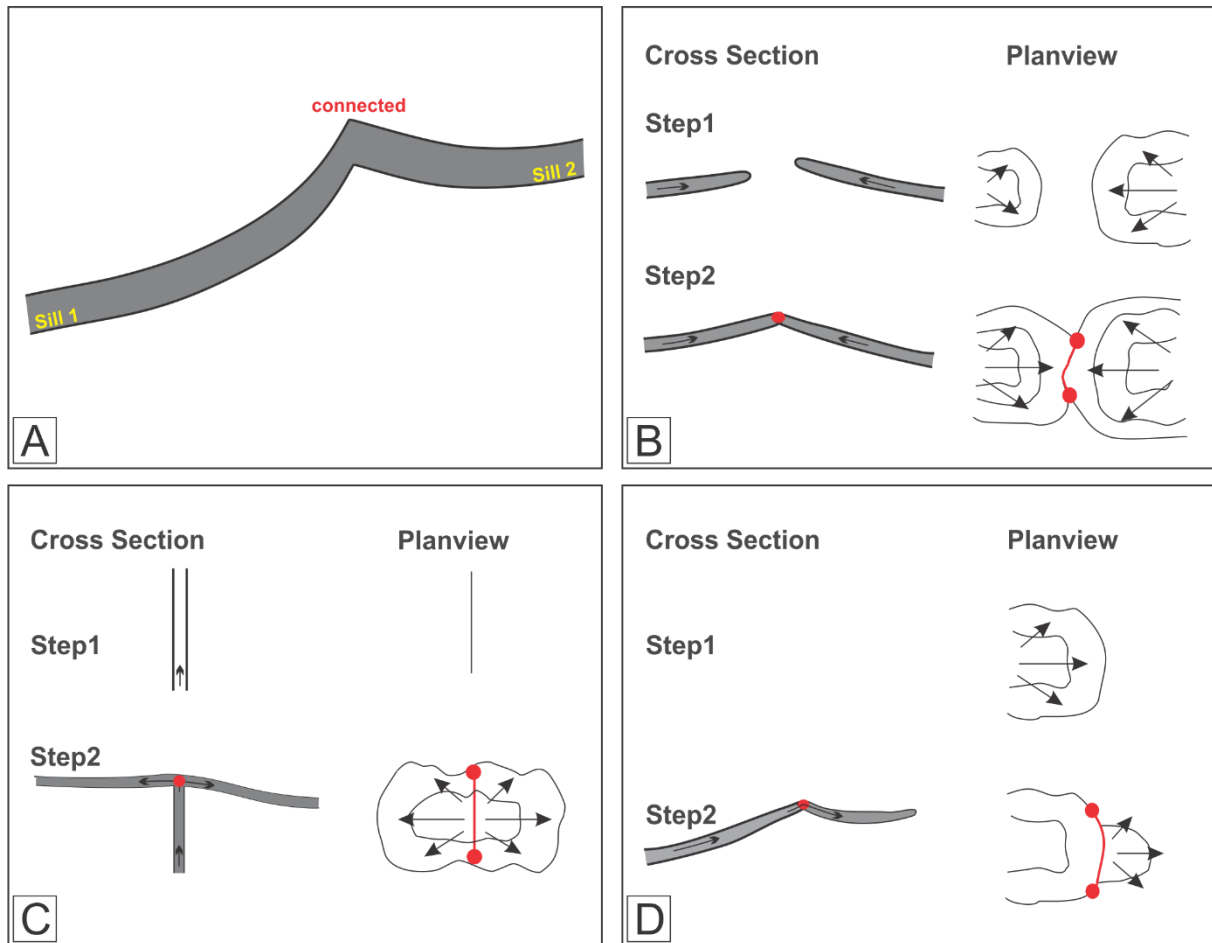
Figure 2.7 – Class A sill junctions cartoon (Modified from Hansen and Cartwright (2006a)).

Class B junctions

This type is the most common geometry and the longest junction in sill complexes. The geometry displays a sill tip, which creates an angle to the other sill body (Figure 2.8a). Three models for the development of class B junctions are known. In the first model (Figure 2.8b), the junction might be formed by the propagation of the subsequent sill which is blocked by the early emplaced sill. In the second model (Figure 2.8c), bi-directional parallel propagation out of a transgressive sill tip occurs because of formation compactness or due to a lithological obstacle. The third model is divided into two (Figure 2.8d): sill branching or splitting, which takes place because of mechanical and lithological heterogeneity. The splitting or branching may also be constrained by local stress that is related to sill propagation.
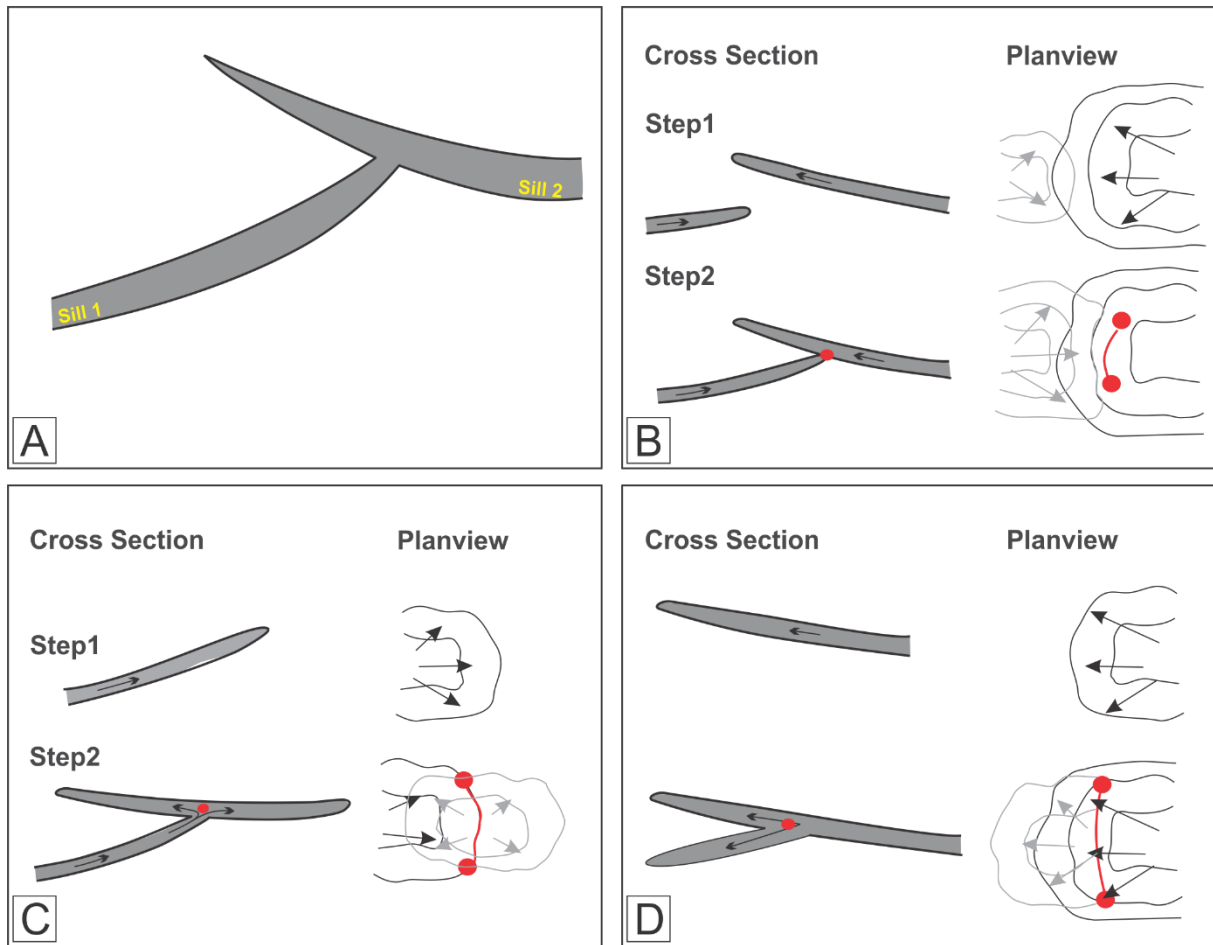
Figure 2.8 – Class B sill junctions cartoon (Modified from Hansen and Cartwright (2006a))

Class C junctions

The subsequent sill (Figure 2.9a) displaces the early emplacement sill. The later sill may drag the early sill to rotate backward (Figure 2.9b).
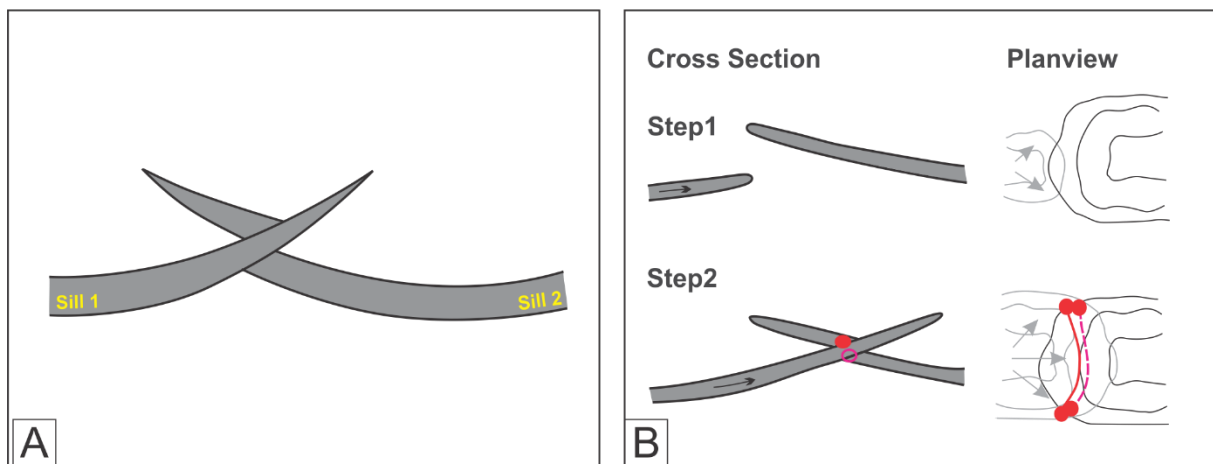
Figure 2.9 – Class C sill junctions cartoon (Modified from Hansen and Cartwright (2006a))

2.5.1.5 Sill structures

Furthermore, Thomson et al. (2008) discussed the typical structural element within magmatic sills in two categories: structures genetically related to brittle process and structures that have their origin related to non-brittle process, as outlined below:

Structures related to brittle process

Structures related to brittle process could be divided into two types: steps and broken bridges. In steps, Thomson et al. (2008) stated that the same process in dyke intrusions could occur also in sill intrusions as well. A series of sills interconnected by a vertical step of an igneous body could result in a step in cross section (Figure 2.10a, 2.10b). Schofield et al. (2012) described the orientation of a stepped sill to be affected by the former fracture orientation or by the development of particular horizon. If the formation of the steps is related to fracture formation in front of the sill tips, the steps would establish en-echelon and step-stair shape (Figure 2.10a), whereas if the steps are related to the development of particular horizon, the steps would display up and down form (Figure 2.10b).
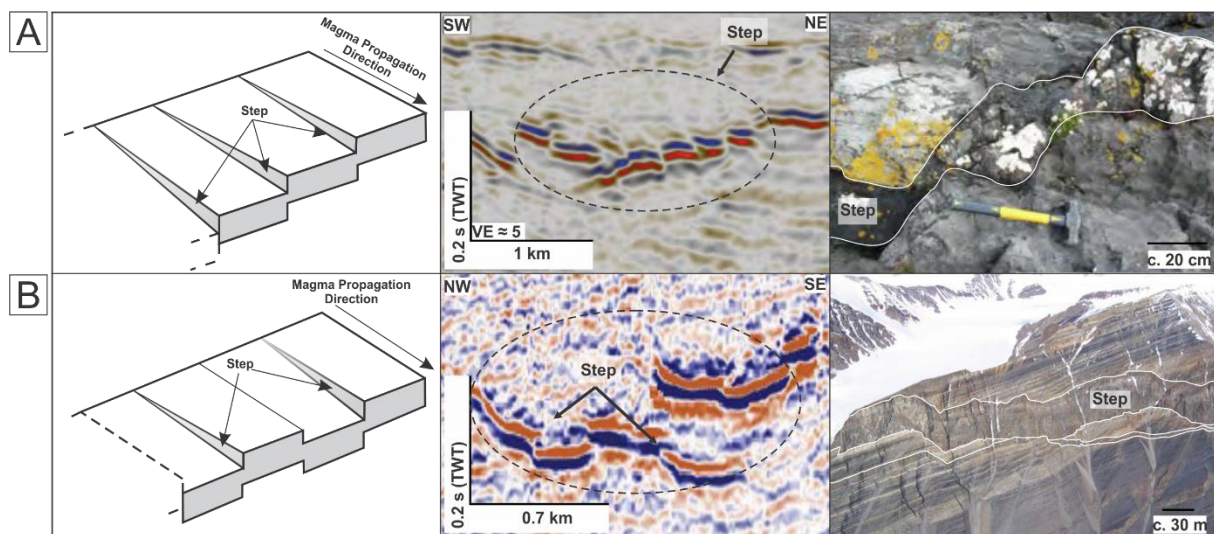
Figure 2.10 – (A) The en-echelon steps process within a sill (After Rickwood (1990); Thomson and Hutton (2004); Schofield et al. (2012)). Seismic reflection and field photo showing intrusive step in the Exmouth Basin (offshore NW Australia) and Ardnamurchan (Northwest Scotland), respectively (After Magee et al. (2016)). (B) An illustration of stepping in different directions showing irregular up and down (Re-drawn from Thomson and Hutton (2004)). Seismic reflection and field photo showing of intrusive steps in the Flett Basin Sill (NW European continental margin) and Axel Heiburg (Canada) (After Magee et al. (2016)).

Schofield et al. (2012) explained that the difference between the step and the broken bridge is the offset segment overlap. The segment overlap caused the later inflation of magma to create

a bridge of strata or a bend, which is extension throughout the convex surface and shortening throughout the concave surface of the bridge (Figure 2.11). In addition, these authors also stated that an open tensile fractures succession is vertical to the bridge axis in the region of maximum flexure. Continuation of magma propagation would become overwhelming for the host rock due to increasing tensile stress within the bridge. These processes would cause the bridge to encounter brittle failure and establish a broken bridge.
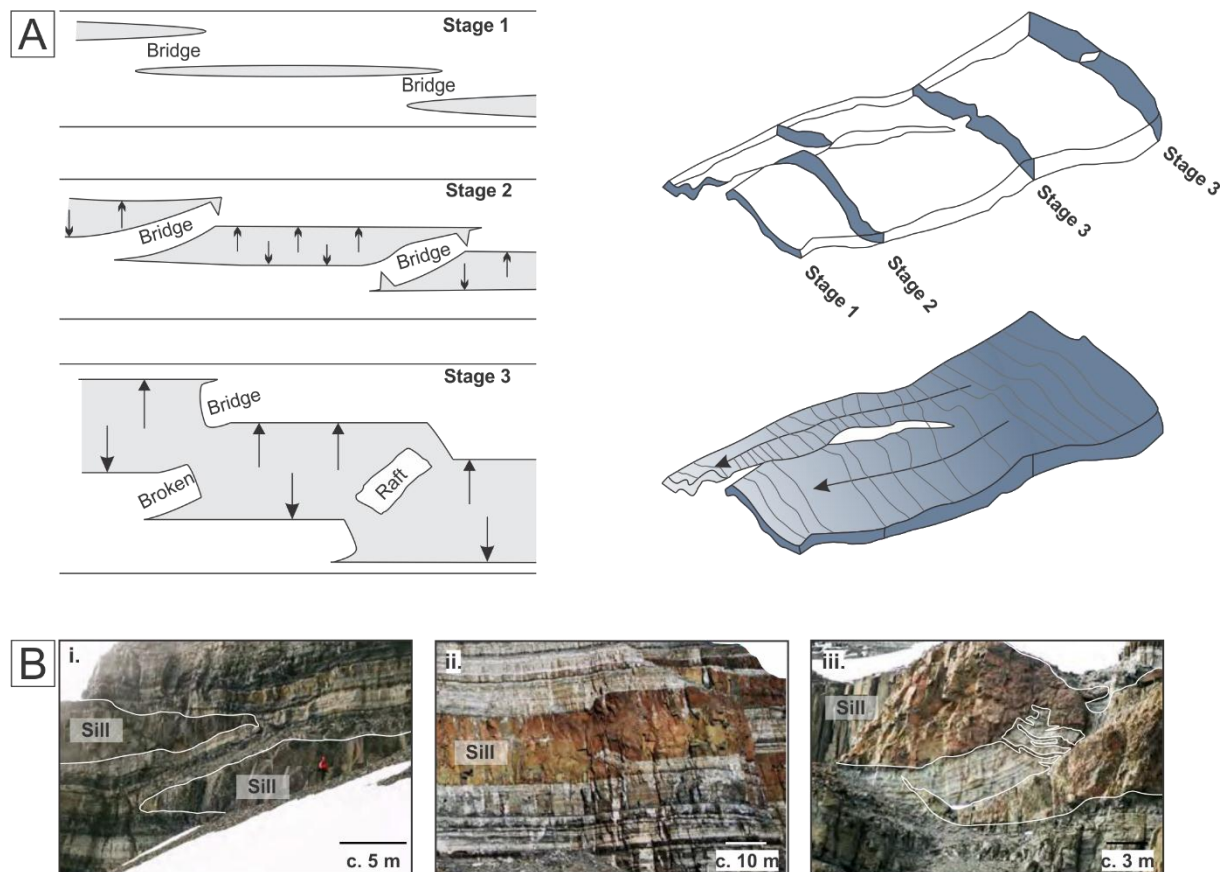
Figure 2.11 – (A) Illustration of broken bridge development within the host rock. Stage 1, melting magma propagates, creating an offset sequence but overlapping bodies. Stage 2, the propagating magma starts to bend each other and deform. Tensile fractures are formed at the area that the flexure of the bridge reaches its maximum. Stage 3, continue inflation of the magmatic bodies in cross-fracture would led to brittle failure, forming a broken bridge (Re-drawn from Schofield et al. (2012)). (B) Field photo of (i) bridge, (ii)broken bridge, and (iii) bridge xenolith in Theron Mountains, Antarctica (After Magee et al. (2016)).

Structures related to non-brittle process

Structures related to brittle process could be divided into: magma fingers and magma lobes (Schofield et al., 2012). Pollard et al. (1975) described that the sill-like surrounding of the laccolith has a finger-shaped, with gently elliptical cross-section, about 1-10 m wide. The finger structures may also be in the form of a lateral expansion against each other and mark a

coalescence. Schofield et al. (2010) noted that the finger formation might also be associated with the formation of saucer-shaped morphology by a way of fluidization within the host rock. Additionally, Schofield et al. (2012) proposed that the magma fingers might be possible if the host rock is poorly consolidated, and subsequently able to transport the grain boundaries through fluidizations activity related to hydrothermal processes (Figure 2.12). Whilst, within the saucer sills, the magma lobe may display a splitting feature away from the inner sill (Thomson and Hutton, 2004; Hansen and Cartwright, 2006b; Schofield et al., 2012).
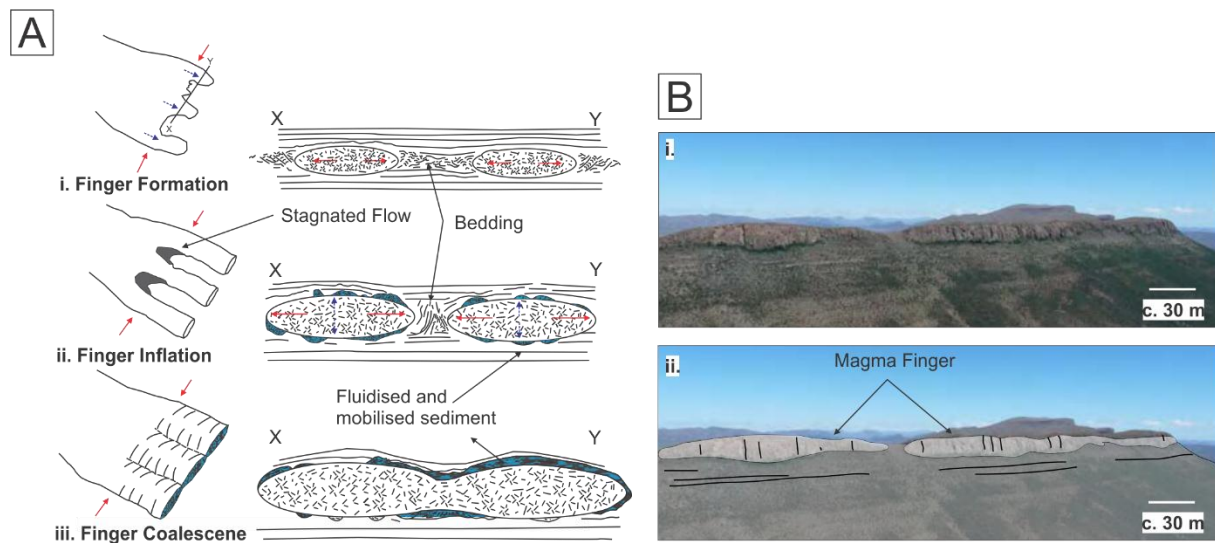
Figure 2.12 – (a) An illustration of magma fingers evolution through time (Re-drawn after Pollard et al. (1975); Schofield et al. (2010); Schofield et al. (2012)). (i) The magma finger geometry was established as the result of inter-relationship between magma and peripheral host rock. (ii) High influx magma would continue to penetrate through the magma finger in vertical and lateral axes. (iii) If, the magma continues to propagate, the magma fingers would merge, establishing an unbroken layer. (b) Uninterpreted (i) interpreted (ii) magma fingers in the Golden Valley Sill, South Africa (After Magee et al. (2016)).

2.5.2 Hydrothermal vents and their development

2.5.2.1 Fluid analysis

Jamtveit et al. (2004) in their study in the Karoo Basin stated that the thermal production shortly after sill emplacement would affect the fluid circulation in the crust to established matrix deformation and fluid channeling. At this early stage, sufficient heat would generate overpressure fluid that is suitable for the formation of hydrothermal venting. The width of the overpressure fluid H_{op} is computed by the length scale for hydraulic diffusion (eq. 2.1):

$$H_{op \approx 2} \sqrt{k_{fluid} . t} \qquad (2.1)$$

Where:

$k_{fluid} = \dfrac{k}{\beta\pi\mu_{fluid}}$ is hydraulic diffusivity.

$\beta \approx 10^{-8}\,Pa^{-1}$ is pore compressibility and effective fluid.

μ_{fluid} is fluid viscosity.

k is permeability.

π is porosity.

t is the time of sill emplacement.

The other measurement to calculate the boiling complex thickness is (eq. 2.2):

$$H_{boil} \approx 2\sqrt{k_T t} \qquad (2.2)$$

Where:

$k_T \approx 10^{-6}\,m^2 s^{-1}$ is heat diffusivity.

The boiling front velocity then could be written as follows (eq. 2.3):

$$V_{boil} \approx \sqrt{k_T t} \qquad (2.3)$$

During an early phase, the fluid is heated by the rock, but is generally insignificant to increase the fluid pressure (Jamtveit et al., 2004). The conductive heat transfers are controlled during these early phases. At the later phases, significant advective heat enables fluid to circulate to create hydrothermal circulation. The volume of fluid at this stage circulating along the same rock start dominates the heat transfer. Contact with cool rocks in the upper part of the boiling zone would condense the hot vapour that affects the boiling front velocity. Jamtveit et al. (2004) observed that the maximum fluid pressure could be achieved during the early pressurization by the calculation of the cold-water properties beyond the boiling zone. The computation could be written as follows (eq. 2.4):

$$Q_d \approx \frac{k}{\mu_{fluid}} \frac{P_{fluid} - P_{hyd}}{H_{OP}} \qquad (2.4)$$

Where:

$P_{fluid}-P_{hyd}$ is the discrepancy between hydrostatic pressure and fluid pressure (the overpressure).

Jamtveit et al. (2004) stated that the production of steam is massive initially, due to small overpressure $Q_D << V_{boil}$. Slowly the fluid pressure would increase and be characterized by a quasi-static-flux balance, as could be expressed (eq. 2.5):

$$\rho Q_D = \pi \Delta \rho_{boil} V_{boil} \tag{2.5}$$

Where:

ρ and $\Delta \rho_{boil} \approx \rho$ are the density of the cold water and density discrepancy between supercritical vapour and cold water.

By solving the non-hydrostatic fluid pressure build-up, the computation becomes (eq.2.6):

$$\rho_{fluid}^{max} \approx P_{hyd} \left[1 + 2 \frac{\Delta \rho_{boil}}{\rho \beta P_{hyd} \sqrt{k_T k_{fluid}}} \right] \tag{2.6}$$

To quantify the pressure build-up due to venting, Jamtveit et al. (2004) assign the dimensionless parameter V_e that can be written as follows (eq.7):

$$V_e = \frac{P_{fluid}^{max} - P_{hyd}}{P_{hyd}} \approx 2 \frac{\Delta \rho_{boil}}{\rho \beta P_{hyd} \sqrt{k_T k_{fluid}}} \tag{2.7}$$

By assuming $\Delta \rho_{boil} \approx \dfrac{\rho}{2}$ and substituting into (eq.7), the V_e could be expressed (eq. 2.8):

$$V_e = \frac{1}{\beta P_{hyd}} \sqrt{\frac{k_T}{k_{fluid}}} \approx \frac{1}{10^7 Z \sqrt{\dfrac{\mu_{fluid} k_T}{k_\beta}}}$$

$$\approx 10^{-7} Z \sqrt{k} \tag{2.8}$$

Where:

Z is the depth of the magmatic intrusion (kilometer).

Based on these computations, Jamtveit et al. (2004) observed that if the $V_e << 1$, the magmatic sill is emplaced in a permeable condition that avoid fluid pressure build-up due to pressure production being lower compared to pressure diffusion. Whilst $V_e >> 1$ is corresponds to the fluid-pressure increase and a 'explode' condition takes place when the fluid pressure exceeds the lithostatic pressure. During this phase, the fluid pressure would produce its own permeability by disfiguring the upper strata and creating a fluid release structure.

2.5.2.2 Geometry of hydrothermal vents

Physically, the anatomy of hydrothermal vent complexes includes pipe-shaped, downward-tampering conical shapes or diatreme-like structures on seismic sections (Figure 2.13). These structures are established because of the host rock fracturing, commonly associated with the tip or crest of underlying magmatic sills (Jamtveit et al., 2004; Planke et al., 2005; Hansen and Cartwright, 2006a).
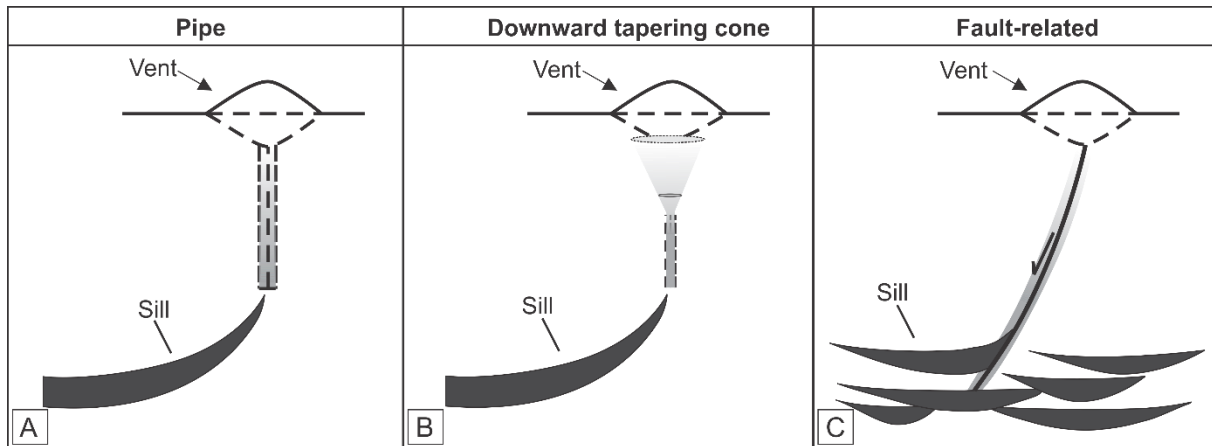
Figure 2.13 – Illustration of hydrothermal vent structures (Re-drawn from Hansen and Cartwright (2006a)): (A) pipe-like; (B) downward-tapering cone; (C) fault related.

In plan view, the vents are characterized by circular to elliptical structures near the tops (Planke et al., 2005; Hansen and Cartwright, 2006a). Three geometrical styles of hydrothermal vents upper parts have been proposed by Planke et al. (2005), based on three-dimensional seismic survey from the Vøring and Møre Basins: eye-shaped, dome-shaped, and crater-shaped (Figure 2.14). Vents with eye-shaped are limited by the doming of the overlying strata, or may onlapped or be concordant with the underlying formation strata (Planke et al., 2005; Hansen and Cartwright, 2006a). The internal reflectors within these types of vents may display chaotic features (Alvarenga et al., 2016). Dome-shaped vents generally having a flat-lying base, concordant with the underlying strata, and forming onlapped doming within the overburden (Planke et al., 2005; Hansen and Cartwright, 2006a). Crater vents are characterized by a truncational base and are concordant with adjacent reflectors (Hansen and Cartwright, 2006a; Alvarenga et al., 2016). Furthermore, Hansen and Cartwright (2006a) added more terminologies to characterize vent structures on seismic sections based on their basal and overburden relationships, and internal geometry (Figure 2.14).
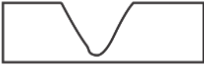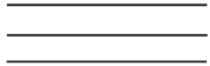
Planke et al. (2005)	Hansen (2006)		
	Basal relationship	Overburden relationship	Internal geometry
Eye-shaped	Truncational	Concordant	Onion-ring structure
Dome-shaped	Downwarped concordant	Dome-shaped	Downlapping
Crater-shaped	Flat-flying concordant	Onlapping	Chaotic

Figure 2.14 – Vent structures cartoon (Planke et al., 2005; Hansen and Cartwright, 2006a; Alvarenga et al., 2016).

2.5.2.3 Composition

The composition of vents remains a subject of debate (Davies et al., 2002; Planke et al., 2005; Hansen and Cartwright, 2006a). Previous study by Planke et al. (2005) has interpreted the composition of the upper mound as a seep carbonate formation, whereas Davies et al. (2002) interpreted the vent fill as being of magmatic origin. These types of composition could not become representative of vents around the world. Studies by Hansen and Cartwright (2006a) considered that the composition could be vent filled sedimentary rocks, based on interpretation from the central Faroe-Shetland Basin. In addition, Jamtveit et al. (2004) also support this argument that the hydrothermal vents are probably filled by sedimentary or magmatic materials (Jamtveit et al., 2004; Hansen and Cartwright, 2006a).

2.5.2.4 Relationship with underlying sills

Detailed three-dimensional seismic interpretation of vent structures by Hansen and Cartwright (2006a) in the NE Atlantic margin have shown that most of the hydrothermal vents are generally associated with underlying sills, which co-exist with fault complexes. On seismic sections, the hydrothermal vents and the down-ward structures are expressed by low amplitude to chaotic reflections, while the magmatic sills generally have very high amplitude reflections (Figure 2.15).
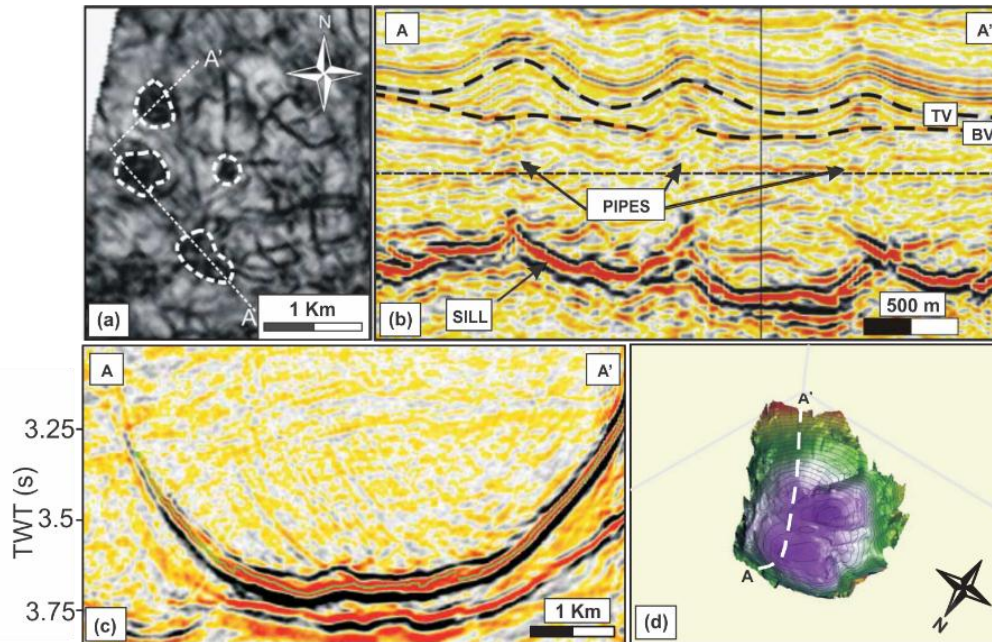
Figure 2.15 – Seismic profile from the northern Faroe Shetland Basin (Hansen et al., 2004; Hansen and Cartwright, 2006a) displaying a direct connection between vents and underlying sills: (a) variance attribute shows the radial or circular morphology; (b) the structural complex pipe-shapes with underlying saucer-shaped sills; (c) individual saucer-shaped sill; (d) the saucer-shaped in a 3D seismic window.

2.5.3 Crestal and radial faults

Crestal and radial faults have attracted considerable attention in the literature, emphasizing their geometry and nature in sedimentary basins. Their classification into fault families was done by Rowan et al. (1999) based on their study in the northern Gulf of Mexico (Figure 2.16) into salt-related symmetrical and asymmetrical arrays. In the case of salt basins, extensional faults in symmetric arrays include crestal faults that generally show faults rooted in reactive diapirs and fault complexes at the upper part of salt anticlines (Rowan et al., 1999). Contrastingly, the asymmetrical arrays of normal faults are characterized based on their dip orientation. Included in this group are roller faults that dip originally basin-ward; ramp faults that increase upward from the onshore margin; and shale-detachment faults that are isolated into a shale decollement (Rowan et al., 1999). Furthermore, Rowan et al. (1999) also stated that the asymmetrical arrays with dip direction element includes flap faults that have footwalls with rotated and uplifted roof strata; and rollover faults at the hinges of monoclinal folds.
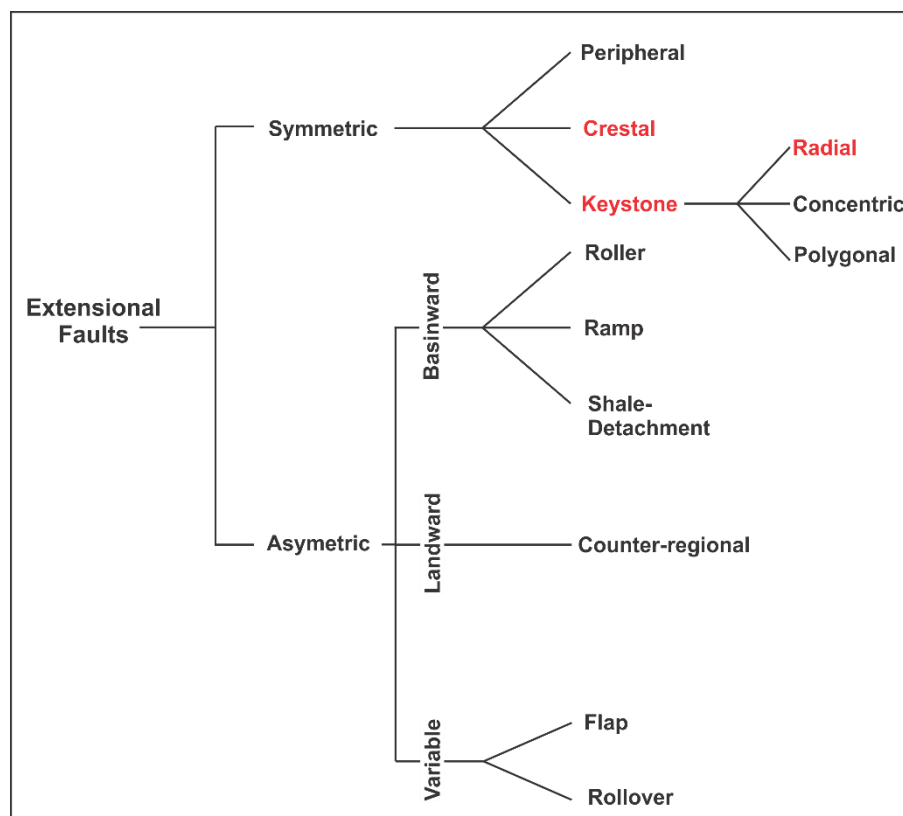
Figure 2.16 – Description of fault families in extensional settings (Rowan et al., 1999).

The focus of this study includes the symmetrical arrays: crestal and keystone (radial) faults. Sedimentary layers intruded by magma could create an accommodation space in form of bending up, and are separated from the central axis in a circular synform (Stewart, 2006).

Rowan et al. (1999) observed that crestal faults are characterized by the development of planar faults that are forming symmetric grabens and rooted into the crests. Down to the flanks of salt diapirs, the age of syn-kinematic strata and the faults increases, whereas the offset in the upper part of the salt where the faults penetrating tends to be small. The geometry of crestal faults in salt diapirs based on map view is restricted, straight to curved grabens, and characterized by polygonal features (Travis et al., 1995; Rowan et al., 1999). Rowan et al. (1999) also documented that crestal faults are basin-ward–related, where the fault azimuth typically equals to the shelf margin and shoreline. Geometrically, drape faults are identical to crestal faults unless the drapes are established in asymmetric arrays (Rowan et al., 1999).
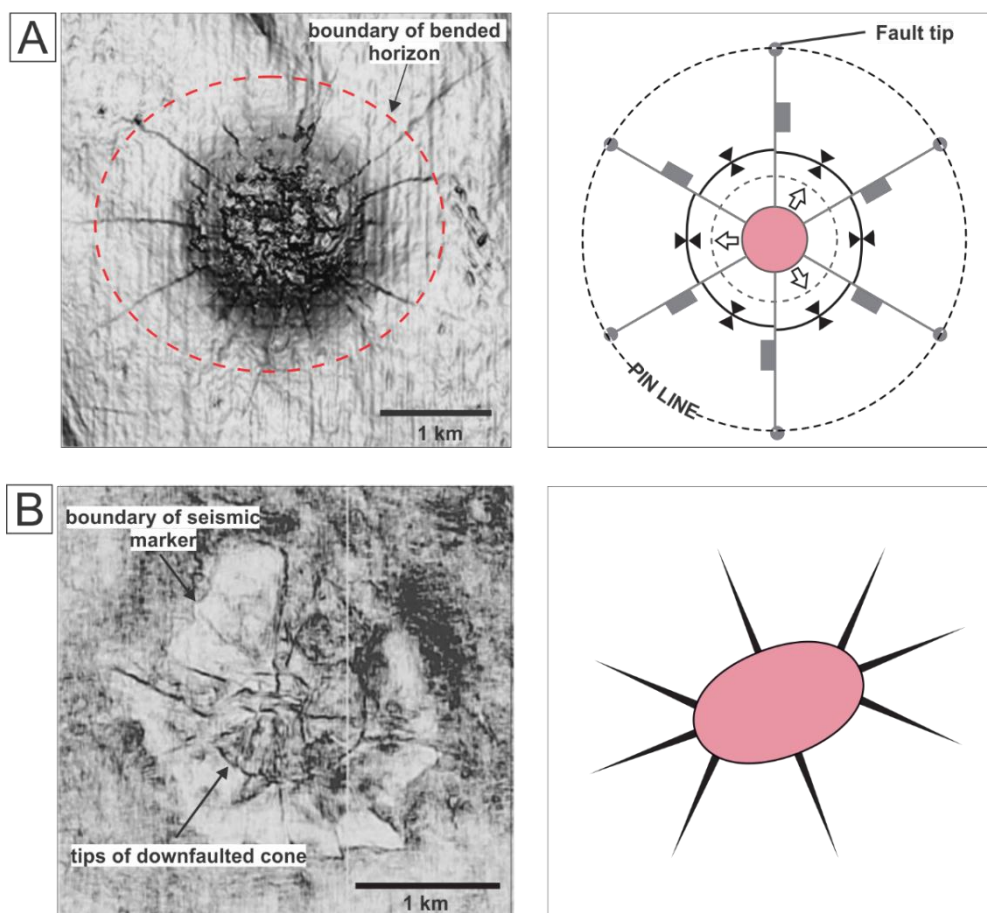
Figure 2.17 – Radial and crestal faults are mapped in 3D seismic data (Stewart, 2006). (A) Domed sediments creating radial faults overlying salt diapirs, North Sea. The cartoon (right) shows the expansion of central zone forced folds with circular orientation, accommodated by radial fault patterns. (B) The radial and crestal faults with cone-shapes in the North Sea. The cartoon to the right shows the radial faults line connected to the end of elliptical intrusion.

Consequently, keystone faults are developed in the hinge zone of anticlines triggered by bending or buckling and do not ordinarily contain any regional contraction (Rowan et al., 1999).

These faults are planar, straight to curvilinear in map view and are similar to crestal faults (Rowan et al., 1999). On salt diapirs, the keystone faults are established in the layers overlying the crest of folds, do not root into the salt, and typically are undeveloped faults that have displacement that decline either upward or downward (Rowan et al., 1999). Included in keystones faults are radial faults that show intersection with other fault families (flap, crestal, roller, rollover, counter-regional, or lateral faults). Stewart (2006) observed that the pattern of radial faults may preferentially be related to polygonal faults (Figure 2.17). At the same level, the polygonal and radial faults may have identical spacing and maximum throws, but showing a range of aspect ratio and length (Carruthers, 2012). Carruthers (2012) documented that, during salt diapirism or intrusion, radial faults are expanded or widened as they propagate, and contracted as they became narrower or slowed.

Chapter 3

Materials and Methods

3.1 Data

The NPD-NTNU-Schlumberger Petrel Ready Database provides the database for this study, which comprises of high-quality, two-dimensional (2-D) and three-dimensional (3-D) seismic data and wireline logs from a wellbore. The wellbore (6706/6-1) is situated in the middle of three-dimensional seismic data. All the dataset will be used to interpret the geology of the study area using the industry based software Petrel®. The three-dimensional seismic data covers an area of about 1200 km^2 on the northern Vøring Basin with a maximum water depth of roughly 1298 m. The bin spacing in inline (north-south) and crossline (east-west) direction are 25 m and 12.5 m, respectively. The seismic data are in time domain and with a dominant frequency of 40 Hz. Using a velocity of 5.55 km/s for the magmatic sill (Skogly, 1998; Hansen and Cartwright, 2006a) the $\lambda/4$, which is the limit of vertical resolution, is 34 m (Sheriff and Geldart, 1995).
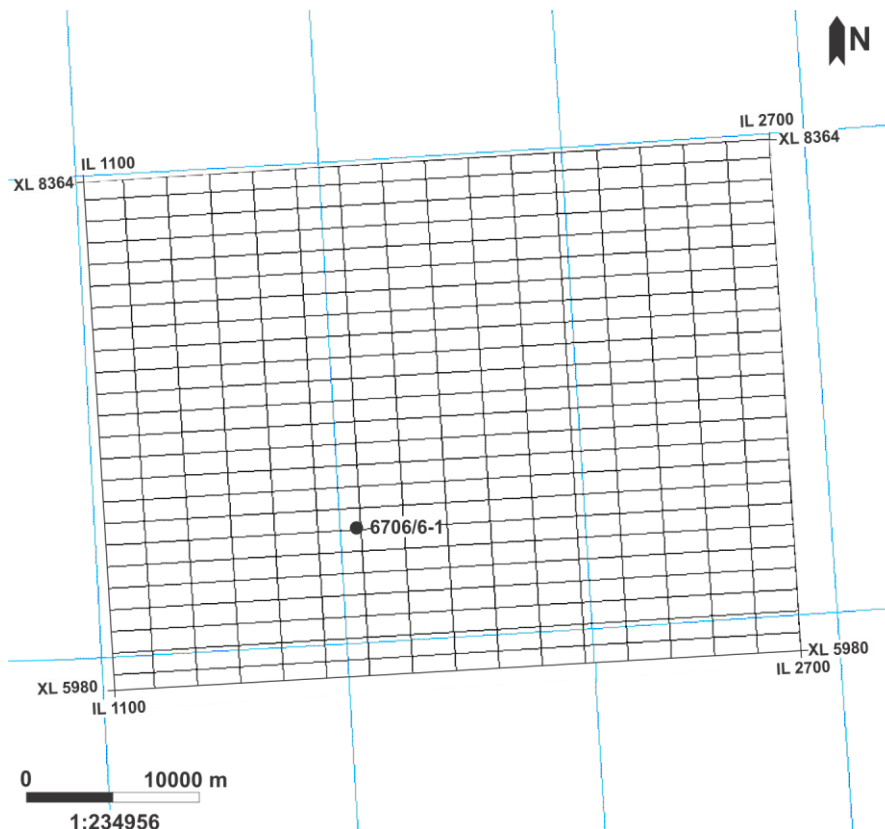
Figure 3.1 – The outline of the 3-D seismic data showing the location of wellbore 6706/6-1 in the study area.

Consequently, the seismic data are zero-phased and are displayed in normal SEG polarity, i.e., an increase in acoustic impedance with depth is a peak or black reflection, while decreasing acoustic impedance with depth are displayed as troughs or red reflections. As the seismic data are in the time domain, a time-depth relationship is done to obtain the true depth of horizons and faults. An average p-wave velocity of 2000 m/s TWT from wellbore 6706/6-1 within the Naust and Tang Formations is used for depth conversion.
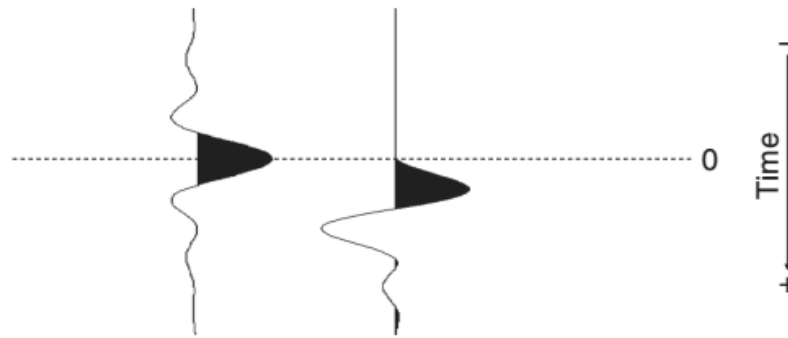
Figure 3.2 – The zero-phase wavelet (left) correspond correctly to the reflection interface, whereas the trace in minimum phase (right) showing mismatch with the reflection interface (Herron, 2011).

3.2 Well data

Well 6706/6-1 situated at the Naglfar Dome in the northern Vøring Basin is a wildcat drilled by Esso Exploration and Production Norway A/S in 2013. The well was drilled as a frontier well to test the hydrocarbon potential of the Cretaceous Hvitveis prospect (NPD, 2017). The presence of weak oil was observed on core samples obtained at 3283.55 m. There is dry gas accumulation in the reservoir sandstone that is interbedded with shale at 3239 m until free water level at 3266 m. The well has a total depth of 3451 m (RKB), and penetrates from the Nordland Group (Naust Formation) until the Pre-Cenozoic unit. The well was abandoned after the gas discovery.

Table 3-1 – The summary of well 6706/6-1.

Well name	TD (m)	Oldest Formation	Age	Content
6706/6-1	3451	No Formal	Palaeocene	Gas

3.3 Horizon interpretation

Before horizon interpretation was done, the seismic to well tie was done in order to tie the seismic units in time to their equivalent formation tops in depth in the wellbore (Figure 3.3).

The seismic to well tie is done by correlating the well top using petrophysical properties, for instance density, sonic log, neutron, gamma-ray, etc., and it comprises of three main steps i.e., (a) sonic calibration (b) synthetic generation and (c) correction.
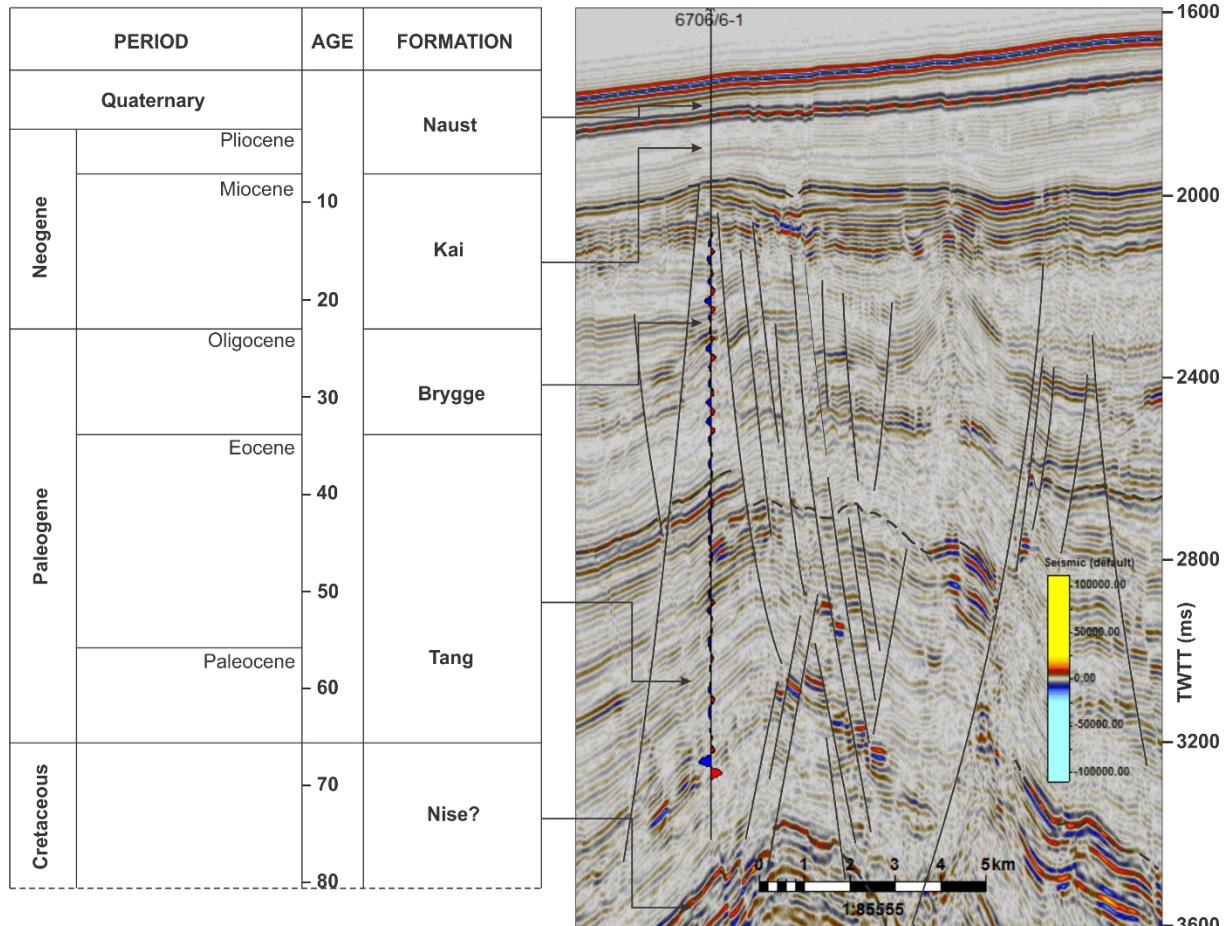
Figure 3.3 − Seismic section shown the synthetic seismogram overlain on the seismic data.

The sonic generation is done using sonic logs and seismic time from checkshot data. For the checkshot data, the calibration need to be done by removing the anomalies or spikes in the data. This process is called despiking. The aim of this calibration is to generate better resolution of the well data with the seismic data. By input, the Time-Depth Relationship (TDR) calibration, time relationship (Tl-Tc=0), and marine datum, the sonic generation is constructed. The next stage is to correlate the wave phase in the wellbore to be displayed in seismic data by generating synthetic seismograms. The synthetic generation was done by converting time with checkshot data by creating TDR, calculating the acoustic impedance (AI), calculating reflection coefficient (RC) using density, sonic log, and extracting wavelet (Figure 3.3). The result of synthetic data, in many circumstances need to be calibrated in order to be compatible with the seismic image.

For horizon interpretation, the interpretation of fault was undertaken first to obtain a general structural overview of the study area. After fault interpretation, key horizons of interest were interpreted using the three-dimensional automatic tracking tool in Petrel® at grid spacing of 10 (250 m) – 25 (625 m) inlines, whereas automatic interpretation on the cross-lines was dependent upon the continuity of the interpreted horizon. Where the horizon is continuous, the 3D automatic tool was used for interpretation. Otherwise 2D tracking tool or manual interpretation at crossline spacing of 10 (125 m) – 25 (312.5 m) was done. Five (5) horizons were interpreted from the seabed to the TD within the well. The seismic characters of the horizons are summarized in Table 3-2. After all the horizons were interpreted, the next stage was to create surface and isochore maps. These maps were used as inputs for horizon and zone modelling.

Table 3-2 – Description of the interpreted seismic horizons.

Unit	Ref. Coefficient	Peak/Trough	Uncertainties
H1	Positive	Peak	Simple reflector and easy to pick.
H2	Negative	Trough	High to moderate amplitude, thinning.
H3	Positive	Peak	Moderate to low amplitude, thinning, affected by numerous faults and hydrothermal vents.
H4	Negative	Trough	Moderate to low amplitude, high uncertainty, affected by numerous faults and hydrothermal vents.
H5	Positive	Peak	High uncertainty, undistributed well, affected by numerous faults.

3.4 Fault interpretation

Fault analysis in three-dimensional seismic data was done by tracking or mapping of fault planes on grid spacing of 25 (625 m) inlines. In addition to interpreting the faults on seismic sections, fault orientations and distributions were identified additionally using seismic attributes. Once the faults were interpreted, a fault model is created using structural framework tools in Petrel®. To move the interpreted into a fault model, the faults must first be converted into fault model with grid spacing of 50 inlines (Figure 3.4). The fault type must be selected (linear, vertical, listric or curved). After which the advance structural processing can be done by displaying the faults in two-dimensional window. The next step is to choose pillar gridding for the top, mid, and base unit of the formation of interest. For this study, the top unit is the

Naust Formation and the base is the Tang Formation. The results of this process are surface skeletons that would represent the grid surface to be modelled.
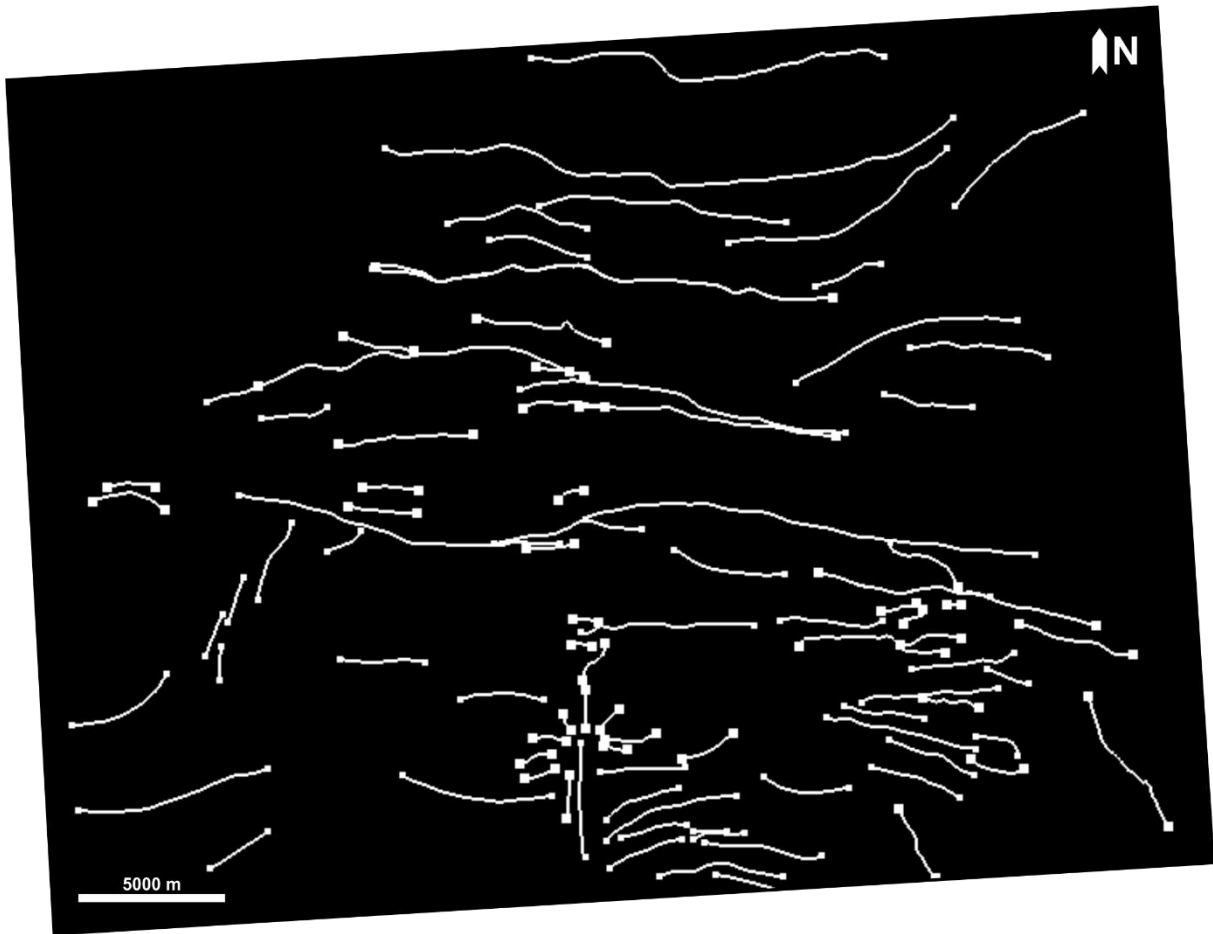
Figure 3.4 – The faults points in two-dimensional window showing the fault distributions.

After the fault model has been built, the next phase is to create the fault frameworks. By using the fault framework, the properties of the faults could be determined automatically by the software e.g., fault throw, fault displacement, fault dip, and fault dip direction. The value of fault dip and fault dip direction properties then will be used in construction the circular histogram plot that showing the directional and frequency of each dip value, known as rose diagram. The rose diagram is a common tool in structural geology, especially in identifying the direction/orientation/trend of faults, fractures, joints, or dykes. At first, the entire values of the fault dip and fault dip direction are converted into points which was displayed in the input tab, then all the points were exported into ASCII format. Go to well tab to create a new well data. In well data setting, only the specific bottom MD need to be set-up. Typically, the set-up value is using the deepest than 'Z' value of dip points. Afterwards, the ASCII format was imported

onto the new well data. Using the polar frequency plot track from the new well section window, the dip values of the new well data will be exported into rose diagram, displaying the dip and dip direction.

3.5 Sill Interpretation

Magmatic sills were identified and mapped manually on the three-dimensional seismic data based on their intersections with the host-rock strata and high amplitude character. Additionally, seismic attributes such as Root Mean Square (RMS) Amplitude were used in the interpretation of the magmatic sills (see section 3.7). These attributes allowed further identification of the sills due to the high acoustic impedance contrast between the sill and host rock strata (Smallwood and Maresh, 2002; Mattos et al., 2016; Omosanya et al., 2016; Omosanya et al., 2017). Furthermore, the continuity, geometry, and size of the magmatic sills were described using morphometric character such as area, length and their depth of occurrence. Depth of occurrence allowed the division of the sills into three categories: shallow sills at depth of less than 3.5 ms TWTT, intermediate sills at depth of 3.5-5 ms TWTT, and deeper sills at depth of more than 5 ms TWTT.

3.6 Hydrothermal vent interpretation

On seismic sections, the presence of hydrothermal vent complexes is recognized based on their upper part morphology (e.g., dome-, eye-, crater-shaped), their downward structure (e.g., down-tampering cone), and their correlation with peripheral structures (e.g., radial faults). In plan view, to identify the bend-up structures of vent, seismic attributes provide better resolution rather than the normal phase seismic section (e.g., spectral decomposition, chaos). The spectral decomposition generally untangles the seismic amplitude into specific frequency allowing to construct subtle geology features (e.g., concave or convex morphology), while the chaos attributes generally are able to identify the bend-up structure or fluid feature. The chaos generally enhanced the chaotic texture adjacent/within the fault plane and discriminates the low amplitudes in seismic profile. The enhancement of chaotic texture could be used for extracting the 3-D geometry of fluid feature using probe geobody. All in all, using these attributes, the vents are recognized (see section 3.7). Furthermore, statistical analysis of the radius of interference 'r' is used to identify the correlation between the 'r' of the hydrothermal vent and depth. Using this correlation, the distribution of down-structure of the vent generally could be identified (Figure 2.14).
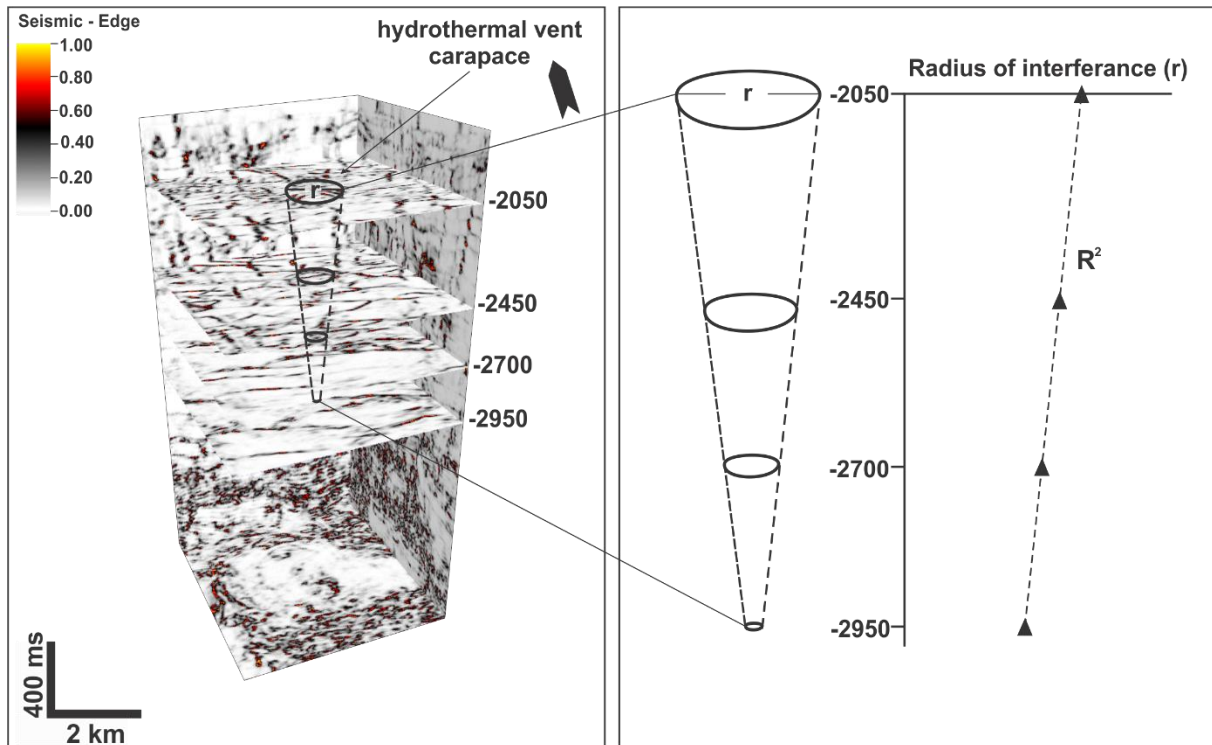
Figure 3.5 – Chaos attribute is used to determine the radius of interference 'r' for the hydrothermal vent complexes. The analysis would be used to identify the relationship between 'r' of the hydrothermal vent and depth.

3.7 Seismic attribute analysis

Seismic attribute maps are common tools that have been used for detailed and accurate mapping of horizons, faults, magmatic intrusions, and fluid-flow features on seismic sections. Signal distortions and limitations in seismic reflection, therefore, require additional attributes to increase confidence in analysis. Active use of attributes specifically is addressed in the analysis of structures and magmatic features (e.g., hydrothermal vents and sills) in the study area. The seismic attributes that have proven useful for structural and hydrothermal vent analysis are chaos attribute (e.g., Omosanya et al., 2017) and spectral decomposition (e.g., Kjoberg et al., 2017). Whilst for magmatic sill analysis, the Root Mean Square (RMS) attribute has shown to be an effective method (e.g., Alvarenga et al., 2016).

3.7.1 Chaos attribute

Throughout computer-based modelling, the chaos attribute generally has the similarity with variance attribute. The chaos attribute use the local attribute to measure the signal unconformity from horizontal sub-slices in three-dimensional seismic reflection data that represent trace-to-trace variability (Randen et al., 2001). This attribute enhances the chaotic texture to discriminate

the signal pattern in seismic profile (Figure 3.6). In general, it can be used for fault detection, bending-up morphology, fluid migration, reef texture, channel infill, reed texture, and intrusions (Randen et al., 2001). For fault detection, the parameter of chaos attribute could be adjusted by estimating the vertical nature of faults or by using the fault dipping (Randen et al., 2001).
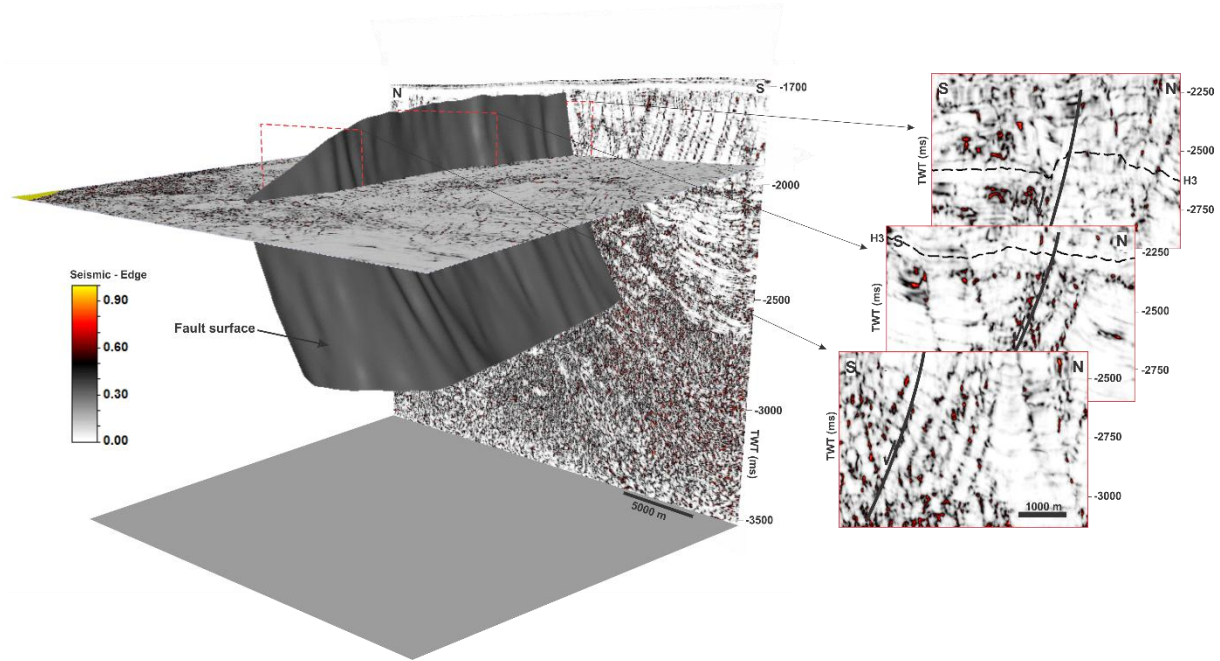
Figure 3.6 – The appearance of chaos attribute in plan view and in intersection window.

3.7.2 Root Mean Square (RMS) attribute

RMS is a common attribute in seismic reflectivity due to its ability in direct hydrocarbon identification. This attribute computes the sum of the squares of amplitude divided by the total of samples in a zone of interest (Chudi, 2015). Typically, the RMS amplitude corresponds to the variation in acoustic impedance. The formula that is used in computation of Root Mean Square (RMS) attribute can be written as follow (eq. 4.1):

$$RMS = \frac{\sqrt{\sum_i^n amp_t^2 * w_t}}{\sum_i^n w_t}$$

$$(4.1)$$

Where:

n is number of samples

amp is amplitude.

w_t is the weight of every amplitude value.

The higher the acoustic impedance (AI) value, the higher the result of RMS value (Chudi, 2015). Magmatic sills are an example of geologic features that have high acoustic impedance relative to low amplitude host-rock strata (Figure 3.7). This seismic expression distinguishes the stratigraphic layers that, in some cases, have high amplitude reflection similar with the magmatic sills (e.g., sandstones).
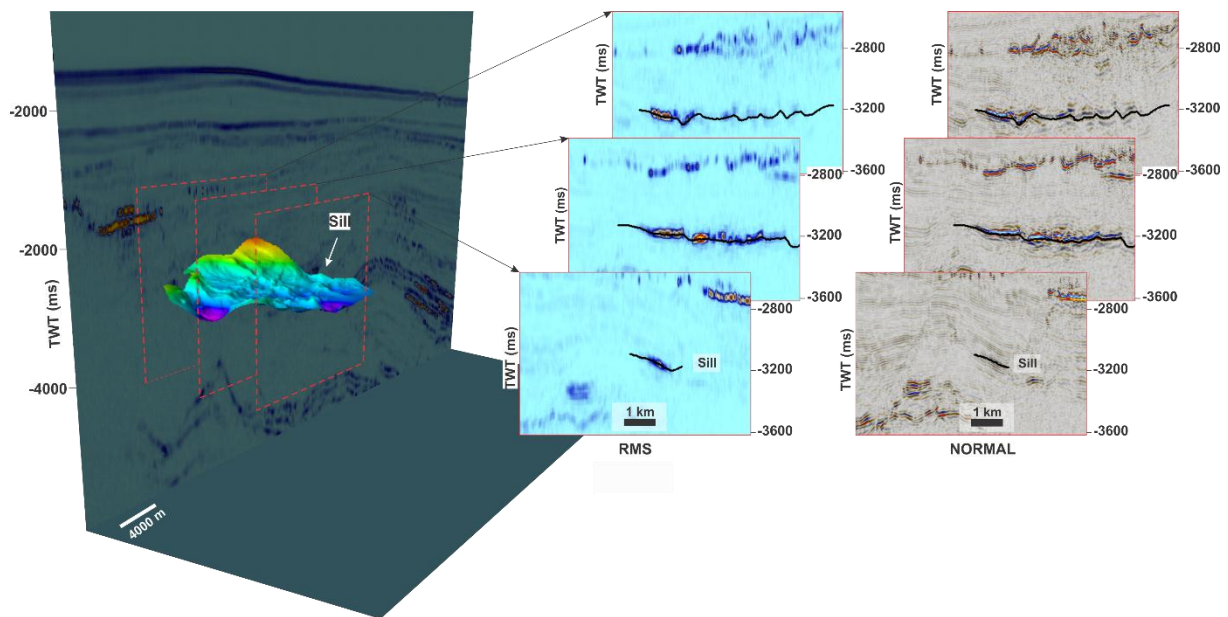
Figure 3.7 – The comparison of RMS amplitude with normal phase seismic section in seismic profile, showing an indication of magmatic sill.

3.7.3 Spectral Decomposition

Spectral decomposition is used by transforming the seismic data into local frequency using the Discrete Fourier Transform (DFT) (Gridley and Partyka, 1997). Spectral decomposition generally use specific frequencies from seismic profile (Figure 3.8b) allowing to distinguish such geological features e.g., channels, hydrothermal vent. This attribute is divided into two resolutions: the vertical and frequency resolutions. Both resolutions could not be used at the same time. For this study, the vertical resolutions are important to increase rather than the frequency resolution. The default frequency in this study generally ranges from (11-14 Hz), the number of cycles less than 3.0, and use sample by sample resolution (e.g., Figure 3.8a). The sample by sample resolution generally has better result in time/depth slices, which is important to identify the continuity of hydrothermal vent morphology through depth.
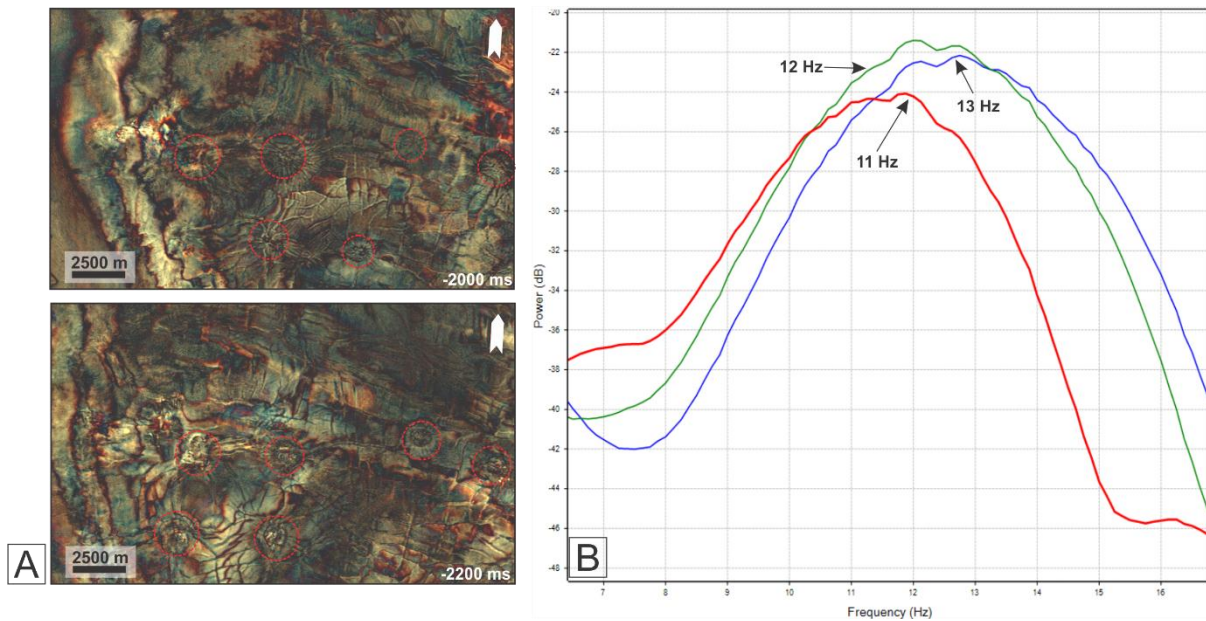
Figure 3.8 – (a) Spectral decomposition texture in 2-D/3-D seismic section. (b) Frequency determination to increase the vertical or frequency resolutions (e.g., R:11; G:12; B:13).

3.8 Fault Analysis

3.8.1 Throw Analysis

The fault analysis done in this study involves throw and displacement mapping by assessing the faults nature and their association with magmatic sills. Representative faults then were presented in throw profiles consisting of Throw versus depth, T-z and Throw versus distance, T-x (e.g., Muraoka and Kamata, 1983; Barnett et al., 1987; Walsh and Watterson, 1989; Cartwright and Mansfield, 1998; Gawthorpe and Leeder, 2000; Walsh and Timlin, 2003; Pochat et al., 2004; Kim and Sanderson, 2005; Hongxing and Anderson, 2007; Jackson and Rotevatn, 2013; Kamal'deen and Alves, 2014; Osagiede et al., 2014; Mattos et al., 2016; Mohammedyasin et al., 2016). In an isotropic medium, the tip of fault plane is considered to move outwards to different direction allowing a maximum displacement in the older part of the fault plane (Carruthers et al., 2013), while a fault plane that extends to the sediment surface could produce high displacement at the upper tip and generally have gradient value (Carruthers et al., 2013). The throw profile may also indicate the faults that have been established due to compression or extension mechanism (Carruthers et al., 2013). The throws that can be analyzed are throws derived from faults that have an offset in seismic surface, by measuring the difference of hanging-wall and foot-wall cut -off points in two-way travel times (Carruthers et al., 2013).

3.8.2 Displacement Analysis

A fault displacement is related to the variations of slip-parallel strain, referred as layer thickness strain (Muraoka and Kamata, 1983). Faults generally show two different classes based on faults trace (*L*) and displacement (D) pattern, known as mesa-shaped (M-type) and cone-shaped (C-type) (Muraoka and Kamata, 1983)(Figure 3.9). The M-type faults are considered to penetrate through rigid layers and have lateral central section. The M-type faults are considered to move parallel with no significant change in the layer thickness strain (Muraoka and Kamata, 1983). In contrast, the characteristic slopes of the C-type curves typically have uniform layer thickness strain throughout the fault plane. Consequently, these types generally are common in homogenous incompetent layers and soft (Muraoka and Kamata, 1983). Furthermore, the average fault displacement of M-type faults generally is twice that of C-type faults with the same length (Muraoka and Kamata, 1983).
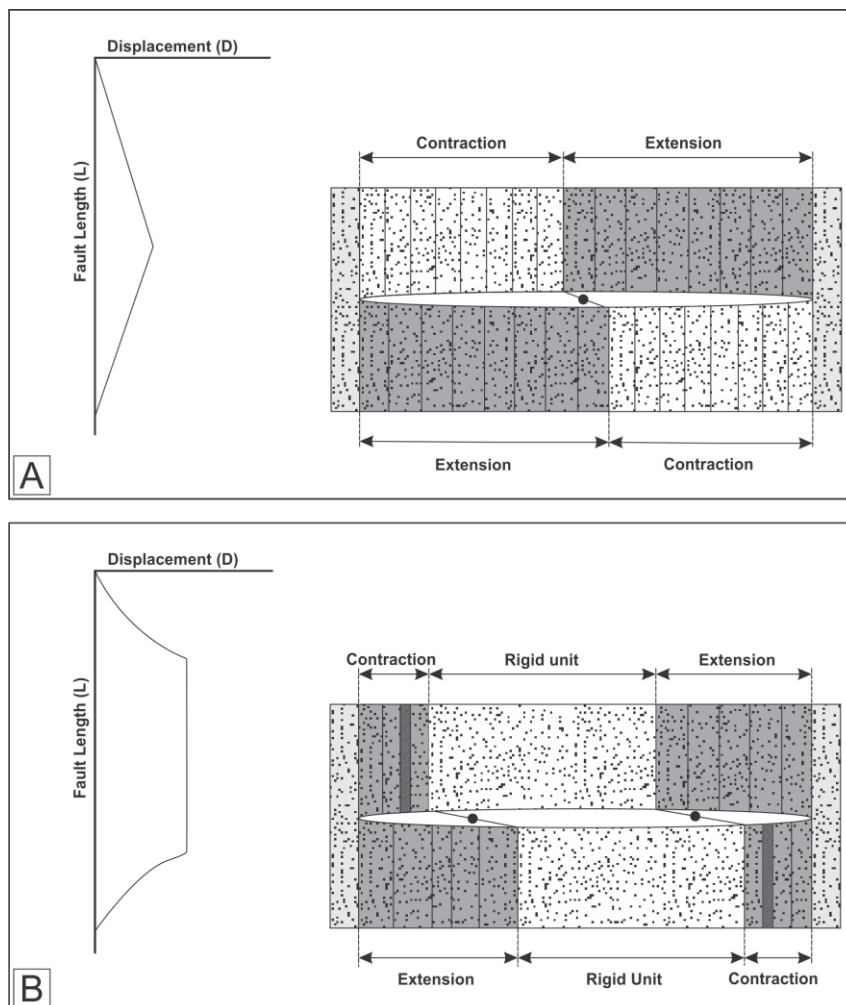
Figure 3.9 – The displacement fault type (redrawn from Muraoka and Kamata (1983)). (a) C-type faults displacement profile with a cartoon showing the strain (right). (b) The M-type faults displacement profile with strain cartoon in the right.

Chapter 4

Results and Interpretations

4.1 Interpreted seismic horizons and units

The major formation tops from well 6706/6-1 (Figure 4.1) have been tied to the seismic data resulting in the interpretation of several seismic horizons and sub-divisions. In the study area, four sedimentary units have been defined from five interpreted horizons that correspond to the tops of the Late Pliocene-Pleistocene Naust Formation, the Early Miocene-Late Palaeocene Kai Formation, the Late Eocene-Oligocene Brygge Formation, the Late Palaeocene Tang Formation, and the Upper Cretaceous-Palaeocene Formation. In general, Unit 4 is interpreted as being un-faulted formation, because most of the faults occurred below Unit 3. Apart from Unit 4, all the other units typically contain magmatic sills and hydrothermal vents.
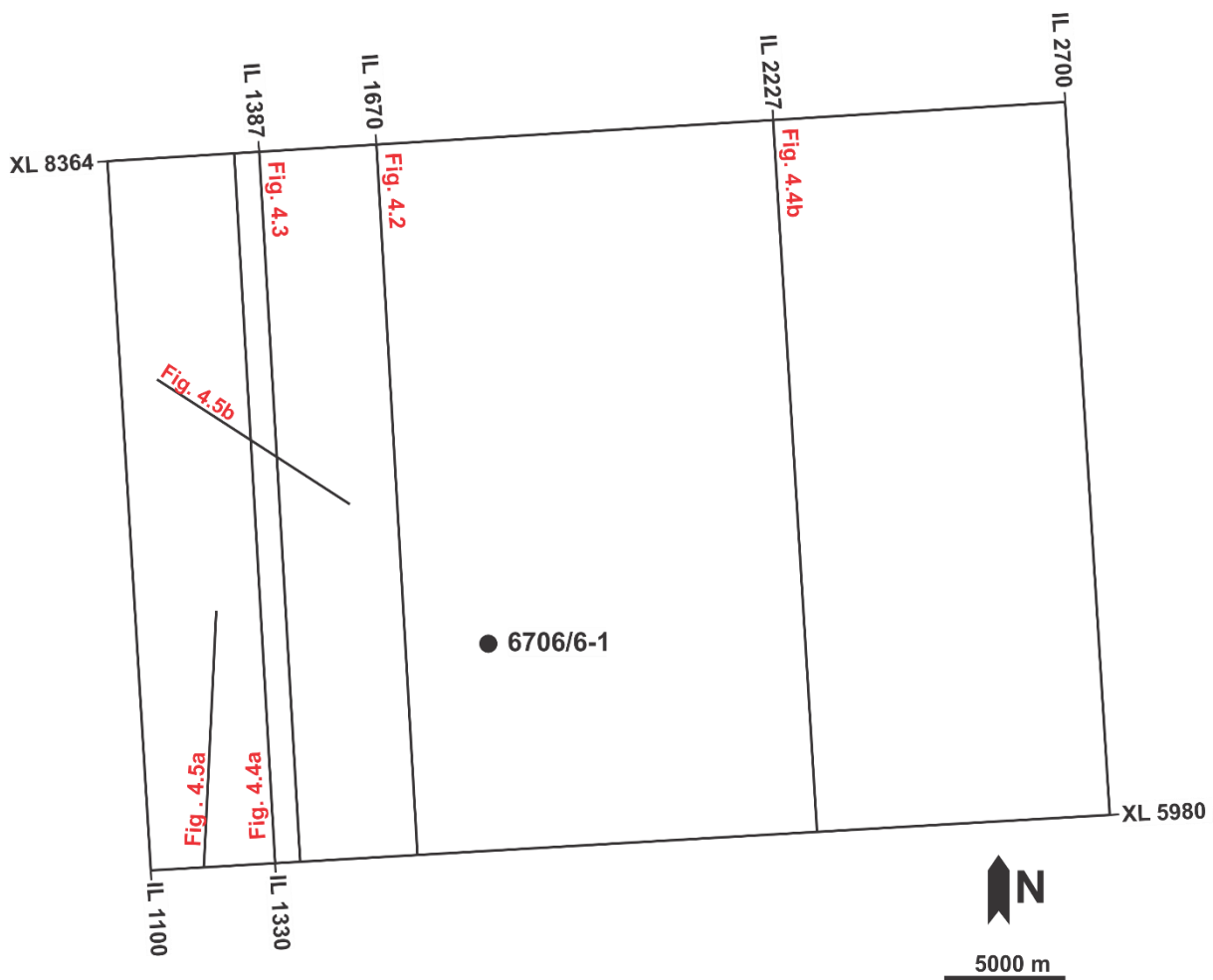
Figure 4.1 – The lines outline the approximate location of the seismic sections in this chapter.

4.1.1 Unit 1 (upper Cretaceous)

On seismic profiles, Unit 1 is situated at the lower boundary of H5, named "No Formal Formation". (NPD, 2015) documented several No Formal Formation in the Vøring Basin as multilayer sandstones. This documentation corresponds with the high amplitude reflection barely below the H5 that typically shows continuity. The upper part of this formation is interpreted to be deposited in Late Cretaceous. The formations within this unit also typically shows staircase-like structure influenced by the extensional faults (Figure 4.2). Further to the north, the seismic profile generally reflects chaotic texture. Based on this appearance, this unit are interpreted as the acoustic basement.
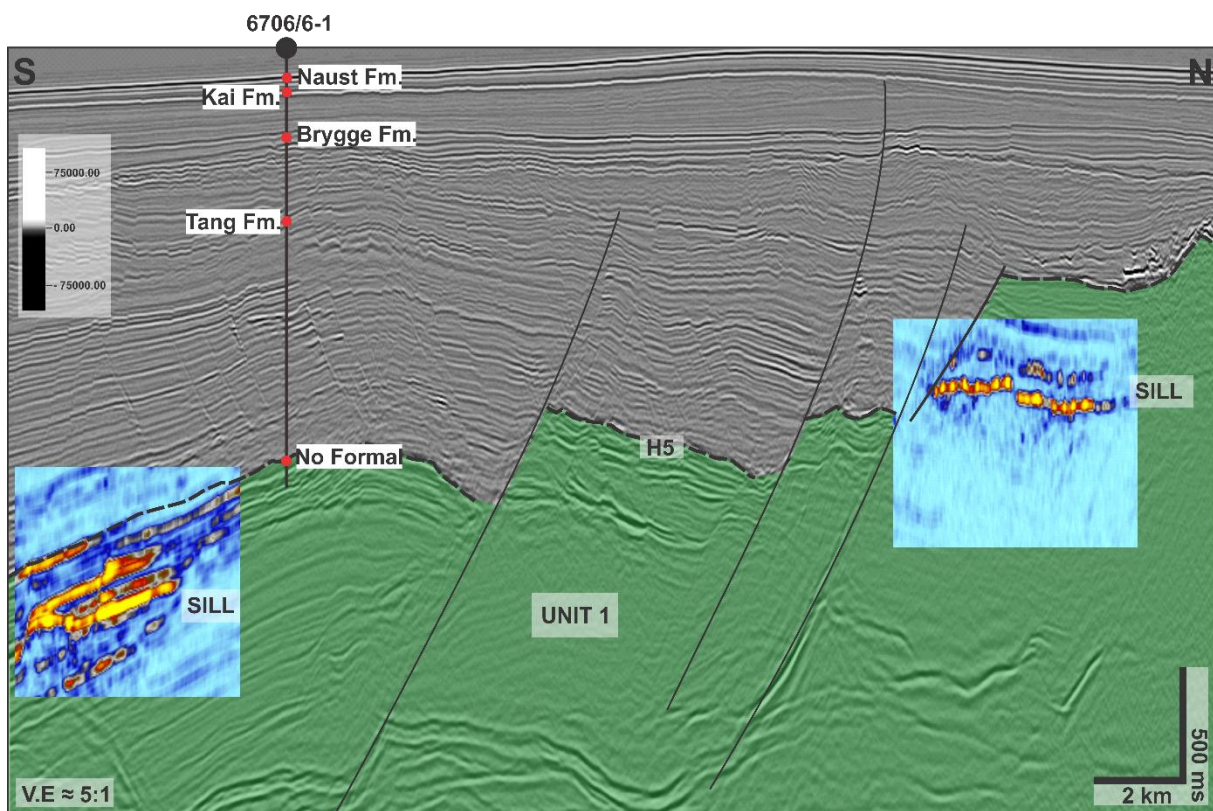
Figure 4.2 – Uninterpreted and interpreted S-N line with well 6706/6-1. The lower boundary H5 is interpreted as the Unit 1 and it intersected by numerous major faults. In this unit, several continuous reflectors could be found at the upper part of the chaotic texture, which may correspond to the presence of multilayer sandstones. Comparison with the RMS attribute indicates that magmatic sills typically have very high amplitude.

Multilayer magmatic sills is also considered to be abundant within Unit 1 (Figure 4.3). Comparison with the RMS attribute, the multilayer sandstones that have high amplitude in normal phase seismic section could separate with multilayer magmatic sills (Figure 4.2). The sill complexes are found at different depth, and have strong connection with the major faults.
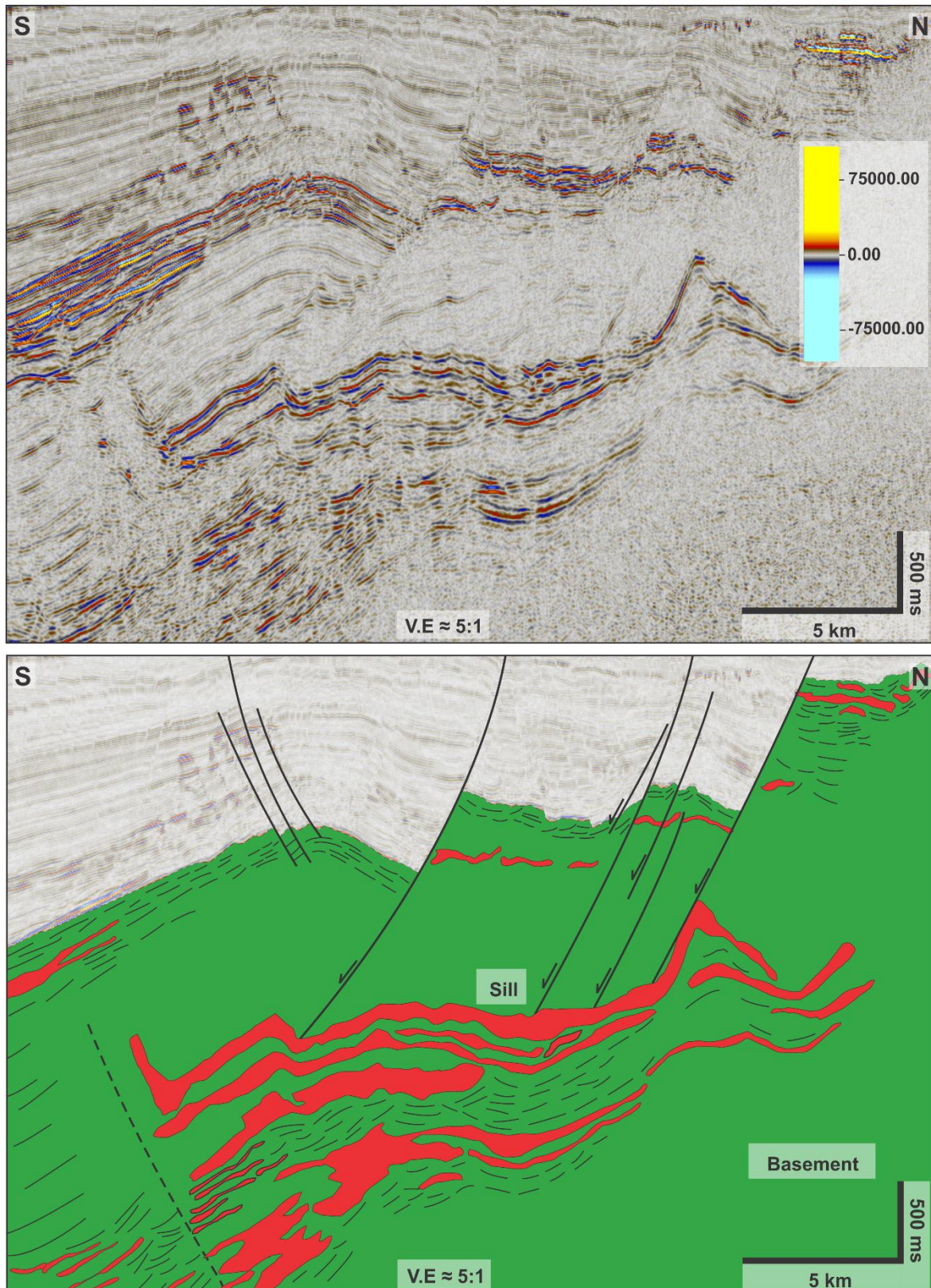
Figure 4.3 – Corresponding seismic section (uninterpreted and interpreted) documenting sill complex structure and association with faults.

4.1.2 Unit 2 (Late Palaeocene to Early Miocene)

Unit 2 is characterized by low to high amplitudes reflection and is bounded by numerous faults. At the lower part of Unit 2 is H3 and upper part of Horizon H5. The horizons H_5 and H_4 correlate with the Tang Formation, found at depth of -2400 ms in well 6706/6-1 (Figure 4.4). The Tang Formation is believed to be deposited in deep marine environment during Palaeocene time (Martinsen and Dreyer, 2001; Hansen et al., 2011), while the lower H_3 and the upper H_4 correspond to the Brygge Formation. The presence of debris flow structure within this horizon, indicates that the formation was deposited on a marine slope (Figure 4.4A).
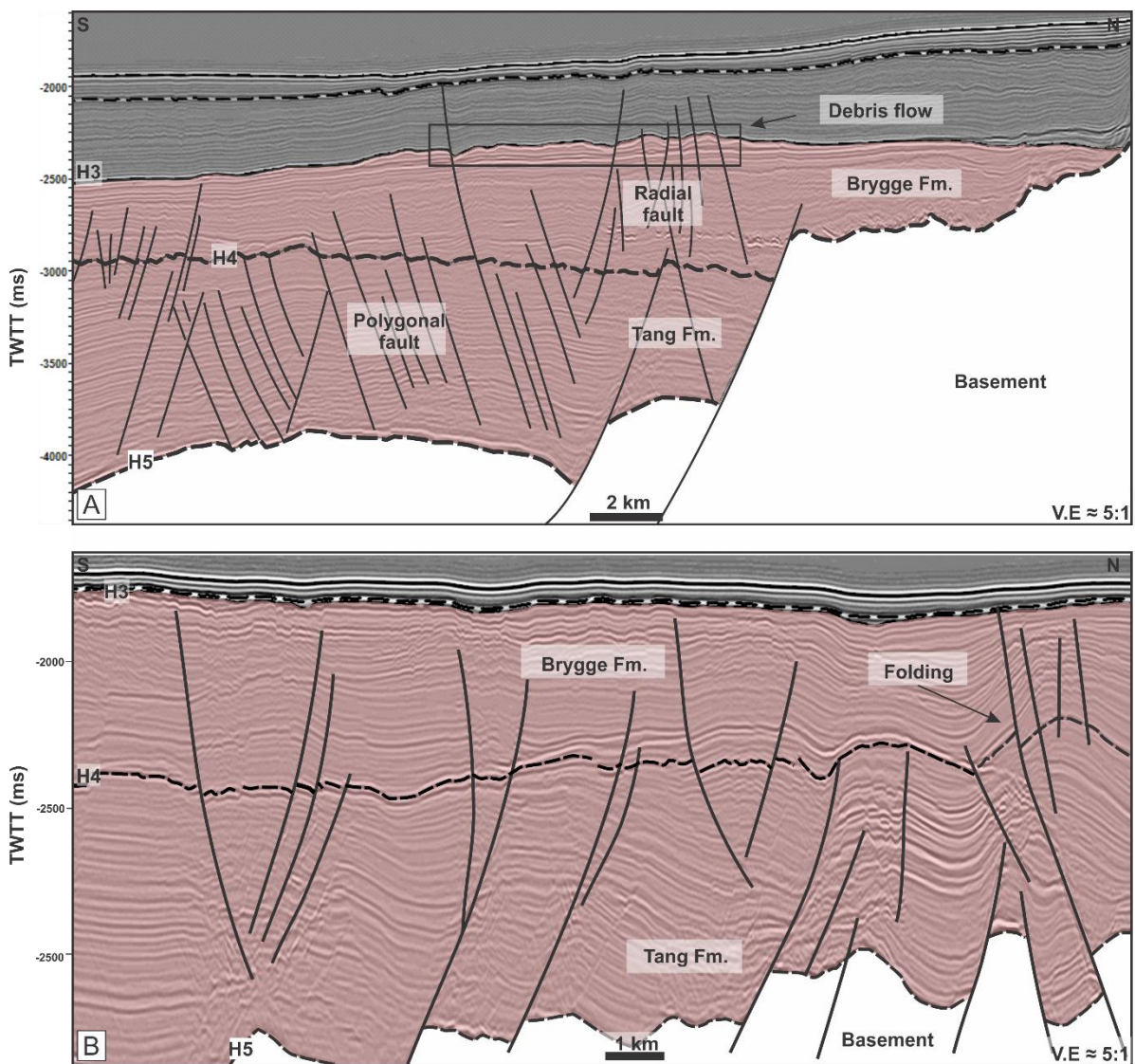
Figure 4.4 – (A) Interpreted S-N seismic sections showing the different formations and fault types (B) Interpreted S-N showing folding within the Tang Fm.

Dalland et al. (1988) documented that the formation contains claystone with minor sandstone, limestone, siltstone, and marl. On seismic profile, the hydrothermal vents are well developed in this formation, typically adjacent to radial faults (Figure 4.5).
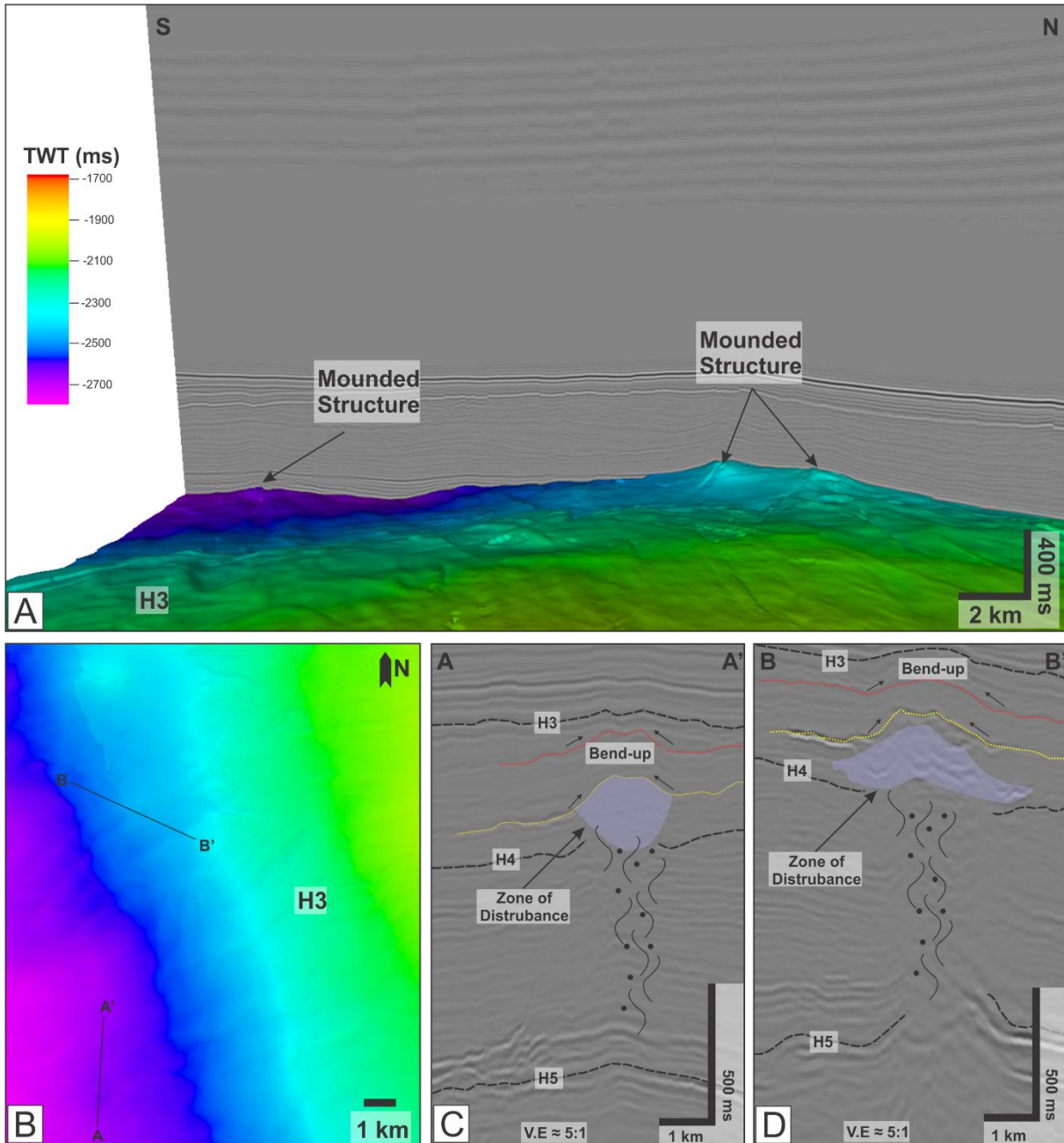
Figure 4.5 – (A) The mounded structure in H3, indicates the onlap of hydrothermal vent. (B) The seismic line highlighting the representative hydrothermal vent within the unit. (c-d) Cross-section A-A' (V-24) and B-B'(V-4), respectively, showing the development of hydrothermal vent complex within the unit.

4.1.3 Unit 3 (Miocene to Pliocene)

The seismic character of Unit 3 includes continuous and low to high amplitude reflections (Figure 4.6A). Unit 3 generally thins to the east and thickens to the western part of the study area. At the lower part of Unit 3 is H2 while its upper is delimited by H3 (Figure 4.6B). Unit 3 is characterized by claystones, siltstones and sandstones with blocky limestone and was deposited in marine setting during the Miocene to Pliocene (Dalland et al., 1988). On seismic section, Unit 3 is dominated by polygonal faults (Figure 4.6C).
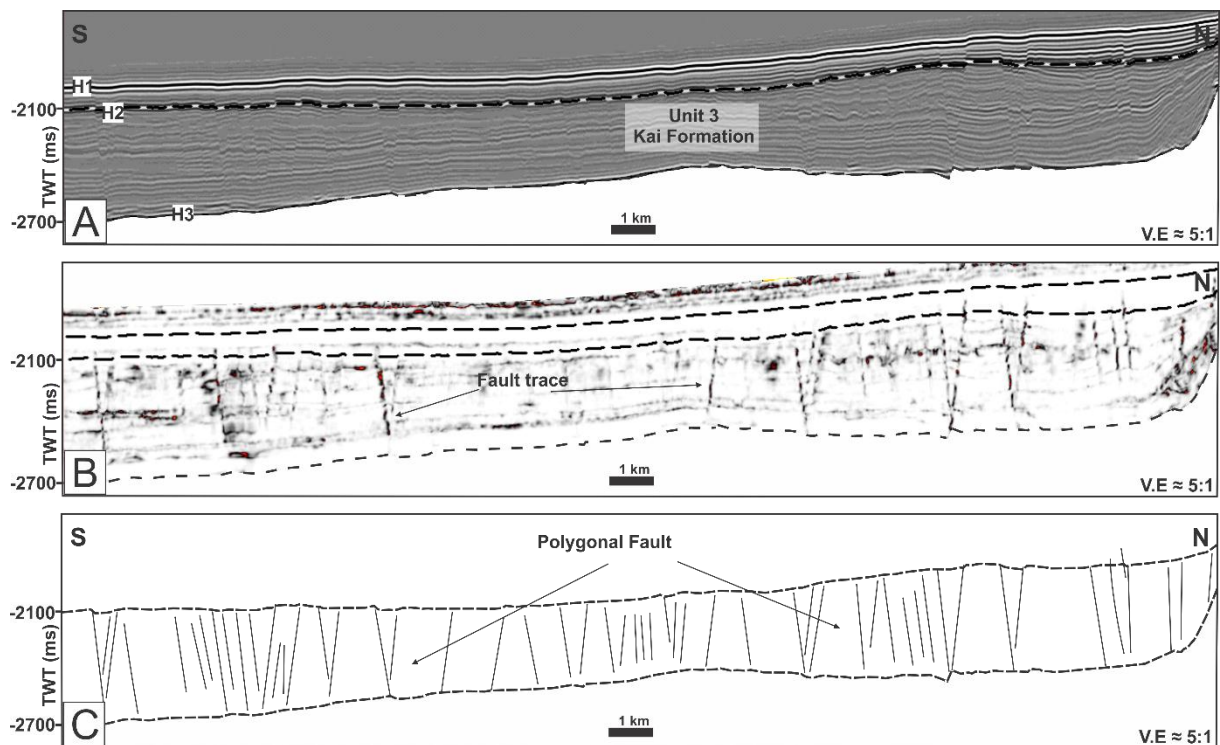
Figure 4.6 – (A) Uninterpreted S-N seismic section using normal phase. (B) Same section using the chaos attribute. (C) Interpreted Inline 1330 showing the unit generally deformed by the formation of polygonal faults.

4.1.4 Unit 4 (Quaternary)

The uppermost unit is Unit 1, which is delimited by high amplitude reflection at its upper and base boundaries. Unit 4 typically thickens toward the southwestern part of the study area (Figure 4.7A). Unit 4 includes glacio-marine sediments (Riis and Fjeldskaar, 1992) mainly clay-rich diamicton that is interbedded with medium to coarse grained sands (Eidvin et al., 1998). Unit 4 is Late Pliocene-Pleistocene in age (Riis and Fjeldskaar, 1992). In SW of the Unit 4, the concave morphology is identified as hemipelagic drape that shows deposition occurred

at low energy environment (Figure 4.7B). The drape is not related to the structure, as the underlying strata appear to be conformable.
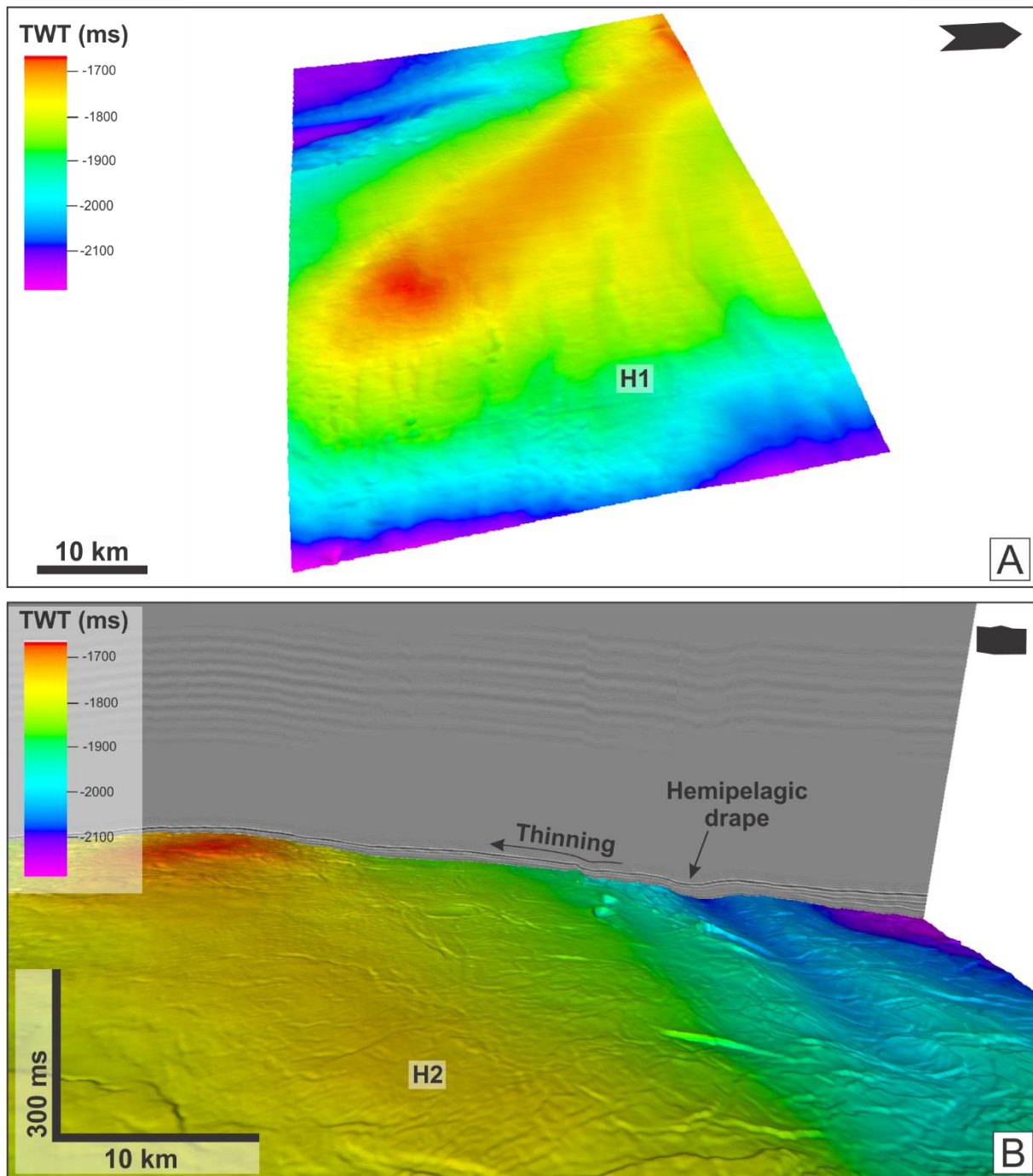
Figure 4.7 – (A) The structural map of horizon H1. (B) A 3-D view of Horizon H2 showing the hemipelagic drape on SW of the Unit 4. The thinning of the strata corresponding with the presence of structural high that has orientation relative NW-SE.

4.2 Interpreted faults

The faults in the study area are dominated by polygonal and radial fault systems (Figure 4.8B). The polygonal faults are considered as a type of normal fault that are well-developed in fine-grained sedimentary rocks with throws ranging from 10 – 100 m (Cartwright et al., 2003). The polygonal faults appear associated with the syneresis process (Cartwright et al., 2003). In contrast, the radial faults in the study have different genesis to the polygonal faults and generally are not related to tectonic activity. Consequently, the radial faults may be related to the stress as the result of local fluid pressure and hydrostatic pressure (Jamtveit et al., 2004). In general, the polygonal and radial faults are well-developed in the Unit 2 (Figure 4.8B).
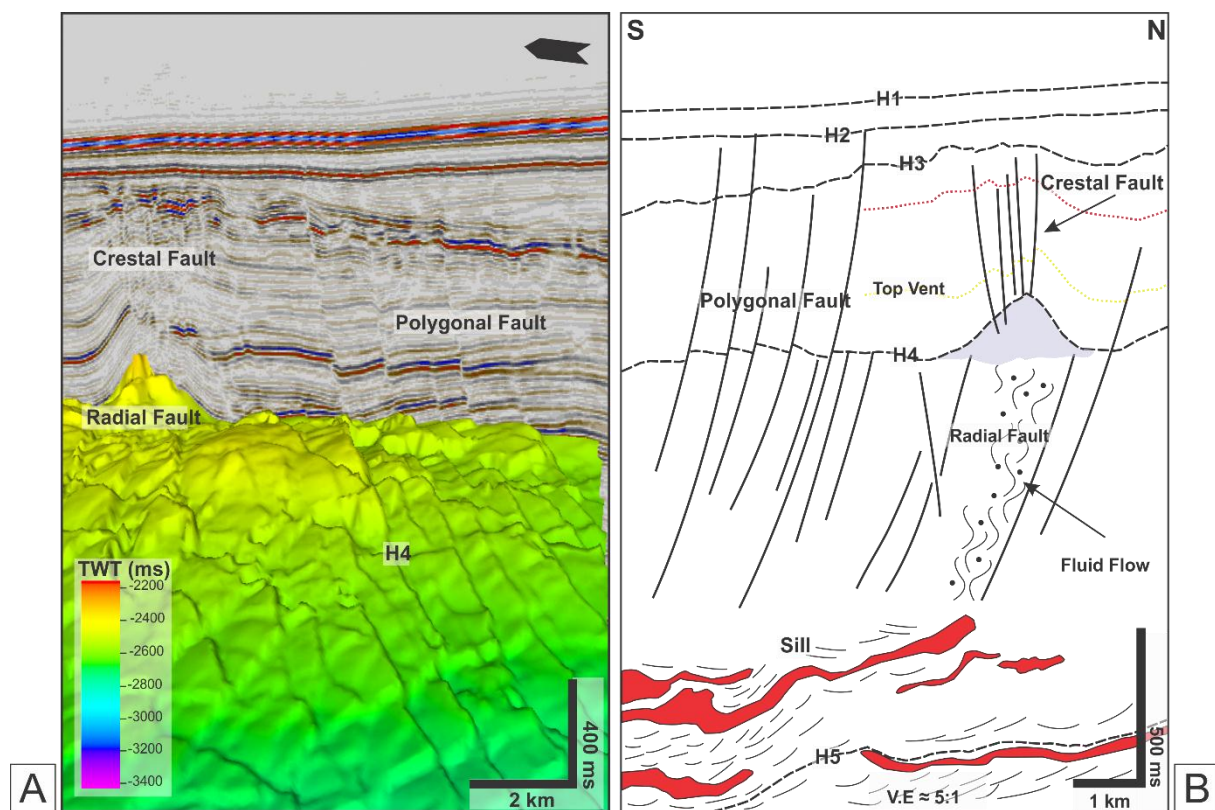
Figure 4.8 – (A) A 3-D seismic profile of horizon H4 indicating the polygonal, radial, and crestal faults. (B) S-N seismic section highlighting sill complex structure and association faults.

Many of the faults generally extend from Unit 1 and are truncated in Unit 4 (Naust Formation). The interpretation of the polygonal fault systems within the formation generally is poorly constrained and sometimes difficult to correlate within the low reflection amplitude seismic interval. Therefore, only polygonal faults that interact with magmatic sills and hydrothermal vents are described in this thesis. Interpretation of 132 faults in this study shows that the

majority of the faults trend in relatively E-W directions and consistently dipping south at angles of 21^0 to 85^0 (Figure 4.9).
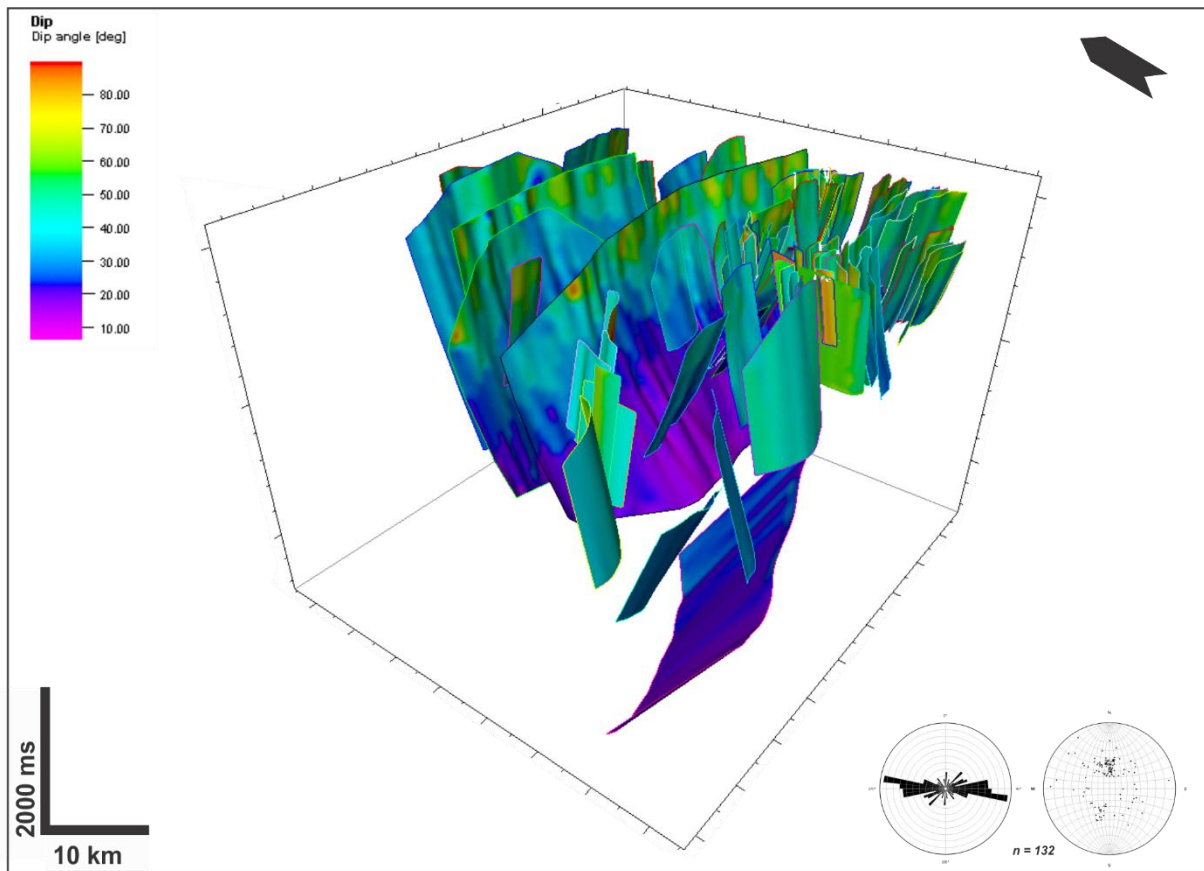
Figure 4.9 – 3-D of fault model using dip properties, showing the orientation of major and minor of 132 fault samples. *The rose diagram expressed the fault strikes and equal angle plots.*

The connection between magmatic sills and fault systems in the study area is further investigated as the faults are perceived as feeders or conduits for the emplacement of magmatic sills at either deeper or shallow depth. Offset of stratigraphic formation as the result of fault displacement perhaps have restructured the sill morphologies creating the formation of minor intrusive steps (Magee et al., 2013a). Therefore, fault interpretations in this thesis have been divided into two categories. The first category is about the seismic interpretation of magmatic sills related fault systems which comprises of looking at sill geometries, fault-sill interactions, and throw-displacement variations. The second category is seismic interpretation of the hydrothermal vent-related radial and crestal fault systems where the geometries of the hydrothermal vents are investigated. Also, included in this interpretation are vent-radial fault interactions and identification of crestal above hydrothermal vents.

4.2.1 Seismic interpretation of the sills related fault systems

4.2.1.1 Geometry of sill intrusions

High to very high contrast of amplitude reflection compared to the sedimentary host-rock strata on seismic sections characterizes magmatic sills or intrusions (Hansen et al., 2004; Hansen and Cartwright, 2006b; Hansen and Cartwright, 2006a; Schofield et al., 2012; Magee et al., 2013a; Magee et al., 2013b; Magee et al., 2013c; Magee et al., 2015; Magee et al., 2016; Mattos et al., 2016; Omosanya et al., 2016; Omosanya et al., 2017). Thirteen magmatic sills associated with hydrothermal vents were interpreted in the study area. Different sill-sill interactions are identified based on sill-sill junction types (Figure 4.10). At depth of 3.5-5 ms (TWTT), the sills form a network of interconnected sill complex. Some emplacement of magma may have intruded along the thick pre-existing faults, established the formation of inclined sheets as it is shown in Figure 4.10B.iii. Here, a C-junction is formed at the point of contact between the sill and the fault.
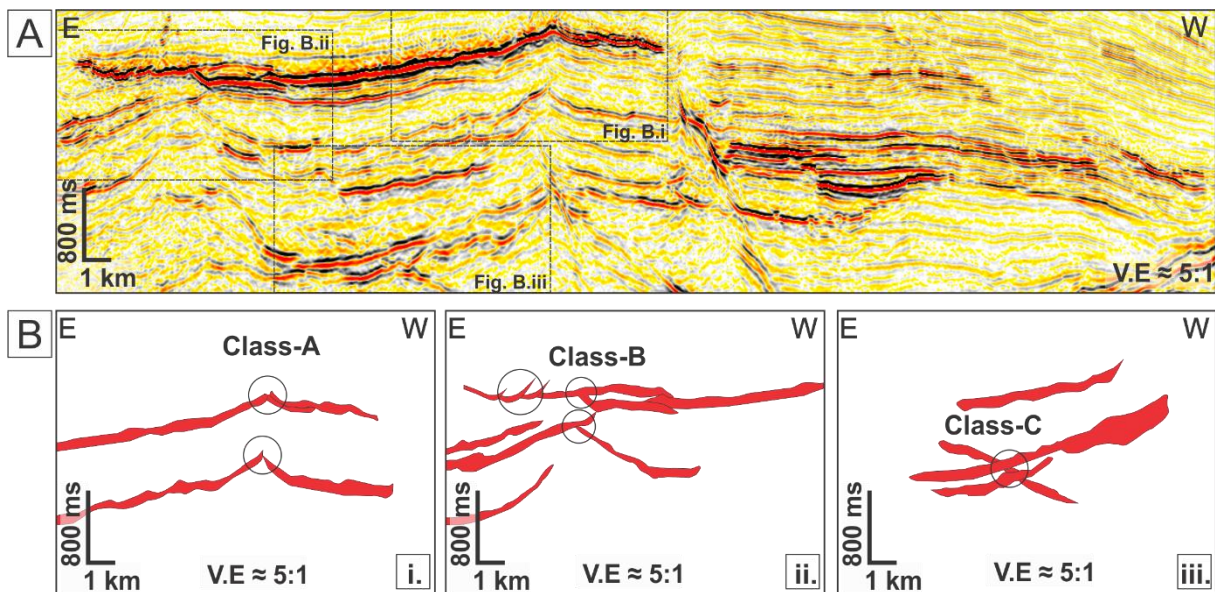
Figure 4.10 – Representative E-W seismic line (uninterpreted and interpreted) showing the formation of magmatic sill junctions.

Based on depth of occurrence, the thirteen magmatic intrusions are divided into three categories, which include shallow sills at depth less than 3.5 ms (TWTT), intermediate sills at depth of 3.5-5 ms (TWTT), and deeper sills at depth more than 5 ms (TWTT) (Figure 4.11). Sill geometry in the study includes saucer-shaped sills e.g., Sill E (Figure 4.11 b, d), transgressive sills e.g., Sill A (Figure 4.11 a-c) and shallow dipping sills e.g., Sill M (Figure 4.11 a-b).
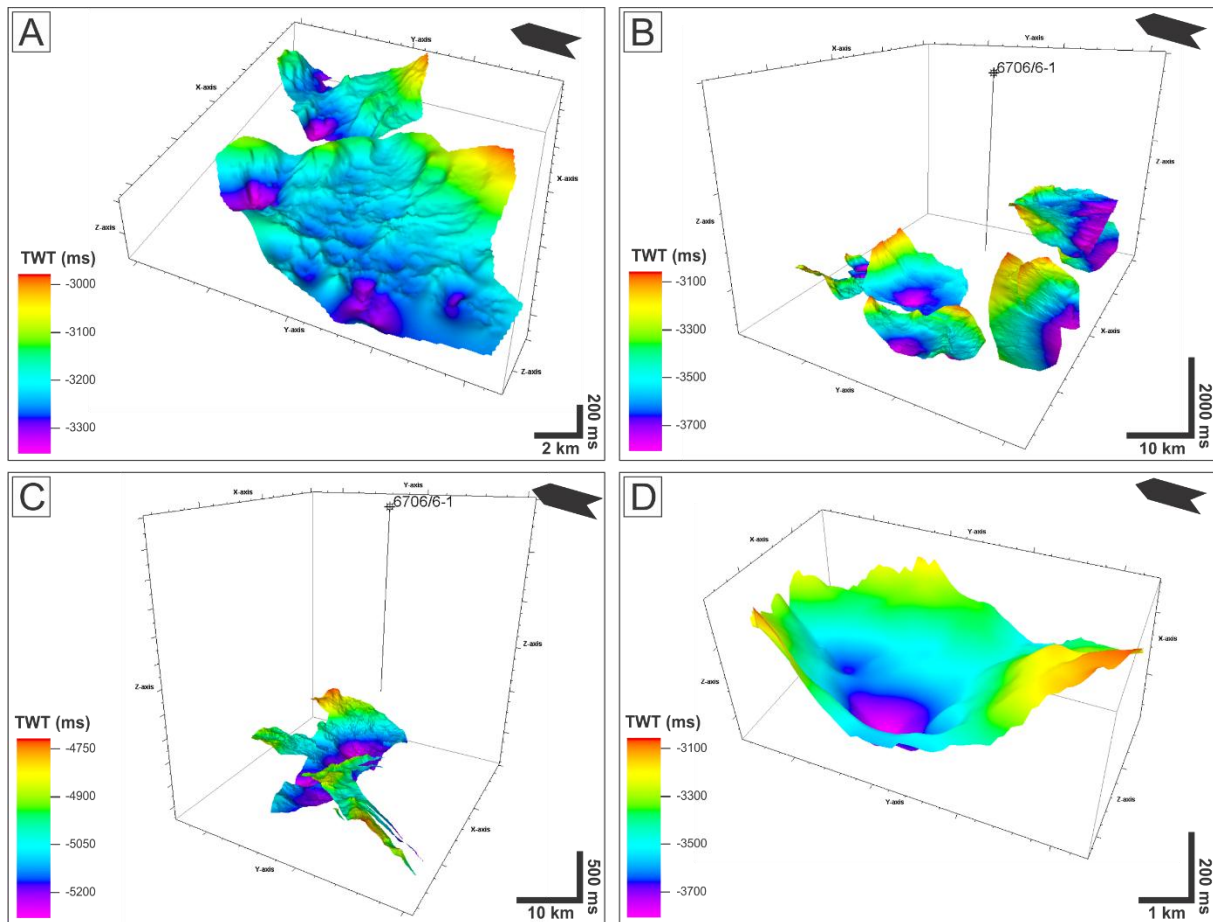
Figure 4.11 – A 3-D view of magmatic sills in the study area. Classification of sills was based on their depth of occurrence into (A) shallow sills (B) intermediate sills and (V) deeper sills. In addition, a common sill geometry in the study area is (D) saucer-shaped morphology.

The concave-upwards or best known as saucers-shaped sills are mostly found at depth of more than 3 ms (TWTT) (Figure 4.11D), whereas the shallow dipping sills can be found at different depths (Figure 4.11a-c). The statistical analysis of the area coverage of magmatic sills in this study shows that the sills are spread widely at different depths. The shallower sills cover areas ranging from 15.2 to 94.3 km^2 with lengths from 24.7 to 58.8 km (Figure 4.12). The intermediate sills have areas ranging from 8.8 to 186.4 km^2 and lengths of 24.7 to 58.8 km (Figure 4.12). The area coverage and lengths of the deeper sills ranges from 48.4 to 186.4 km^2 and 100.7 to 121.2 km, respectively (Figure 4.12).
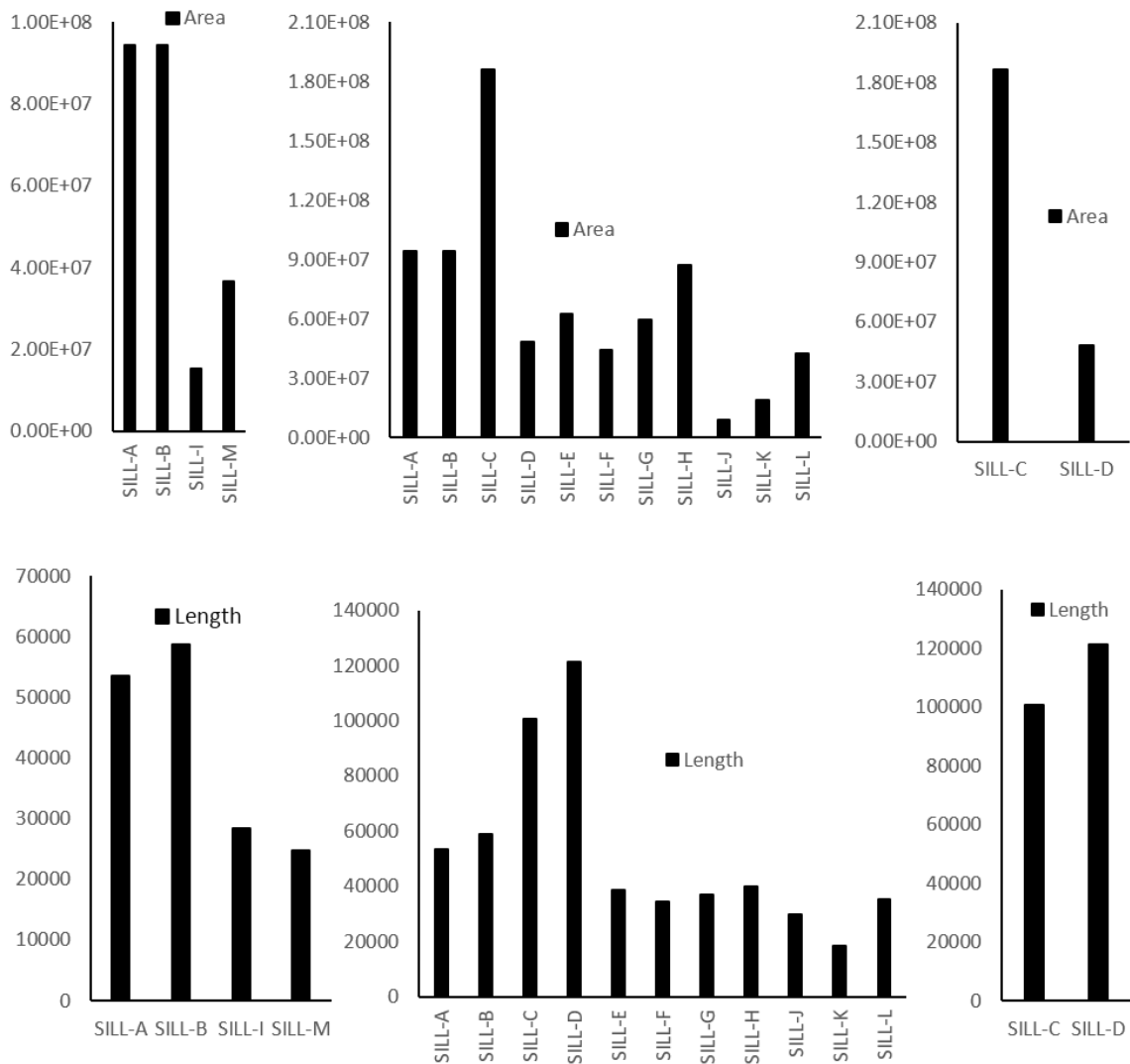
Figure 4.12 – Histogram showing the areas and lengths of the magmatic sills at shallow, intermediate, and deeper depths (left to right).

4.2.1.2 Fault-related magmatic sills

Sill-A is a saucer-shaped sill that advances ~94.3 km^2 in NE-SW direction (Figure 4.13D). Malthe-Sorensson et al. (2004) documented that the saucer-shaped structure is generated as a result of sill interaction with the overburden. The magmatic penetration within the overburden introduces stress heterogeneities that affects the dimension of the emplaced sill. Sill-A was interpreted based on its very high amplitude reflection within seismic profile and selected for further study because of its inter-relationship with various faults (Figure 4.13 A-B). The sill has a concave-upward geometry in the middle and with an inclined sheet. Twelve faults (F60-F71) were identified associated with Sill-A. These faults are normal and synthetic faults (Figure 4.13) and generally strike E-W, with southerly dip of 25°-80° (Figure 4.13C). These faults intersect into Sill-A creating an accommodating zone for the magmatic sill to intrude.
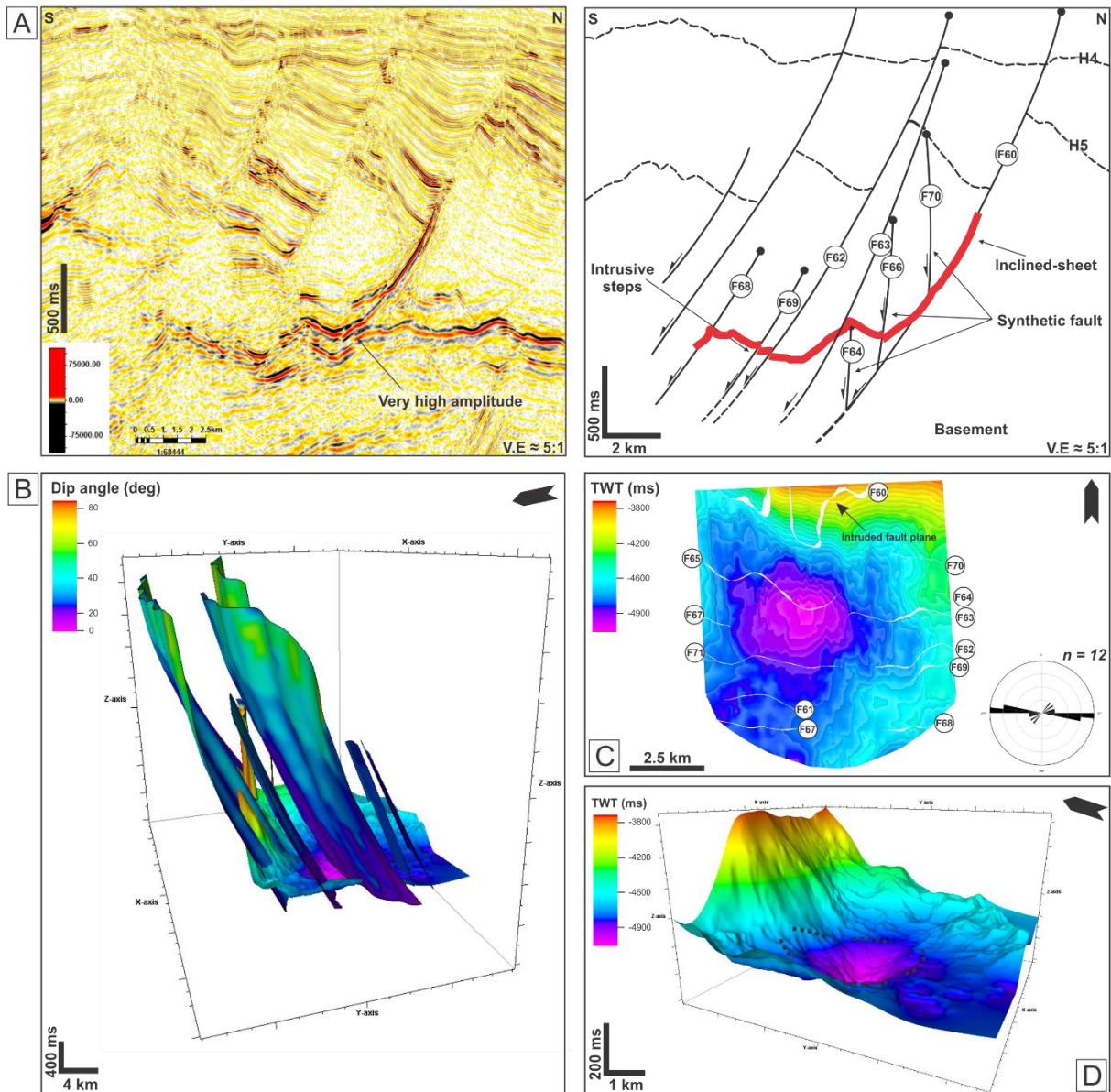
Figure 4.13 – (A) Interpreted N-S Inline 1830. (B) A 3-D diagram showing the cross-cutting relationship between Sill-A and the faults (C) A 2-D map showing the fault trends are E-W and with dip of 25°-80°S (D) A 3-D of Sill-A morphology. Dash lines represent the intrusive steps.

Sill-A is well-imaged contiguous to the fault. The throw plots i.e., throw-depth (T-z) and displacement (D-x) for these sills are shown in Figure 4.14 and Figure 4.15. For the throw and displacement plot, faults F64 and F70 are not included because these faults have minor influence on the geometry of Sill-A. The throw-depth (T-z) plots of the faults generally increase northward but show an increase and decrease in throw due to fault segment linkage (Magee et al., 2013a). The average fault throw is 23.6 m with the maximum throw (T_{max}) reaching up to 165 m (Figure 4.14). Maximum throw could be associated with F60 toward the upper tips where the inclined-sheet is.

Figure 4.14 – Fault throw versus two-way travel time (depth) for fault F60-F71 intersecting Sill-A. Fault throw is display in meter, while the depth (z) in ms (TWT). The red dot indicates the throw maxima, whereas the blue dot represents the minimum throw values.

Figure 4.15 – Fault displacement versus distance along fault within Sill-A. Distance along the fault and fault displacement are shown in meters. The dash lines indicate minimum displacements and segment linkage. S1 to Sn and dotted lines distinguish fault segments.

Fault throw generally decreases gently toward the basal tip with gradients of 3.9^0. Furthermore, the Displacement-length (D-x) plots of the ten faults are shown in Figure 4.15. Based on the plots, the fault displacements are dominated by M-type profiles. Fault F60 is typically difficult to interpret because it contains M- and C-type profiles. The C-type faults are represented by fault F69 and F66. Faults that laterally have segmented fault include F65 with seven segments, followed by F60, F67, and F71 with five segments. F69 has the least with only two segment, while the rest of the faults have three segments. The Displacement maximum (D_{max}) ranges from 482 m (F71) to 50 m (F68), while fault length ranges from 10.3 km (F60) to 1.2 km (F69). Parallel to the north, significant intrusive steps are linked to F65 and F71 before changing into an inclined-sheet along F60. Near the concave-upward geometry, F71 has T_{max} ~60m and D_{max} 482 m at fault length of ~5 km, whereas F65 has T_{max} ~62m and D_{max} 402 m at fault length of ~3.6 km. The inclined-sheet further to the northern rim transgresses for ~600 ms (Figure 4.13D) and intruded F60 before feeding the upper formation (Figure 4.13A). The magma flow within the inclined-sheets may propagate westward, which is relatively consistent with the orientation of the long-axis of intrusive steps in the footwall of F71 and F65 (Figure 4.13C).

Relative to Sill-A, Sill-B is probably formed in response to fault stress associated with magmatic-driven pressure failure in the formation, leading to horizontal propagation of magmatic sill that is sub-parallel with σ_1-σ_2 (Walker, 2016). The horizontal propagation may also be associated with stress asymmetry that is formed because the length of the horizontal segments are more than two to three times of the overburden thickness. Sill-B is emplaced at intermediate depth, covering ~170 km^2 in area in NNE-SSW direction and is situated in western part of the study area. Fourteen faults (F72-F85) that were identified have interaction with Sill-B and are all normal faults (Figure 4.16A). These faults strike in E-W direction, relatively dipping south at average 40° and showing undulated fault traces (Figure 4.16A-C). The direction of magmatic Sill-B is coincident with the faults direction (Figure 4.16D). F80 and F79 are preferentially oriented in the same direction as the intrusive steps in the southern part of the study area (Figure 4.16c). The steps create offset with maximum throw (T-z) ranging from 23 m to 54 m and maximum displacement (D-max) from 39 m to 93 m (Figure 4.17 and Figure 4.18). This is likely caused the reorientation of the magma flow direction to NNE-SSW parallel to the fault trend.
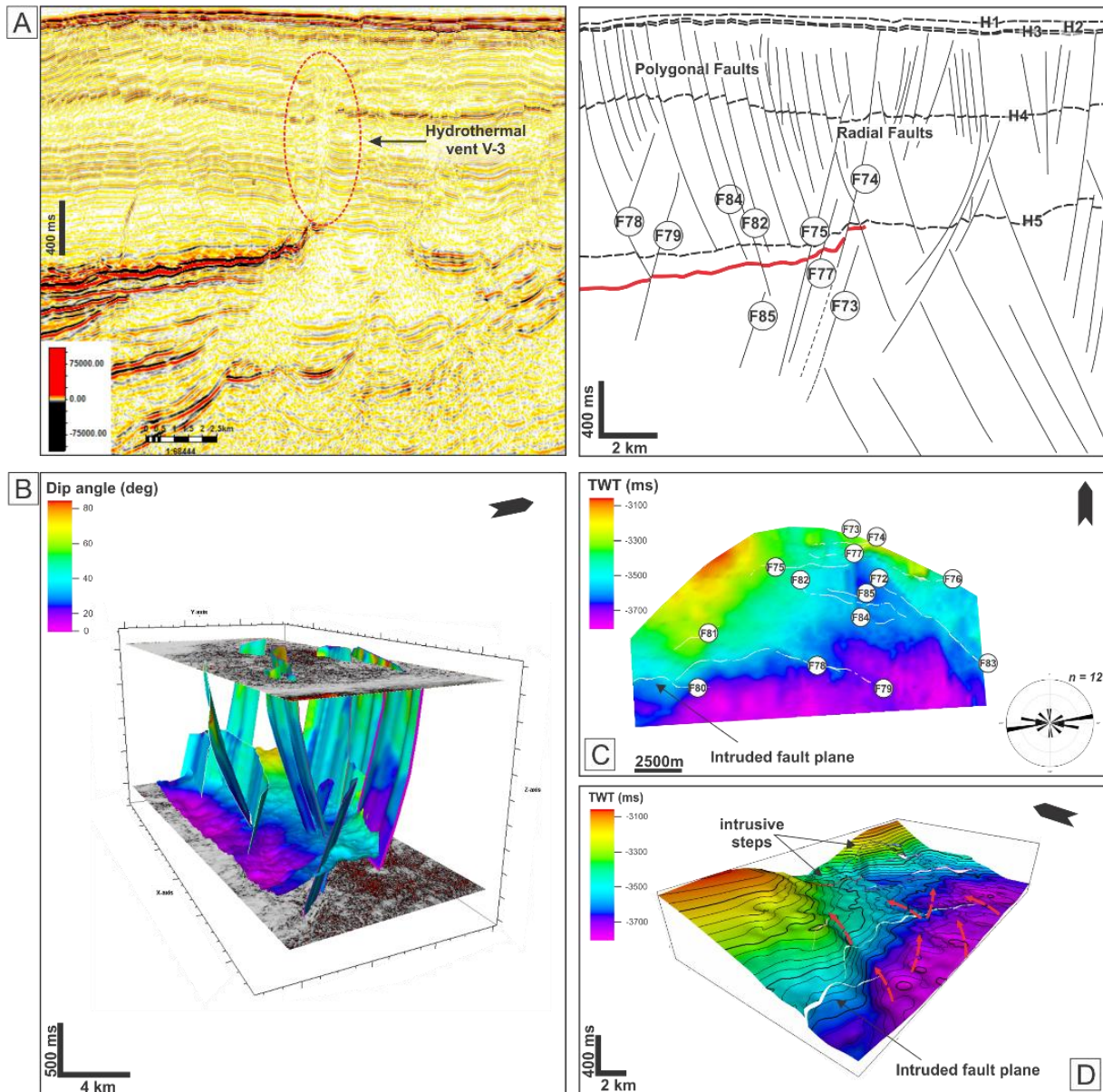
Figure 4.16 – (A) Interpreted N-S seismic lines of Inline 2310. (B) A 3-D figure showing how Sill-B crosscuts the normal faults (C) A map showing that fault orientation is E-W. (D) The magma flow is inferred to be dominantly in NNE-SSW direction (red line).

Based on the displacement plots in Figure 4.18, the fault displacements are dominated by C-type profiles. Fault F75 represents the M-type, while the displacement for F72 and F73 are unable to be identified. The rest of the faults have C-type profiles. There are three faults that have two segments, represented by F74, F75, F76, whereas F79 consists of one segment. In contrast, the other faults do not have any segments. Farther to the northeast, offset of Sill-B generally become smaller, with fault throws and displacements being less than 6 m. The decrease in fault throws and displacements may occur as a result of change in bulk grain size of adjacent formations (Dewhurst et al., 1999) that control the formation of the Sill-B.
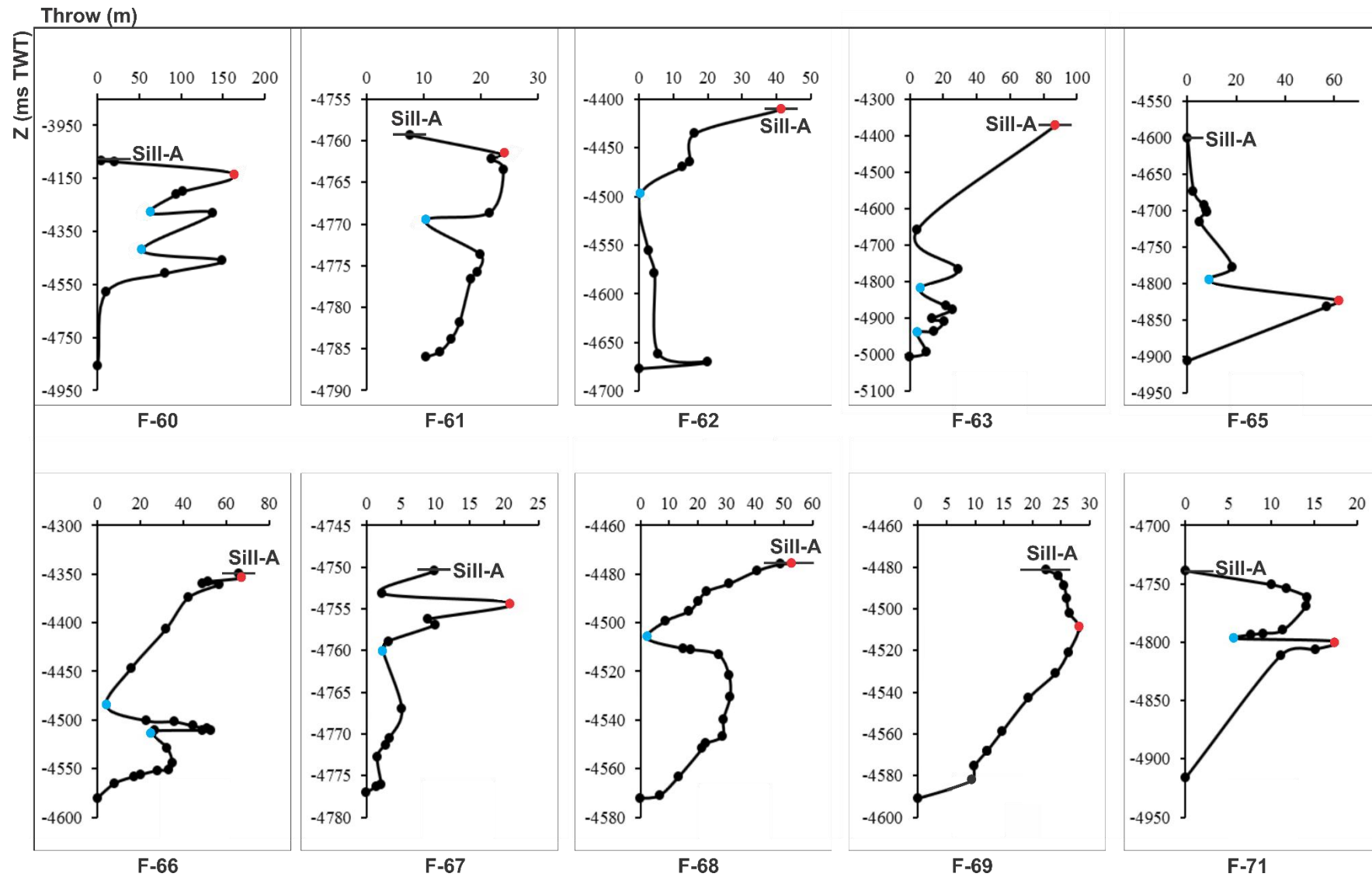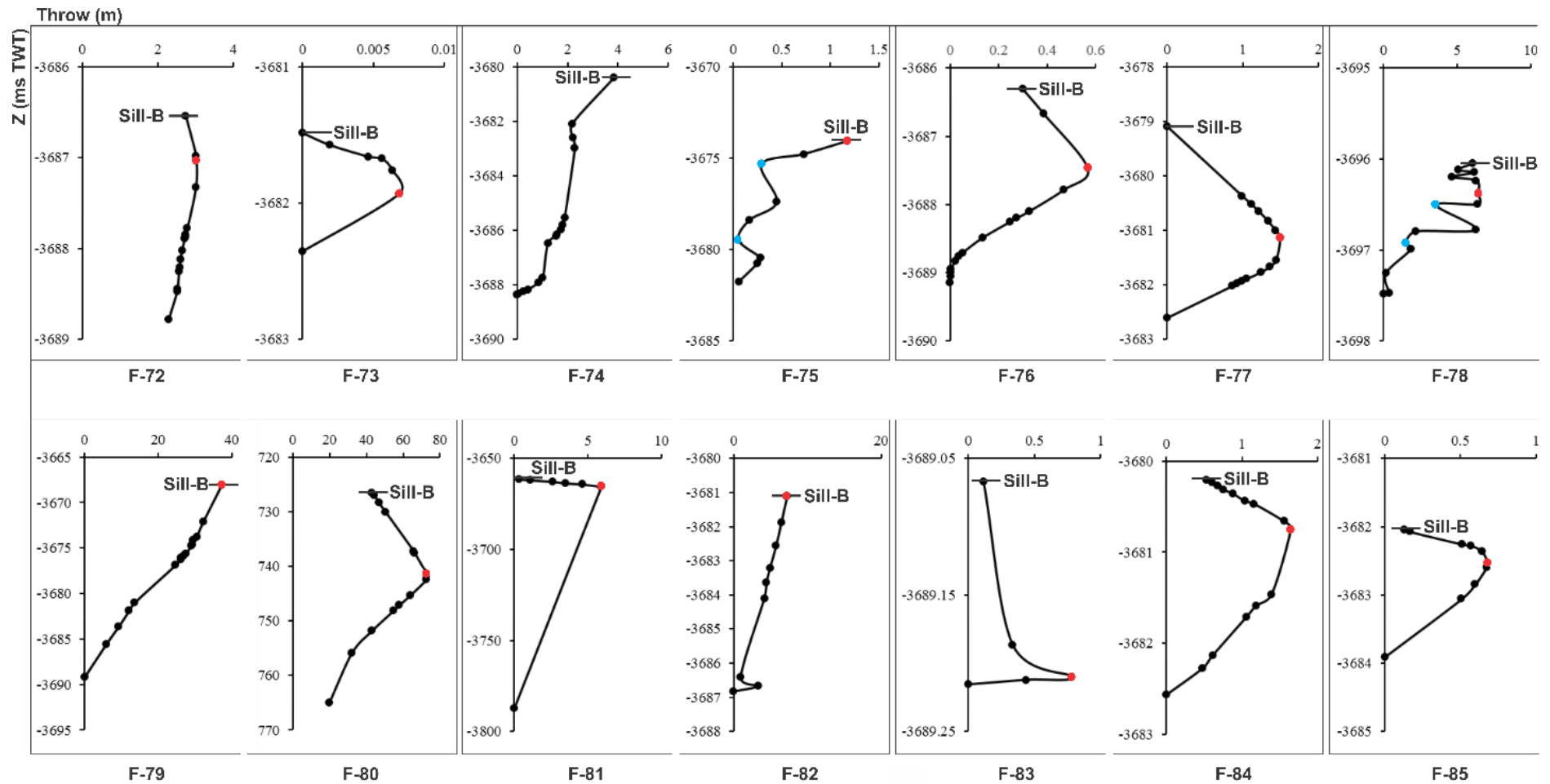
Figure 4.17 – Fault throw versus two-way travel time (depth) for fault F60-F71 intersecting Sill-B. Fault throw is displayed in meters, while the depth (z) in ms (TWT). The red dot indicates the throw maxima, whereas the blue dots represent the minimum throw values.
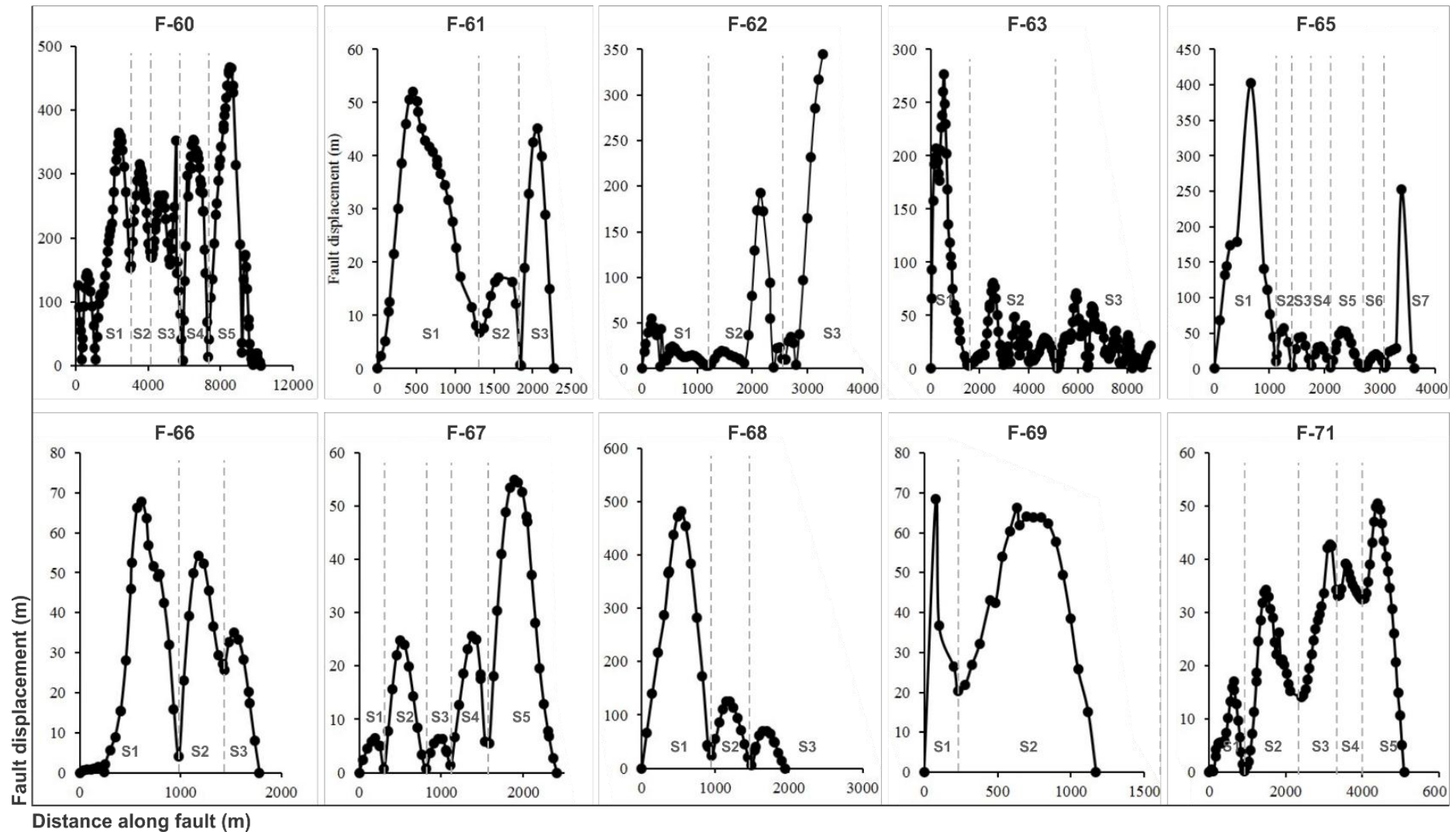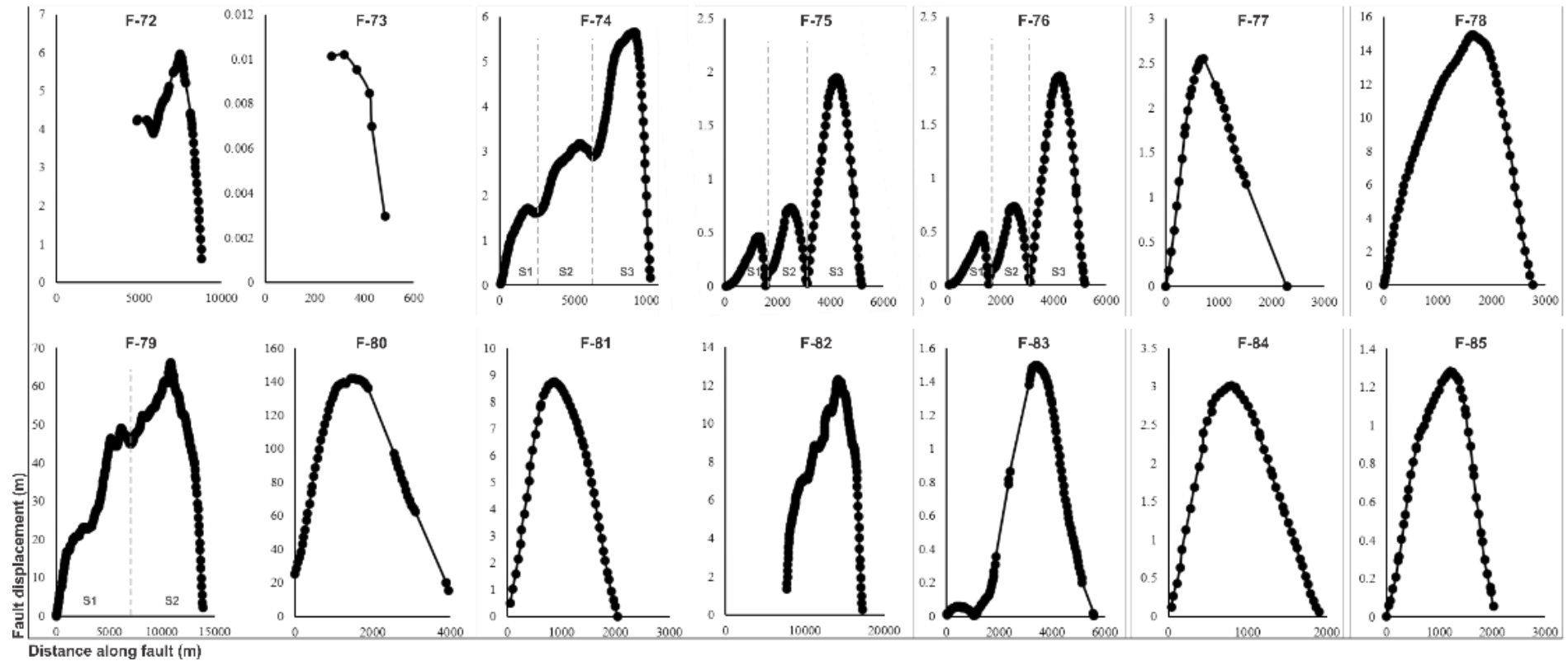
Figure 4.18 – Fault displacement versus distance along fault within Sill-B. Distance along the fault and fault displacement are shown in meters. The dash lines indicate minimum displacements and segment linkage. S1 to Sn and dotted lines distinguish fault segments.

4.2.2 Seismic interpretation of the fault systems related to hydrothermal vents

4.2.2.1 Geometry of the hydrothermal vents

Twenty-nine hydrothermal vents (Figure 4.19) were identified in this study and were typically developed at two stratigraphic formations, the Brygge and Tang Formations. The vents in general are common in the western and southeastern part of the study area (Figure 4.19). Correlation with exploration well 6706/6-1 indicates that the shallower vents are Late Palaeocene-Oligocene in age while the deeper vents are Late Palaeocene. On the three-dimensional (3D) seismic data, the upper parts of the vents are dome-, eye-, and crater-shaped (Figure 4.20). On seismic section, the vents were identified as low amplitude, vertical, thin zones. Using the chaos attribute, the vents typically are shown as high amplitude reflections suggesting their distinct compositional variation relative to the host-rock strata and the lack of organization or chaos along their paths. The overburden relationship generally is concordant or divergent whereas the basal relationship is down-wrapped concordant.
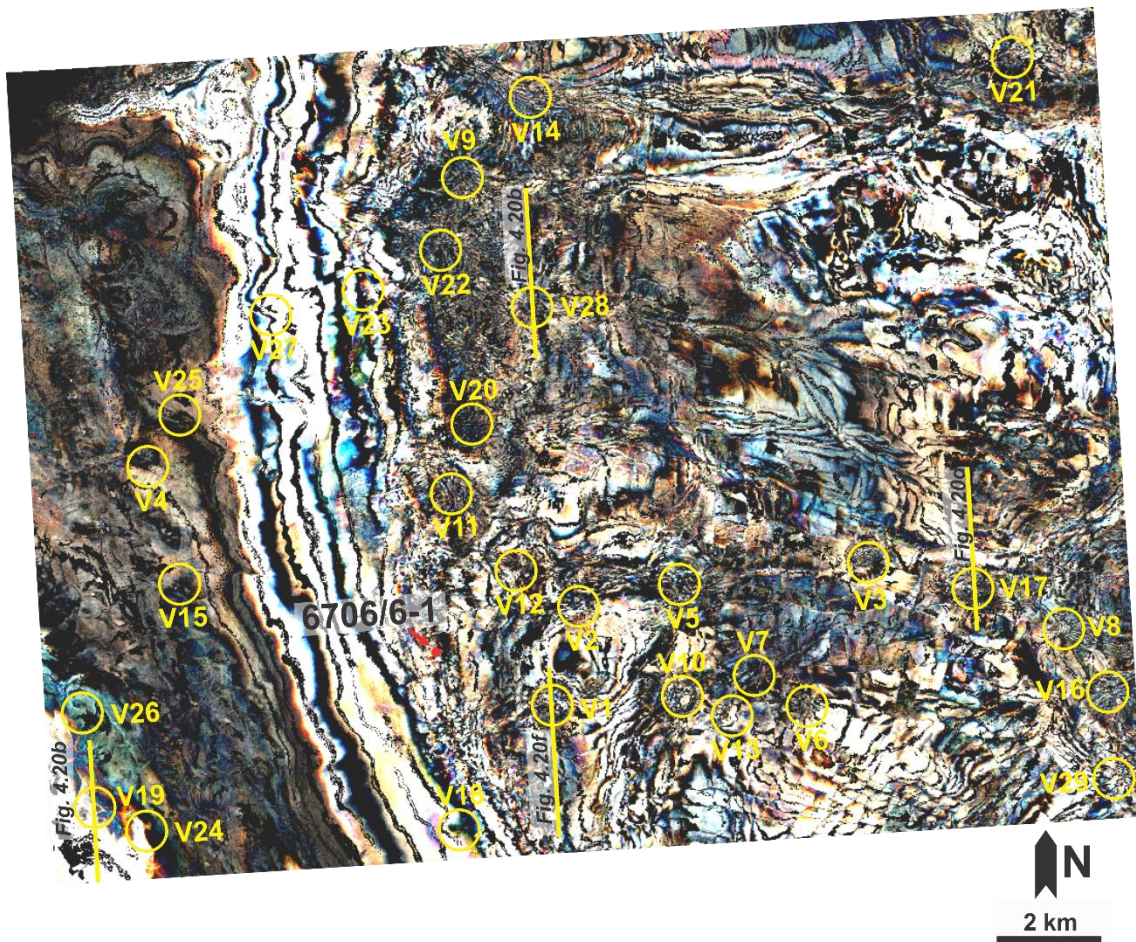
Figure 4.19 – Spectral Decomposition slice at depth -2150 ms showing the distribution of hydrothermal vents in the study area. Morphologically, the hydrothermal venting shows circular to elliptical features in plan view.
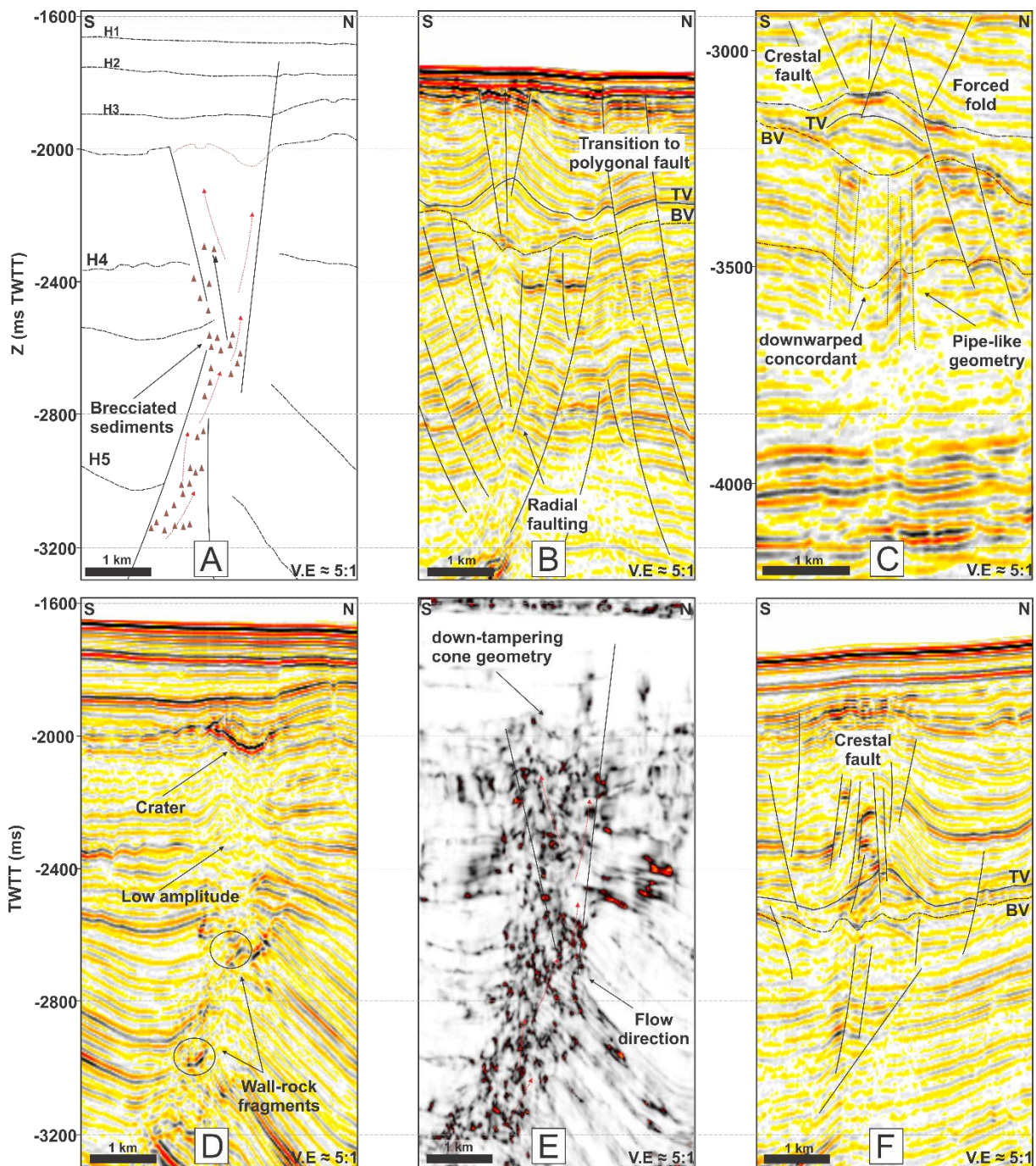
Figure 4.20 – (A) A cartoon of V-17 highlighting the crater-shaped, brecciated sediment and radial fault (B) V-28 adjacent to radial faulting. (C) V-19 shows the eye-shaped geometry, forced fold, pipe-like or columnar geometry. The inter-relation between the formation and the vent is down-warped concordant. (D-E) V-17 has crater morphology with down-tampering cone geometry downward. Amplitude reflection from chaos attribute showing the fluid move upward that was interpreted forming brecciated sediments. (F) Hydrothermal vent V-1 showing the dome-shaped geometry with crestal faults above the vent.

Interpretation of the seismic also indicates that the vents have their lower parts at the tips of the underlying sill complex and interact with numerous faults (Figure 4.20). The faults include

polygonal, radial, and crestal faults (Figure 4.20). Within the pipe of the hydrothermal vent is considered to be brecciated sediments (Figure 4.20D). Based on the size, the hydrothermal vents are divided into three (3) categories: less than 3 km, 3-5 km, and more than 5 km (Table 4-1). The majority (>60%) of the vents developed with eye-shaped geometry, with down-tampering (>55%) are the dominant downward structures (Table 4-2). Specifically, the small (<3 km) and intermediate (3-5 km) hydrothermal vents are the most widespread, the large (>5 km) vents are mostly found near the inner part of the study area.

Table 4-1 – Hydrothermal vent complex statistics.

Shape/Size	<3 km	3-5 km	>5 km	Total
Eye	10	7	3	18
Dome	3	4	1	8
Crater	2	1	0	3
n	15	11	4	29

The minimum diameter of the upper part of the hydrothermal vent were 1.9 km to 5.7 km, while the diameter varies from 2 to 2.6 km, with an average of about 2.1 km. Furthermore, the average diameter of vents at 3-5km and >5 km are 3.9 km and 5.3 km, respectively. Mounds are also formed in the study area and present in the Paleogene sequence above the upper part of hydrothermal vents.

Table 4-2 – Statistics of hydrothermal vent structures.

Structure	Total
Down-tampering cone	17
Pipe-like/columnar	11
Fault-related	1
n	29

The relationship between the depth and the radius of interference (r) shows that the down-tampering cones generally have negative trend (e.g. V-1, V-8, V-19) with coefficient of determination (R) ranging from 0.187 to 0.99 (Figure 4.21). The pipe/like or columnar typically have positive trends (e.g. V-4, V-10, V-12) with R advance from 0.83 to 0.98 (Figure 4.21). The plot for V-11 shows that the coefficient of determination (R) of fault-related is 0.18 (Figure 4.21C).
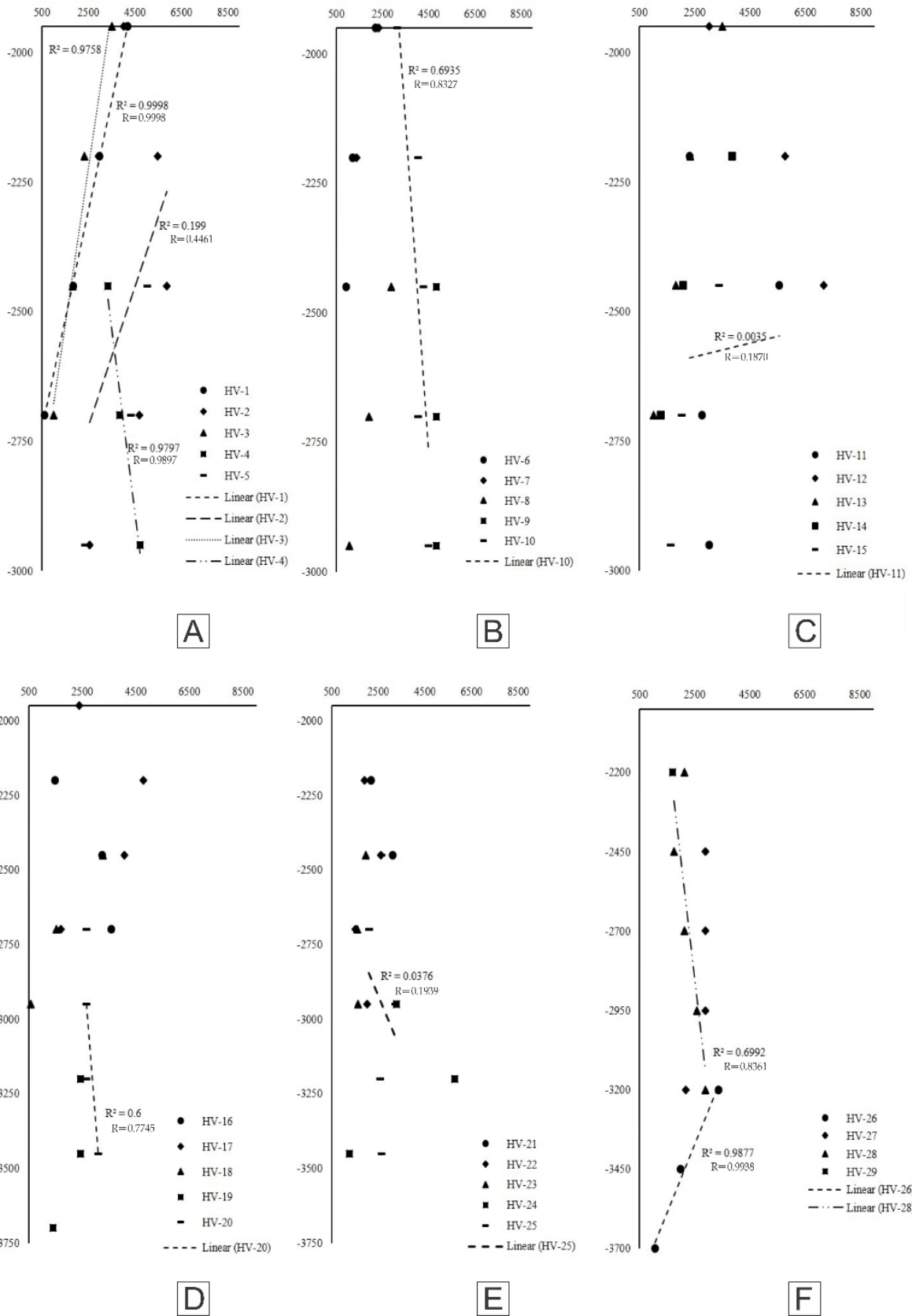
Figure 4.21 – The relationship between depth and the radius of interference (r) of hydrothermal vents in the study area.

4.2.2.2 Characteristics of radial faulting associated with hydrothermal vents

Cross-sectional view of several vents revealed that the carapace morphology of the vents was coupled with several radial and crestal faults. Fault mapping in this study has shown that the radial and crestal faults related to the vents are generally common after the transition from the interval of polygonal faults. In 3-D view, the radial and crestal faults are seen below or adjacent to hydrothermal vents (Figure 4.24). To describe the relationship between the hydrothermal vents and radial and crestal faults, three representative vents have been selected (i.e., V-2, V-3, and V-4). Detailed mapping of the V-2 indicates that the vent has a dome-shaped geometry, down-tampering cone, and vertically restricted to the interval between -1900 to -3200 ms deforming strata of Palaeocene and possibly Early Miocene age.

The radial faults adjacent to V-2 strike generally in ENE-WSW and WNW-WSE directions and gently dipping NW to SSE at angle of 23^0-74^0 (Figure 4.22). Compared to polygonal faults on the flank of V-2, the dip of the radial faults generally increases indicating the rise in throw values at the center of the vent. Three-dimensional seismic mapping has shown that these radial faults transit into polygonal faults within ca. 2.5 km away from the top of the vent. Vent, V-3 has eye-shaped morphology, down-ward tampering, and vertically developed from -2050 to -2700 ms TWTT. The radial faults adjacent to this vent have fault orientation of NW-SE and dip gently southward and north-eastward at angle of 27^0-64^0 (Figure 4.22). In general, there decline in dip of the radial faults is going deeper. At depth below -2700 ms, several minor faults accommodate the deformation near Sill-B (Figure 4.23). These faults strike E-W direction, at dip 27^0-40^0.
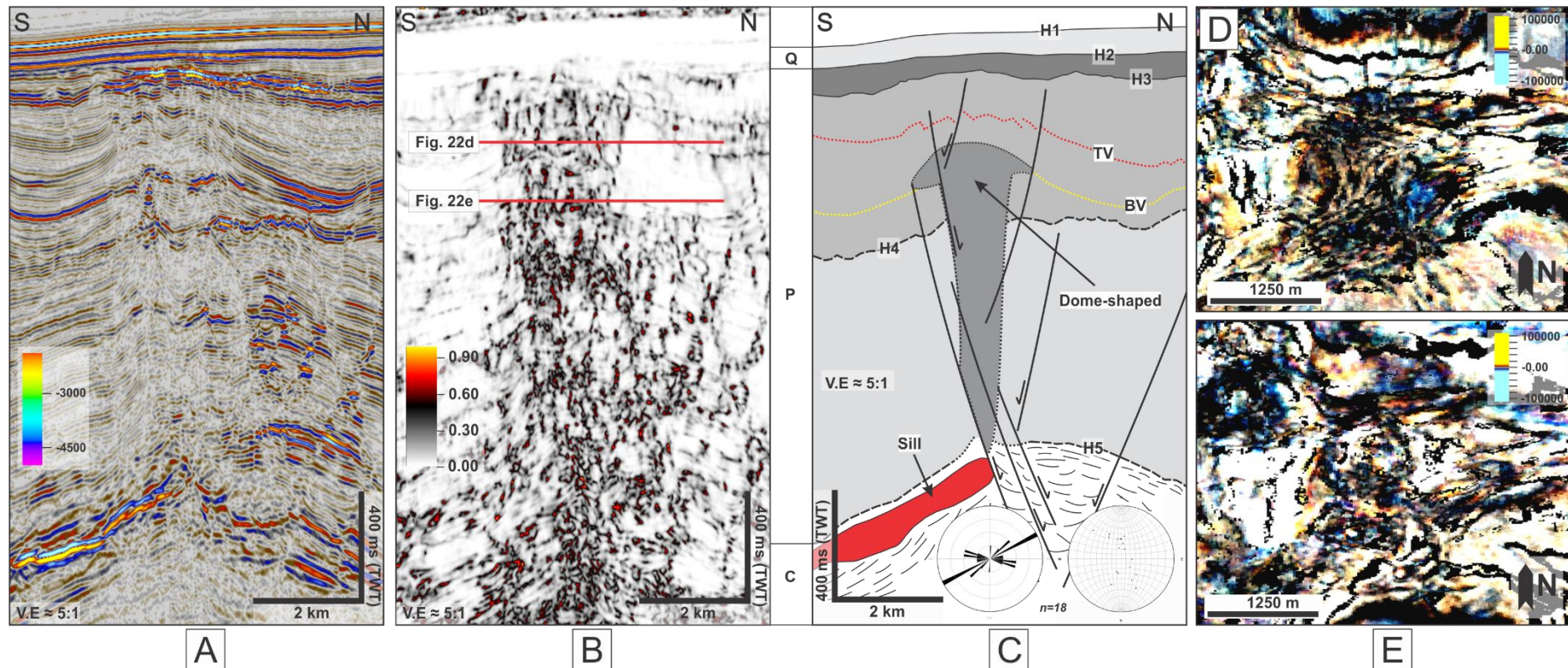
Figure 4.22 – (A) Uninterpreted S-N seismic section. (B) S-N seismic section using chaos attribute. The high amplitudes (red dot) are represent the fluid flow feature. The time slices (red line) are shown in Figure D-E. (C) Interpreted S-N seismic section highlighting the V-2 with dome-shaped and association with the radial faults and magmatic sill. Dash lines indicate the uncertainty in seismic interpretation. *Inset is the rose diagram and the equal area plot*. (D-E) Time slices using spectral decomposition attribute (R=11; G=12; B=13) at -2080 ms TWT (D) and -2280 ms TWT (e) respectively, indicate the bend-up morphology of the V-2.
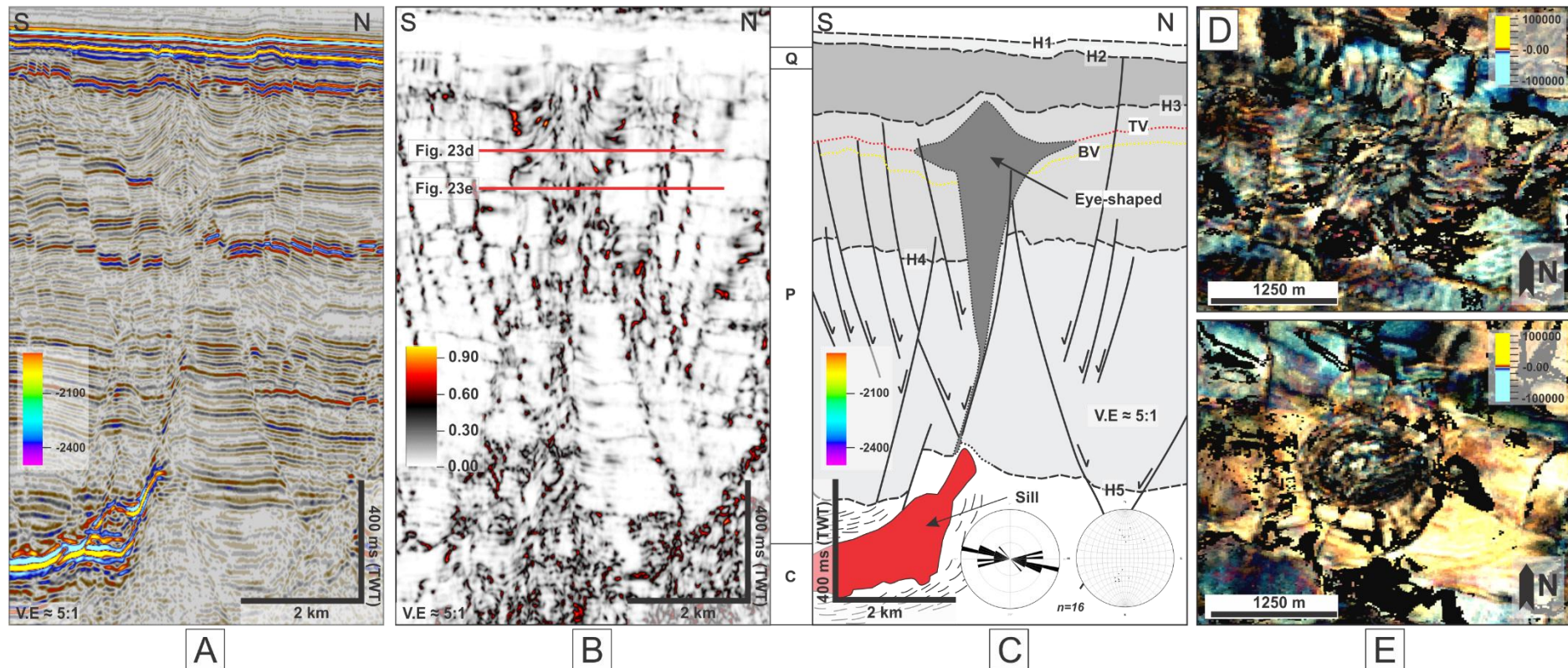
Figure 4.23 – (A) Uninterpreted S-N seismic section. (B) S-N seismic section using chaos attribute. The high amplitudes (red dot) are represented as the fluid flow feature. The time slices (red line) are shown in Figure D-E. (C) Interpreted S-N seismic section highlighting the V-3 with eye-shaped and association with the radial faults and magmatic sill. Dash lines indicate the uncertainty in seismic interpretation. *Inset is the rose diagram and the equal area plot*. (D-E) Time slices of spectral decomposition (R=12; G=13; B=14) at -2100 ms TWT (D) and -2200 ms TWT (E) respectively, indicate the bend-up morphology of the V-3.

Further to the west, V-4 has distinctively different geometry to the other hydrothermal vents. Based on the radius of interference, V-4 exhibits an increase in area and length vertically from -2800 to -3400 ms (Figure 4.21). Omosanya et al. (in press) documented that this vent is pyramid-shaped and associated with several radial faults. The radial faults below the vent dominantly trend in a E-W direction and are consistently dipping southward at 30^0-86^0 (Figure 4.24d). The dip of the radial faults generally increases towards to the central part of the vents, indicating that the faults have increase in throw at the central axis. Some minor faults could be found at depth below -3200 ms with strike E-W and angle of dip of 30^0-34^0. Minor carapace or crestal fault patterns in general occur at the top of V-4 (Figure 4.24B). The formation above the carapace indicates that the strata are in the hanging-wall of a downfaulted graben (Figure 4.24). Below the graben, faults strike E-W, and are inwardly-dipping at 55^0-70^0. These faults are likely concentric fault systems (Figure 4.24 B-C).
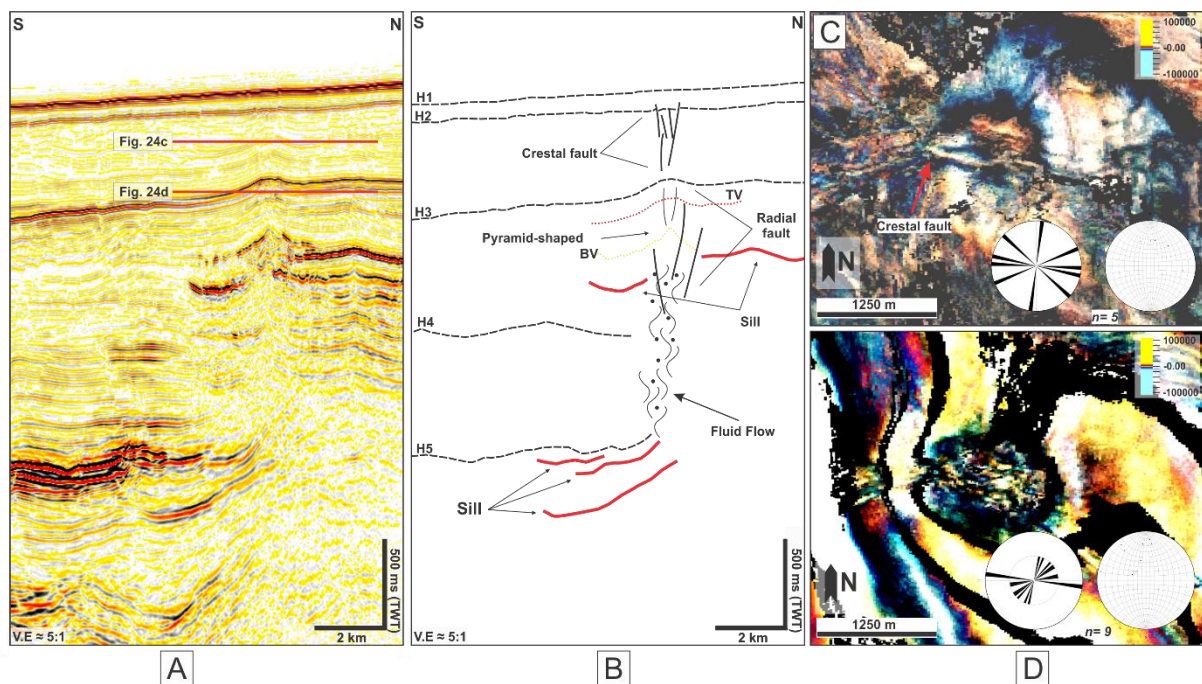
Figure 4.24 – (A-B) Uninterpreted and interpreted S-N seismic section showing pyramid-shaped vents, radial and crestal fault systems, sills, and flow mechanism. (C-D) Time slices using spectral decomposition (R=12; G=13; B=14) showing the transformation from crestal to radial fault as depth increases. The time slices are taken at depth -2100 ms TWT (C) and -2450 ms TWT (D) respectively. *Inset is the rose diagram expressed the fault strikes and the equal angle plot.*

Chapter 5

Discussion and Conclusions

5.1 Reconstructed geological history of the study area

Two major tectonic events affected the mid-Norwegian continental margin during the Late Palaeocene and in the Early Eocene to Oligocene leading to the formation of several Paleogene domes in the Vøring Basin (Brekke, 2000). These tectonic events had changed orientation from NW-SE extension related to the opening of the Norwegian-Greenland Sea to NW-SE compression (Lundin and Doré, 2002; Mjelde et al., 2003; Faleide et al., 2008). The study area, the Naglfar Dome, is interpreted to have been established post-breakup in Early Eocene due to regional inversion of the Hel Graben (Lundin and Doré, 2002). Early Eocene magmatic-induced uplift influenced the configuration of the basin during Paleogene inversion (Omosanya et al., 2017). The Hel Graben on another hand was documented to have been established during continental break-up and opening of the Norwegian and Greenland Seas in Palaeocene. Subsequently, the Hel Graben was heavily rotated and deformed in its north-easternmost section by an Oligocene to Miocene unconformity (Doré et al., 1999).

A conceptual model for the evolution of the Naglfar Dome is presented in Figure 5.1. The geological history of the study area is best preserved by Unit 2, which correlates to the Brygge and Tang Formations. The Tang Formation was deposited during the Late Palaeocene a period coeval with extensional tectonics in the mid-Norwegian continental margin while the Brygge Formation was deposited during the Late Palaeocene to Oligocene during a period of intense magmatic activity and re-organization of regional extensional tectonics to compression. The evidence for compressional events in the study area is shown in Figure 4.4C, where the formations have been constricted into forced folds. Omosanya et al. (2017) documented that the fold appears to form from Early to Mid-Eocene. Furthermore, the breakup system was identified from the multilayer of underlying magmatic sills within the Tang Formation. At least two different periods of magmatic sill emplacement are identified on the mid-Norwegian continental margin i.e., during the Early to Late Palaeocene and Early Eocene (Hansen, 2004; Hansen and Cartwright, 2006a; Hansen and Cartwright, 2006b). It is proved, that based on the occurrence of the underlying magmatic sills, the break-up magmatism during the Early to Late Palaeocene could have led to the formation of several extensional features in the study area.

Furthermore, Berndt et al. (2000) interpreted the presence of these magmatic deposits and indicated that they were probably fed from the Hel Graben. Interpretation of seismic data indicated that the faults may have been established first before the underlying sill propagated from the magma chamber in the study area (Figure 5.1). While the faults below the magmatic sills may be formed after the emplacement of the magmatic sills (Omosanya et al., 2017).
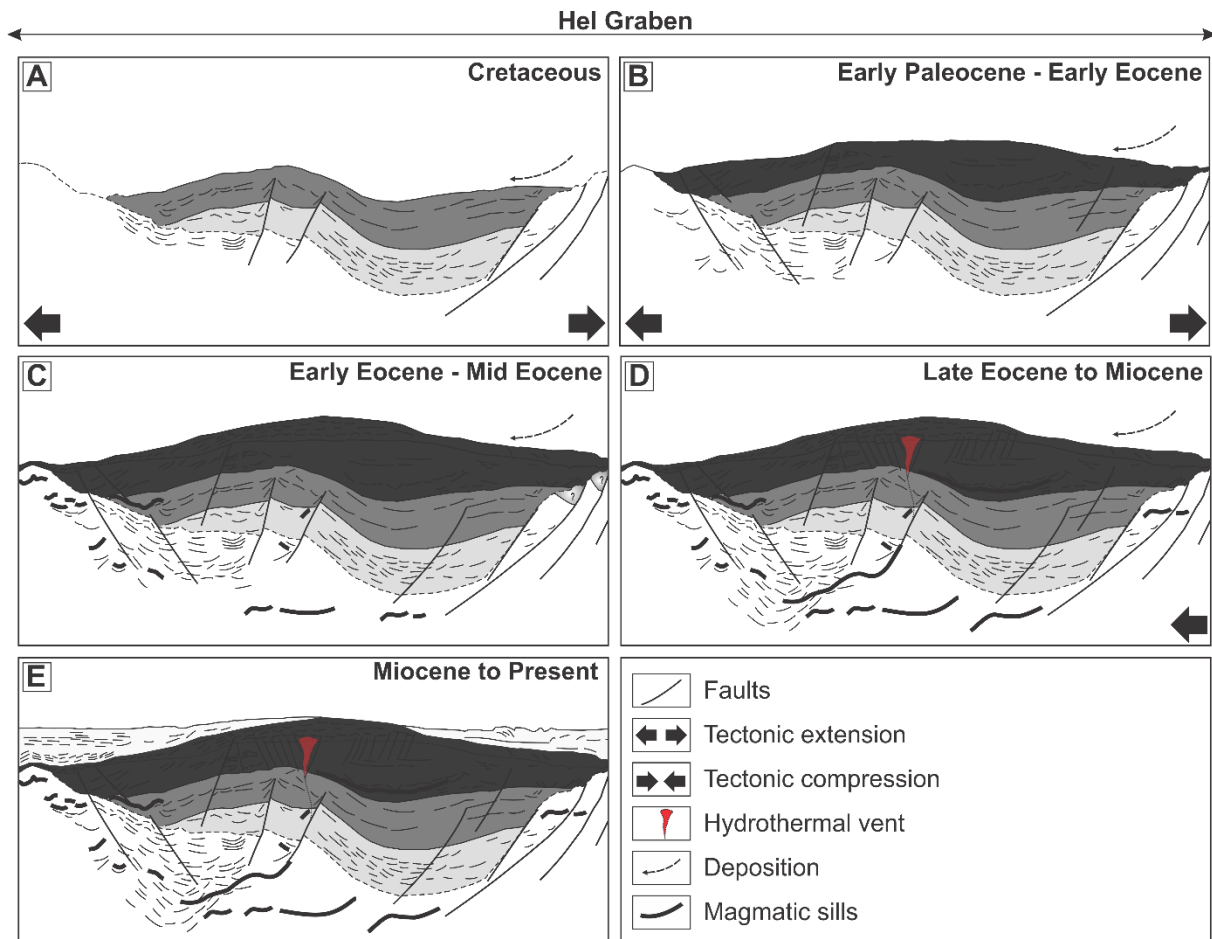
Figure 5.1 – Conceptual model highlighting the evolution of the study area. (A) The Cretaceous formation before the initial deposition of the Palaeogene Formation. (B) Tectonic extensional. (C) Period of tectonic transition from extensional to compression system. Also, the initial emplacement of magmatic intrusion. (D) Continuous magmatic emplacement may have direct affect to formation of hydrothermal vent. (E) The deposition of the Naust Formation that generally un-faulted.

Furthermore, the Kai Formation is Early Miocene to Late Paleocene in age. Interpretation of seismic profile shows that the formation thins to eastern part, and numerous polygonal faults are found in this unit (see Figure 4.6). After the deposition of the Kai Formation, the climate is considered to cool-down, with glaciation period which occurred on the Norwegian margin from 2.8 to 1.5 Ma (Eidvin et al., 2007). The uplift and erosion typically occurred during the Neogene

and was followed by sedimentation of Pliocene-Pleistocene sediments which created the present shelf edge (Blystad et al., 1995; Brekke, 2000). The Naust Formation is considered to be deposited during this period, but relatively in a short time (Eidvin et al., 2007). Consequently, the Naust Formation generally is un-faulted.

5.2 Style of sill emplacement

Multiple emplacement of magmatic sills occurring distinctively at different depths might be consistent with the different magmatic events recorded along the mid-Norwegian continental margin. The different depth of sills succession may indicate different periods of crystallization and emplacement (Annen, 2011). The magmatic migration facilitated by sill is considered to take a longer time rather than dike emplacement (Magee et al., 2016). The longer emplacement may have direct impact on the composition of the igneous rock. Hence, the identification of three main depth of occurrence of sills in the study area is correlated to the three main episodes of magma emplacement in the study area. The intruded magma pulse in contact with host rock may represent mechanical discontinuity, whether fully or partially crystallized intrusion (Annen, 2011) (Figure 5.2A). The merging of intrusive sills due to repeated magma invasion along the host rock would affect the thermal and chemical regeneration (Annen, 2011). Different periods of intrusive pulse may lead to initial magmatic intrusion to cool and crystallize. Consequently, the new magmatic pulse probably will intrude into the low-temperature medium which increases the thickness of initial sills, generally establishing the laccoliths (Annen, 2011; Magee et al., 2016). Hence, if short emplacement occurred, the magma may preserve the temperature to remain hotter in the period of time, allowing intrusion ascendance to the overlying layer (Annen, 2011; Magee et al., 2016). The other scenario indicates that channelization of intrusive magma may increase the segment thickness, by allowing magma flow to be perpetual when other sills solidify (Holness and Humphreys, 2003; Magee et al., 2016) (Figure 5.2B). If the conduit segment is half molten, the new batch magma pulse may be reactive to the conduits (Currier and Marsh, 2015; Magee et al., 2016).

The total area coverage of magmatic sills in the study area is estimated to be more than 8.22 x 10^8 m^2. To a large extent, the sill volume is difficult to estimate because of the limitation of seismic in the estimation of their thickness and correlation of the sills in situations where they intersect former igneous bodies. However, the area extent of the sills shows that magmatic sills can be emplaced further laterally in sedimentary basins for several kilometers against vertical

migration of sills. By mapping flow indicators within sill complexes, the interconnected networks of the sills and inclined sheets generally facilitated magma transport over distances as much as 12 km vertically and 4100 km laterally. Hence, this study further debunks the traditional perspective that volcanoes are fed via dikes and directly over the melt source and shallow-level reservoirs. The lateral extent of the sills from this study supports the idea that sills, upon entering a sedimentary basin, can form laterally extensive sills complexes that may feed volcanoes that are laterally offset from the melt source.
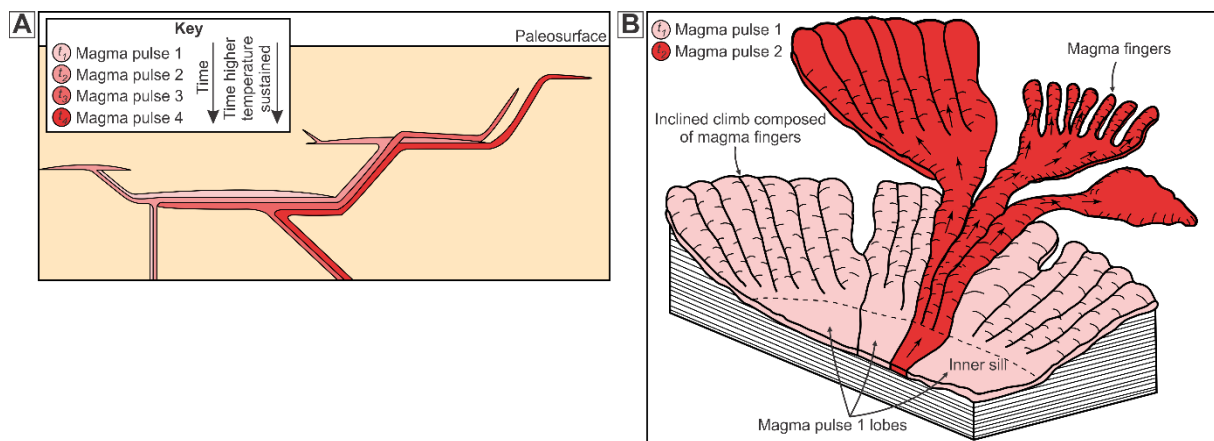
Figure 5.2 – (A) An illustration of magmatic pulse emplacement (Annen, 2011). (B) A finger shaped diagram proposed by Magee et al. (2016).

As for the processes or styles of magmatic sill emplacement in the study area, the presence of intrusive steps within the magmatic sills shows that sill emplacement is favorably related to brittle processes. The intrusive steps are parallel to the axis of magmatic sill emplacement and could be used as a flow indicators (Pollard et al., 1975; Thomson et al., 2008; Schofield et al., 2012; Omosanya et al., 2017). Furthermore, the occurrence of inclined sheets also signifies a brittle process. Although the process leading to the formation of inclined sheets remains ambiguous, magma ascent along inclined sheets in sill complexes is likely facilitated by multiple processes. Most authors favor that the majority of inclined sheets occur in extension fractures proposing that inclined sheets formation is facilitated through: (a) the generation of tensile strains and fractures at the tips of sills in response to overburden bending (Malthe-Sorensson et al., 2004) (Jackson and Pollard, 1990; Galland and Scheibert, 2013); (b) the emplacement of magma along reverse faults that nucleated during the growth of flat-topped forced folds (Thomson et al., 2008); (c) intrusion along pre-existing faults (Magee et al., 2013c); (d) the intrusion of magma along inclined unconformity surfaces (Magee et al., 2016), or (e) the upward deflection, along a curved trajectory, of a propagating fracture beyond the lateral

tip of a sill in response to the asymmetrical emplacement of magma above the initial level of the extension fracture (Hansen, 2015). Hence, it is suggested that sill emplacement in the study area is characterized by brittle deformation. A good example is shown by Sill-A (Figure 4.13), which typically intruded the basement formation and the inclined sheet transgressed upward for ca. 600 ms (Figure 4.13A-B) feeding the magma into overlying formations.

5.3 Development of hydrothermal vents in the study area

Seismic interpretation shows that there is a strong connection between the spatial location of magmatic sills and hydrothermal vent complexes in the study area. In addition, the presence of hydrothermal vents is markedly reflected on seismic sections owing to their amplitude character and their circular to conical morphology in plan view or maps. Planke et al. (2005) documented that the geometry of the upper part of hydrothermal vents is influenced by a combination of structural and compaction process. For instance, the dome structure at the upper parts of vents is interpreted as mud volcanoes on the paleo seafloor while crater structures probably reflect compaction process due to compaction of peripheral formation rather than volcanic eruption. The timing of hydrothermal vent development postdates the emplacement of the underlying sills. Younger sills emplaced lately are typically found at shallow depth and likely responsible for the re-structuring the pre-existing hydrothermal vents (e.g. crater-shaped vents) (Omosanya et al., in press).

Undoubtedly, the vents have strong connection with the underlying sills at different depths. A model from V-3 (Figure 4.23c) has proven that, in general, the hydrothermal vents typically coincide with the tips of the underlying sills, are adjacent to polygonal, and have atop them radial and crestal faults. Shortly after the emplacement of the molten magma, vertical stress would increase due to magma pressure, generation of boiling fluid, degassing, and fracturing the overburden (Planke et al., 2005; Judd and Hovland, 2009; Omosanya et al., 2017). Increase of local fluid pressure which is higher than the hydrostatic pressure, may lead to the creation of hydrothermal vents (Jamtveit et al., 2004). Here, mobilization of fluid through overburden and increase hydrostatic pressure led to reorganization of stress state within the polygonal faults, allowing the establishment of radial faults.
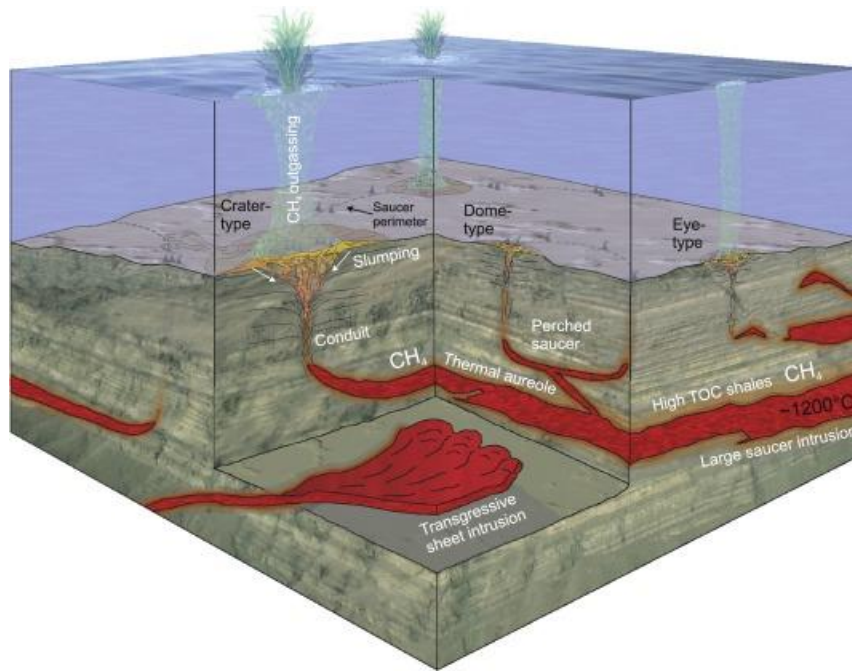
Figure 5.3 – Illustration of the relationship between hydrothermal vents and underlying sill intrusions (Adapted from Reynolds et al. (2017)).

Resolving the type of materials filling the vents in general is challenging. The study by Jamtveit (1987) in the Karoo Basin indicated the vents are comprised of brecciated sediments, while the investigation of Svensen et al. (2003) in the Vøring Basin showed that the vents contain seep carbonate anomalies. Considering the seismic character (chaos attribute) of the vents from the study area, limited amplitude contrast exists between the vent and the host-rock strata. It is therefore proposed that the vents in the study area are filled with rocks similar in composition to the host-rock strata and are likely brecciated sediments rather than magmatic materials due to the complex and chaotic mixture of different seismic amplitudes (e.g., Figure 4.22b, Figure 4.23b).

5.4 Fault growth and as conduits during magmatic sill emplacement

Faults are potentially well-developed from the Unit 1 and limited until Unit 2, suggesting the major growth of the faults was probably active from Late Palaeocene until Miocene. In addition, the geometry of the fault planes indicates that the faults generally developed prior to sill emplacement. The pervasive magma within the primitive structures is considered to have occurred in two ways: if the lateral principal stresses are less than the magmatic driving pressure, and if the structures are almost perpendicular to the orientation of least compressive regional stress (Delaney et al., 1986). However, if the primitive structures are absent, the

magma invasion must fill the 'new structures' (Delaney et al., 1986). During the invasion of magmatic intrusion, the driving pressure has to be higher than the vertical overburden stress which corresponds to the stress minima $\sigma 3$ (Magee et al., 2013b). These components, therefore, have a large effect on the sill geometry (Magee et al., 2013b). The coalescence of vertically offset magma segments generally is related to the establishment of the intrusive steps and does not relate to the faults (Schofield et al., 2012). The interpretation from intrusive steps within the Sill-A indicates that the magma flow generally mobilized outward, radially from the center. The intrusive step of Sill-A ranges from 23.6-165 m and is showing parallel to the fault. At fault F60, the inclined segment of the sill ends up parallel to the fault and reaches ~600 ms. Undoubtedly, this indicates that the sill emplacement is unlikely at the same time as fault displacement. It is plausible to say that the propagation sill uses the faults to reorient the flow by following the strike of the fault. In addition, the adjacent lithologies are also considered to juxtapose along the fault plane and the intrusion.

A second sill, the Sill-B (Figure 5.4), is probably formed in response to fault stress associated with magmatic-driven pressure failure in the formation, leading to horizontal propagation of the magmatic sill that is sub-parallel with σ_1-σ_2 (Walker, 2016). Lateral propagation may be associated with stress asymmetry that occurs due to length of the horizontal segments that is more than two to three times of the overburden thickness. The intrusive steps range from 24-54 m, but do not have inclined-sheets (i.e., Sill-A). The offset of Sill-B generally decreases to the northeast, with the fault throw to be less than 6 m. This process may be related to bulk grain of the adjacent formation (Dewhurst et al., 1999). This indicates that the propagation of the sill typically occurred after the displacement of the faults. The sill is considered to exploit the fault by reorienting the flow to be parallel with the fault. Therefore, the interaction style between magma and faults is primarily controlled by the fault-plane geometry and orientation (Valentine and Krogh, 2006; Bédard et al., 2012).

Beyond the tip of the intrusive, the contact with the host rock may create pressure that generates tensile stress that is sufficient to create structures in the host-rock unit (Delaney et al., 1986). While peripheral to the intrusive, the pressure is sufficient enough to generate tensile maxima (Delaney et al., 1986). Finally, the emplacement of magmatic intrusive may also perturb the fluid within the overburden to become over-pressured and initiates the formation of hydrothermal vents (Jamtveit et al., 2004; Hansen and Cartwright, 2006a). Mobilization of fluid through the overburden, increases the hydrostatic pressure, reorganizes the stress state within

the polygonal, and then creates the radial faults (e.g., Figure 5.4B). Through time, reduction in magmatic pulse parallel to pressure reduction within the fault conduit can cause the conduit to be closed (Bédard et al., 2012).
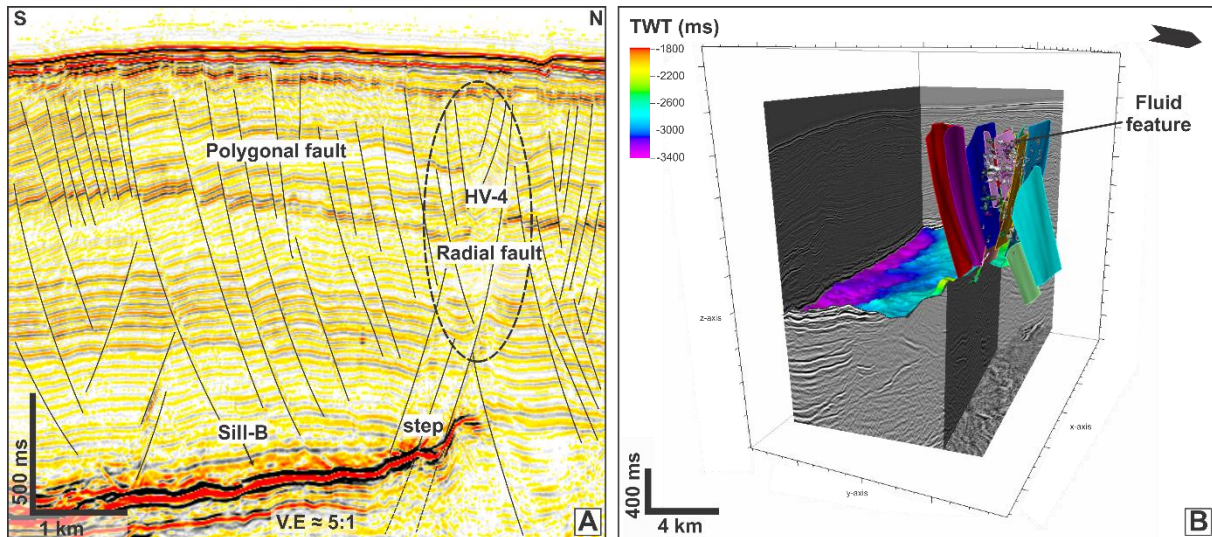
Figure 5.4 – (A) Interpreted S-N seismic section showing the polygonal and radial fault systems, sills, intrusive steps, and V-3. (B) A 3-D illustration of fluid feature within the fault plane, and its relationship with the emplacement of the Sill-B.

Adjacent to the fault plane corrugation, near-fault stress field perturbation may redirect σ_3 to be perpendicular to the fault plane (Chester and Chester, 2000; Magee et al., 2016). The direction of the maximum compressive stress within brittle failure generally ranges from 20°-40° (Chester and Chester, 2000). Being very close to the fault plane, the maximum compressive stress indicates as high angle to the fault, known as the far field (Chester and Chester, 2000). Therefore, it is plausible that σ_3 is locally reoriented by the near fault stress field to plunge in Sill-A at about 39° and in Sill-B at 40°. This supports the analysis that the sill may redirect the flow to become parallel to the fault rather than create a continuous bedding parallel intrusion (Magee et al., 2016). In particular, sills may only intrude up to the faults when faults are hosted in the hanging wall and flow towards or across the strike of the fault plane; i.e., uplift of the overburden reduces the normal stress across the fault, allowing magma to intrude.

5.5 Mechanism for development of radial and crestal faults

Most of the hydrothermal vents in this study area are placed adjacent or directly above the radial faults, whereas some local crestal faults may form above the vent complexes. The dynamic process of upward fluid migration through the overburden may have initiated the development

of these complex fault systems. From maps and time slices, it is obvious that the radial faults are overprinted within the polygonal fault systems (Figure 4.16). As the polygonal faults close up to the boundary of the radial faults, their dips typically increase, suggesting that both fault types are formed at different time. In the special case study of salt-diapirs, Carruthers et al. (2013) documented that within a basin dominated by polygonal fault patterns, radial faults are developed as perturbed systems that occurred as the effect of compression and extension in anisotropic stress conditions. Carruthers et al. (2013) used regional stress analysis to understand the evolution of radial faults associated with salt diapirs in the Espírito Santo Basin, Brazil (Figure 5.5).
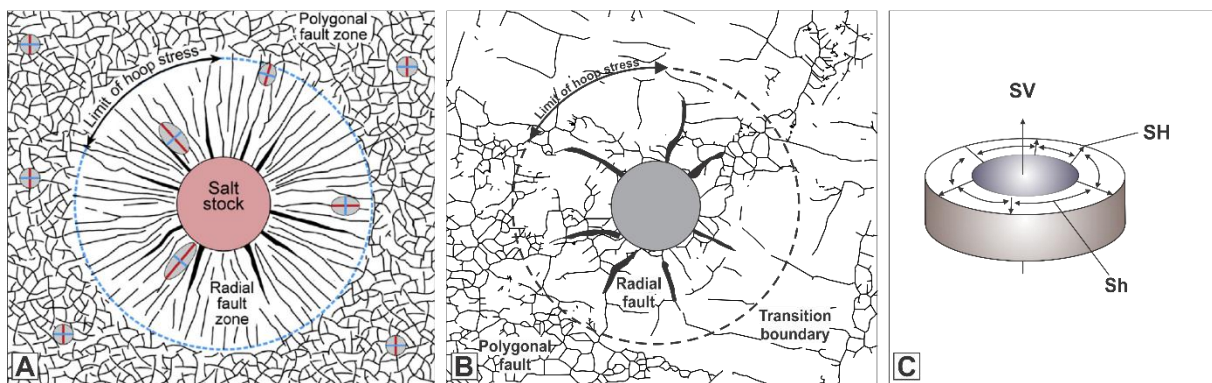
Figure 5.5 – (A) Illustration of polygonal faults around salt-diapirs (Carruthers et al., 2013) (B) Interpretation of fault systems peripheral to hydrothermal vent V-3. (C) Mechanical analogy using pressurized borehole (From Brown (1977)) for principal stress analysis. *SH* (radial compression), *Sh* (hoop extension), *Sv* (vertical stress).

Radial faults associated with hydrothermal vents e.g., V3 (Figure 5.4A-B) are analogous to radial fault systems developed within polygonal systems in salt-rich basins such as those of Carruthers et al., 2013. In such settings, the vertical stress (*Sv*) is associated with the weight of overburden, while the horizontal stress (*Sh*) is a ratio of the vertical stress (Figure 5.5C). Their analysis shows that the radial compression to the salt diapirs typically decreases with increasing hoop extension and distance until the hoop extension reaches the same magnitude and differential stress is zero (Carruthers et al., 2013). The maximum stress applied to hydrothermal vents is typically vertical, the same as in salt-diapirs, where the radial compression and hoop extension around the vents have less principal stress (Carruthers et al., 2013).

5.6 Implication for hydrocarbon and mineral exploration in the study area

Well 6706/-1 is an exploration well with a gas discovery (NPD, 2017). Higher gas readings are recorded at depths of 2340 to 2360 m (maximum 6%), 3013 to 3020 m (maximum 6%), 3260 to 3280 (maximum 8%), and 3360 to 3450 m (maximum 2.5%) from four intervals (NPD, 2015). Further geochemical analysis also indicated that the shaley layers in the study area contain good TOC (with average TOC value of 1.4 wt %), but have low potential for hydrocarbon generation (NPD, 2015). The thermal maturity is %Ro = 0.5, indicating the beginning of oil window at depth of 2680 m. This maturity is typically shallow considering that the water depth is 1298 m (NPD, 2015). Thermal heat produced by the magmatic sills may have an impact on maturation and migration of hydrocarbon in the study area (Holford et al., 2012; Magee et al., 2013c). Four scenarios have been proposed to describe the likely impact of intrusive rocks on compartmentalization of reservoir and petroleum systems in sedimentary basins (Holford et al., 2012; Magee et al., 2013c).
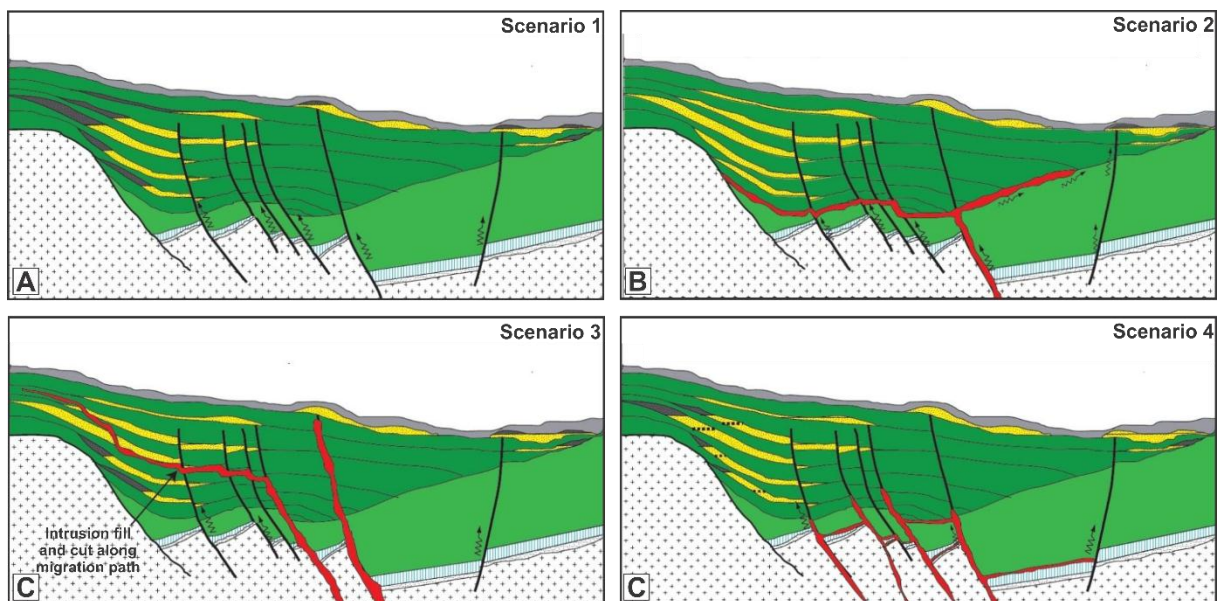
Figure 5.6 – Illustrations of intrusive magma compartmentalization (Holford et al., 2012; Magee et al., 2013c).

In the first scenario, there is no magmatic emplacement (Figure 5.6A). In the second scenario, the magma starts to propagate through the magma chamber using the fault complexes as a pathway, creating intrusive steps, and following the truncations (Figure 5.6B). Successive magma may occupy the lower part of the basin acting as barriers to hydrocarbon migration and may form shadow zones in the upper part of the magmatic intrusion where traps are not filled (Magee et al., 2013a). The propagating magma may compartmentalize the upper stratigraphic

layer. Successive magma may create dikes or inclined-sheets in the upper part (Figure 5.6C). The next scenario (Figure 5.6D) is when intrusion may compartmentalize the source rock, becoming barriers for vertical and horizontal migration, and likely reducing the volume of hydrocarbon (Magee et al., 2013a).
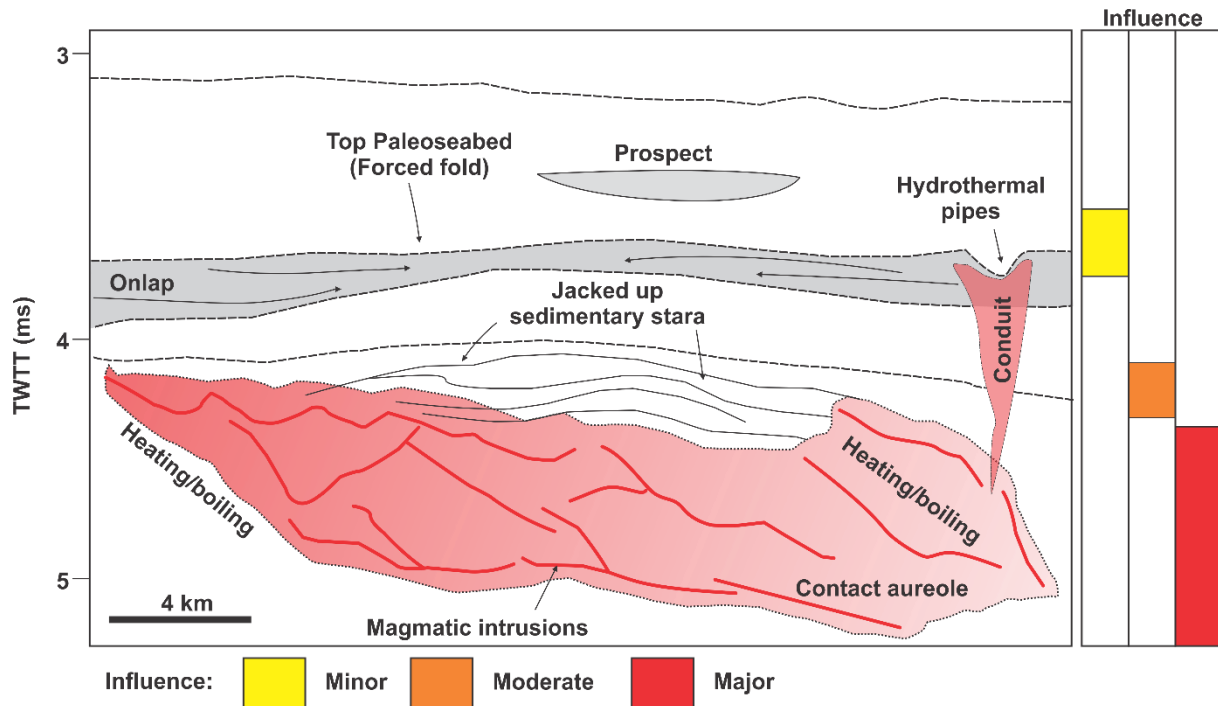
Figure 5.7 – Schematic diagram highlighting the consequences of sill emplacement on reservoir compartmentalization and source rock quality (After Omosanya et al. (2017)).

The presence of hydrothermal vents may also create pathway for over-pressured gases or fluids to propagate vertically (Svensen et al., 2006). An alternative influence of magmatic emplacement on reservoir compartmentalization and source rock quality in the study area is discussed by Omosanya et al. (2017). There are three scenarios: (a) Several hundred meters above the underlying intrusions, in which the effect on reservoir compartmentalization and quality is generally minor; (b) If the reservoir is situated at the upper part of the intrusion, the sill emplacement will have moderate influence on the reservoir; (c) However, if the intrusion invades the reservoir, the influence is major (Figure 5.7).

Additionally, intrusive emplacement through the fault planes may isolate the pathway for fluids to migrate and reduce the host rock permeability due to metamorphism. Isolated compartments of sediment sealed by the low permeability intrusive may have impact on the efficiency of hydrocarbon mobilization out of source rocks and into the reservoirs (Holford et al., 2013). Compared to a conventional non-volcanic basin, the intrusive magma genetically produce their own seal properties (e.g., tuffs, tight basalt flow) and reservoirs (e.g., hyaloclastites, fractures

volcanic), allowing a new reservoir-seal (Rohrman, 2007). However, fractures produced by intrusive magma due to thermal cooling after the emplacement or during brittle tectonic deformation can lead to the formation of secondary porosity and permeability, and therefore act as a conduit for mobilization of fluid through impermeable barriers (Holford et al., 2013; Rateau et al., 2013). This process may be significant for the migration of fluids from which mineral can be precipitated. Corseri et al. (2017) modelled the presence of pyrrhotite deposits in sediments intruded by magmatic sills in the North Gjallar Ridge, Vøring Basin, based on modelling and integration of magnetotelluric (MT) survey, Bouger anomaly, magnetic field, and seismic reflection. The mineral deposit was modelled to extend to the pre-Cretaceous sequences and probably until the upper continental crust.

5.7 Conclusions

Based on three-dimensional (3-D) seismic interpretation, this thesis has described a suite of magmatic intrusions, hydrothermal vents, and showed the strong affinity between sills and fault planes. The study area was affected by NE-SW extension stresses during the Late Palaeocene, which changed to NW-SE directed compression during the Early Eocene to Oligocene. The tectonic evolution of the study area, the Naglfar Dome, is related to post-breakup events i.e. regional inversion during the Early Eocene. Magmatic emplacement in the study area occurred in two phases i.e., during Early to Late Palaeocene and in the Early Eocene. These periods presumably explain the different depth of occurrence of magmatic sills in the study area, where deeper sills typically cover large areas than the shallow sills.

The presence of intrusive steps and inclined sheets sills signifies that the magmatic style is dominated by brittle processes. Interpreted intrusive steps also generally show the presence of en-echelon and step-stair shapes. Based on this analysis, it is concluded that the emplacement of the magmatic sills is unrelated to or not established at the same time with the fault systems. It is more likely that the polygonal faults are formed first, followed by the magmatic sills. The fault throws and displacements also favor this condition such that the faults typically become a conduit rather than deform the sills. The host rock and the faults favor the formation of transgressive saucer-shaped sills. Some magmatic sills are shallowly dipping or layer-parallel due to horizontal propagation of magmatic sills being sub-parallel with σ_1-σ_2.

After magmatic emplacement, the hydrothermal vents were formed. The rise of vertical fluid facilitated the formation of hydrothermal vents with the maximum stress applied in vertical orientation. As the result of fluid migration and increased hydrostatic stress, that are directly linked to the vent, the reorganization of the stress within polygonal faults triggers the formation of radial faults. Mapped vents show dome-, eye-, and crater-shaped upper parts. The eye-shaped vents are most dominant in the study area. Furthermore, the minimum and maximum diameter of radius of interference of the hydrothermal vents typically is 1.9 to 5.7 km. The dome structure at the upper parts of some of the vents is interpreted to have formed at the paleo seafloor, while the crater structure may relate to compaction process. The emplacement of shallow sills, to some extent, may destroy the geometry of earlier formed vents.

5.8 Recommendations

Further detailed study on palaeostress conditions is important to further understand the interaction between magmatic sill emplacement and faults. By doing this, the stress conditions surrounding magmatic sills and hydrothermal vents can be understood. Perhaps, due to the different geological settings and deformation, the fault stress field associated with the formation of radial and crestal faults in magma-rich basins may be different from those in salt-rich settings.

References

Alvarenga, R. S.,Iacopini, D.,Kuchle, J.,Scherer, C. M. S. & Goldberg, K. 2016. Seismic characteristics and distribution of hydrothermal vent complexes in the Cretaceous offshore rift section of the Campos Basin, offshore Brazil. *Marine and Petroleum Geology,* 74**,** 12-25.

Annen, C. 2011. Implications of incremental emplacement of magma bodies for magma differentiation, thermal aureole dimensions and plutonism–volcanism relationships. *Tectonophysics,* 500**,** 3-10.

Barnett, J. A.,Mortimer, J.,Rippon, J. H.,Walsh, J. J. & Watterson, J. 1987. Displacement geometry in the volume containing a single normal fault. *AAPG Bulletin,* 71**,** 925-937.

Bédard, J.,Naslund, H.,Nabelek, P.,Winpenny, A.,Hryciuk, M.,Macdonald, W.,Hayes, B.,Steigerwaldt, K.,Hadlari, T. & Rainbird, R. 2012. Fault-mediated melt ascent in a Neoproterozoic continental flood basalt province, the Franklin sills, Victoria Island, Canada. *Geological Society of America Bulletin,* 124**,** 723-736.

Berndt, C.,Skogly, O. P.,Planke, S.,Eldholm, O. & Mjelde, R. 2000. High-velocity breakup-related sills in the Vøring Basin, off Norway. *Journal of Geophysical Research: Solid Earth,* 105**,** 28443-28454.

Blystad, P.,Brekke, H.,Færseth, R. B.,Larsen, B. T.,Skogseid, J. & Tærudbakken, B. 1995. Structural elements of the Norwegian continental shelf. Part II. The Norwegian Sea Region. *NPD, Norwegian Petroleum Directorate, Bulletin 8.*

Brekke, H. 2000. The tectonic evolution of the Norwegian Sea Continental Margin with emphasis on the Voring and More Basins. *Geological Society, London, Special Publications,* 167**,** 327-378.

Brekke, H.,Dahlgren, S.,Nyland, B. & Magnus, C. 1999. The prospectivity of the Voring and More basins on the Norwegian Sea continental margin. *Petroleum Geology Conference Series,* 14**,** 261-274.

Brown, E. T. 1977. Fundamentals of rock mechanics. *Tectonophysics,* 38**,** 367-368.

Bukovics, C. & Ziegler, P. A. 1985. Tectonic development of the Mid-Norway continental margin. *Marine and Petroleum Geology,* 2**,** 2-22.

Carruthers, D.,Cartwright, J.,Jackson, M. P. & Schutjens, P. 2013. Origin and timing of layer-bound radial faulting around North Sea salt stocks: New insights into the evolving stress state around rising diapirs. *Marine and Petroleum Geology,* 48**,** 130-148.

Carruthers, T. 2012. *Interaction of polygonal fault systems with salt diapirs.* Cardiff University.

Cartwright, J. & Hansen, D. M. 2006. Magma transport through the crust via interconnected sill complexes. *Geology,* 34**,** 929-932.

Cartwright, J.,James, D. & Bolton, A. 2003. The genesis of polygonal fault systems: a review. *Geological Society, London, Special Publications,* 216**,** 223-243.

Cartwright, J. & Mansfield, C. 1998. Lateral displacement variation and lateral tip geometry of normal faults in the Canyonlands National Park, Utah. *Journal of Structural Geology,* 20**,** 3-19.

Chester, F. M. & Chester, J. S. 2000. Stress and deformation along wavy frictional faults. *Journal of Geophysical Research: Solid Earth,* 105**,** 23421-23430.

Chudi, O. K. 2015. *Predicting Oligocene reservoir potential in the deep-water Western Niger Delta: an integrated basic modelling and diagenetic study.* Heriot-Watt University.

Corseri, R.,Senger, K.,Selway, K.,Abdelmalak, M. M.,Planke, S. & Jerram, D. A. 2017. Magnetotelluric evidence for massive sulphide mineralization in intruded sediments of the outer Vøring Basin, mid-Norway. *Tectonophysics,* 706**,** 196-205.

Currier, R. M. & Marsh, B. D. 2015. Mapping real time growth of experimental laccoliths: The effect of solidification on the mechanics of magmatic intrusion. *Journal of Volcanology and Geothermal Research,* 302**,** 211-224.

Dalland, A.,Worsley, D. & Ofstad, K. 1988. A lithostratigraphic scheme for the Mesozoic and Cenozoic succession offshore mid- and northern Norway. *Norwegian Petroleum Directorate Bulletin.*

Davies, R. D.,Bell, B. R.,Cartwright, J. A. & Shoulders, S. 2002. Three-dimensional seismic imaging of Palaeogene dike-fed submarine volcanoes from the northeast Atlantic margin. *Geology,* 30**,** 223-226.

Delaney, P. T.,Pollard, D. D.,Ziony, J. I. & Mckee, E. H. 1986. Field relations between dikes and joints: emplacement processes and paleostress analysis. *Journal of Geophysical Research: Solid Earth,* 91**,** 4920-4938.

Dewhurst, D. N.,Cartwright, J. A. & Lonergan, L. 1999. The development of polygonal fault systems by syneresis of colloidal sediments. *Marine and Petroleum Geology,* 16**,** 793-810.

Doré, A.,Lundin, E.,Jensen, L.,Birkeland, Ø.,Eliassen, P. & Fichler, C. Principal tectonic events in the evolution of the northwest European Atlantic margin. Geological society, london, petroleum geology conference series, 1999. Geological Society of London, 41-61.

Doré, A.,Lundin, E.,Kusznir, N. & Pascal, C. 2008. Potential mechanisms for the genesis of Cenozoic domal structures on the NE Atlantic margin: pros, cons and some new ideas. *Geological Society, London, Special Publications,* 306**,** 1-26.

Duff, P. M. D. & Duff, D. 1993. *Holmes' principles of physical geology*, Taylor & Francis.

Eidvin, T.,Brekke, H.,Riis, F. & Renshaw, D. K. 1998. Cenozoic stratigraphy of the Norwegian Sea continental shelf 64degreesN-68degreesN. *Norsk Geologisk Tidskrift,* 78**,** 125-151.

Eidvin, T.,Bugge, T. & Smelror, M. 2007. The Molo Formation, deposited by coastal progradation on the inner Mid-Norwegion continental shelf, coeval with the Kai Formation to the west and the Utsira Formation in the North Sea. *Norsk Geologisk Tidsskrift,* 87**,** 75.

Eldholm, O. 1991. Magmatic tectonic evolution of a volcanic rifted margin. *Marine Geology,* 102**,** 43-61.

Eldholm, O. & Grue, K. 1994. North Atlantic volcanic margins : Dimensions and production rates a volume of flood basalts a mean eruption rate of the basalts were emplaced within volume in a mean crustal accretion rate. *Journal of Geophysical Research,* 99**,** 2955-2968.

Eldholm, O.,Thiede, J. & Taylor, E. 1989. Evolution of the Vøring Volcanic Margin. *Proceedings of the Ocean Drilling Program, 104 Scientific Results.*

Faleide, J. I.,Tsikalas, F.,Mjelde, R.,Wilson, J. & Eldholm, O. 2008. Structure and evolution of the continental margin off Norway and the Barents Sea. *Episodes,* 31**,** 82-91.

Frey, Ø.,Planke, S.,Symonds, P. A. & Heeremans, M. 1998. Deep crustal structure and rheology of the Gascoyne volcanic margin, western Australia. *Marine Geophysical Research,* 20**,** 293-311.

Galland, O. & Scheibert, J. 2013. Analytical model of surface uplift above axisymmetric flat-lying magma intrusions: Implications for sill emplacement and geodesy. *Journal of Volcanology and Geothermal Research,* 253**,** 114-130.

Gawthorpe, R. & Leeder, M. 2000. Tectono-sedimentary evolution of active extensional basins. *Basin Research,* 12**,** 195-218.

Gjelberg, J.,Dreyer, T.,Høie, A.,Lilleng, T. & Tjelland, T. 1987. Late Triassic to Mid-Jurassic sandbody development on the Barents and Mid-Norwegian shelf. *Petroleum Geology of North West Europe***,** 1105-1129.

Gridley, J. & Partyka, G. 1997. Processing and interpretational aspects of spectral decomposition. *SEG Technical Program Expanded Abstracts 1997.* Society of Exploration Geophysicists.

Hansen, D. M. 2004. 3D seismic characterisation of igneous sill complexes in sedimentary basins: North-East Atlantic Margin.

Hansen, D. M. & Cartwright, J. 2006a. The morphology of intrusion-related vent structures and their implications for constraining the timing of intrusive events along the NE Atlantic margin. *Journal of the Geological Society,* 163**,** 789-800.

Hansen, D. M. & Cartwright, J. 2006b. The three-dimensional geometry and growth of forced folds above saucer-shaped igneous sills. *Journal of Structural Geology,* 28**,** 1520-1535.

Hansen, D. M.,Cartwright, J. A. & Thomas, D. 2004. 3D Seismic Analysis of the Geometry of Igneous Sills and Sill Junction Relationships. *Geological Society, London, Memoirs,* 29**,** 199-208.

Hansen, J. A.,Bergh, S. G. & Henningsen, T. 2011. Mesozoic rifting and basin evolution on the Lofoten and Vesterålen Margin, North-Norway; time constraints and regional implications. *Norsk Geologisk Tidsskrift,* 91**,** 203-228.

Herron, D. A. 2011. *First steps in seismic interpretation*, Society of Exploration Geophysicists.

Holford, S.,Schofield, N.,Jackson, C.,Magee, C.,Green, P. & Duddy, I. Impacts of igneous intrusions on source and reservoir potential in prospective sedimentary basins along the Western Australian continental margin. West Australian Basins Symposium. Proceedings of the Petroleum Exploration Society of Australia Symposium, Perth, WA, 2013. 1-12.

Holford, S.,Schofield, N.,Macdonald, J.,Duddy, I. & Green, P. 2012. Seismic analysis of igneous systems in sedimentary basins and their impacts on hydrocarbon prospectivity: Examples from the southern Australian margin. *The APPEA Journal,* 52**,** 229-252.

Holness, M. & Humphreys, M. 2003. The Traigh Bhan na Sgurra Sill, Isle of Mull: flow localization in a major magma conduit. *Journal of Petrology,* 44**,** 1961-1976.

Hongxing, G. & Anderson, J. K. 2007. Fault throw profile and kinematics of Normal fault: conceptual models and geologic examples. *Geol. J. China Univ,* 13**,** e88.

Jackson, C. a.-L. & Rotevatn, A. 2013. 3D seismic analysis of the structure and evolution of a salt-influenced normal fault zone: a test of competing fault growth models. *Journal of Structural Geology,* 54**,** 215-234.

Jackson, C. A.,Schofield, N. & Golenkov, B. 2013. Geometry and controls on the development of igneous sill–related forced folds: A 2-D seismic reflection case study from offshore southern Australia. *Geological Society of America Bulletin,* 125**,** 1874-1890.

Jackson, M. D. & Pollard, D. D. 1990. Flexure and faulting of sedimentary host rocks during growth of igneous domes, Henry Mountains, Utah. *Journal of Structural Geology,* 12**,** 185-206.

Jamtveit, B. 1987. Metamorphic evolution of the Eiksunddal eclogite complex. Western Norway, and some tectonic implications. *Contributions to Mineralogy and Petrology,* 95**,** 82-99.

Jamtveit, B.,Svensen, H.,Podladchikov, Y. Y. & Planke, S. 2004. Hydrothermal vent complexes associated with sill intrusions in sedimentary basins. *Geological Society, London, Special Publications,* 234**,** 233-241.

Joppen, M. & White, R. S. 1990. The structure and subsidence of Rockall Trough from two-ship seismic experiments. *Journal of Geophysical Research,* 95**,** 19821.

Judd, A. & Hovland, M. 2009. *Seabed fluid flow: the impact on geology, biology and the marine environment*, Cambridge University Press.

Kamal'deen, O. O. & Alves, T. M. 2014. Mass-transport deposits controlling fault propagation, reactivation and structural decoupling on continental margins (Espírito Santo Basin, SE Brazil). *Tectonophysics,* 628**,** 158-171.

Kim, Y.-S. & Sanderson, D. J. 2005. The relationship between displacement and length of faults: a review. *Earth-Science Reviews,* 68**,** 317-334.

Kittilsen, J.,Olsen, R. R.,Marten, R. F.,Hansen, E. K. & Hollingsworth, R. R. 1999. The first deepwater well in Norway and its implications for the Upper Cretaceous Play, Voring basin. *Petroleum Geology of Northwest Europe: Proceedings of the 5th Conference on the Petroleum Geology of Northwest Europe,* 1**,** 275-280.

Kjoberg, S.,Schmiedel, T.,Planke, S.,Svensen, H. H.,Millett, J. M.,Jerram, D. A.,Galland, O.,Lecomte, I.,Schofield, N. & Haug, Ø. T. 2017. 3D structure and formation of hydrothermal vent complexes at the Paleocene-Eocene transition, the Møre Basin, mid-Norwegian margin. *Interpretation,* 5**,** SK65-SK81.

Lundin, E. & Doré, A. 2002. Mid-Cenozoic post-breakup deformation in the 'passive'margins bordering the Norwegian–Greenland Sea. *Marine and Petroleum Geology,* 19**,** 79-93.

Lundin, E. R.,Dore, A. G.,Ronning, K. & Kyrkjebo, R. 2013. Repeated inversion and collapse in the Late Cretaceous-Cenozoic northern Voring Basin, offshore Norway. *Petroleum Geoscience,* 19**,** 329-341.

Magee, C.,Hunt-Stewart, E. & Jackson, C. a. L. 2013a. Volcano growth mechanisms and the role of sub-volcanic intrusions: Insights from 2D seismic reflection data. *Earth and Planetary Science Letters,* 373**,** 41-53.

Magee, C.,Jackson, C. a.-L. & Schofield, N. 2013b. The influence of normal fault geometry on igneous sill emplacement and morphology. *Geology,* 41**,** 407-410.

Magee, C.,Jackson, C. a. L. & Schofield, N. 2013c. Interaction between Faults and Igneous Intrusions in Sedimentary Basins: Insights from 3D Seismic Reflection Data*. *AAPG International Conference and Exhibition.* Singapore: AAPG©2012.

Magee, C.,Maharaj, S. M.,Wrona, T. & Jackson, C. a.-L. 2015. Controls on the expression of igneous intrusions in seismic reflection data. *Geosphere,* 11**,** 1024-1041.

Magee, C.,Muirhead, J. D.,Karvelas, A.,Holford, S. P.,Jackson, C. A.,Bastow, I. D.,Schofield, N.,Stevenson, C. T.,Mclean, C. & Mccarthy, W. 2016. Lateral magma flow in mafic sill complexes. *Geosphere,* 12**,** 809-841.

Malthe-Sorensson, A.,Planke, S.,Svensen, H. & Jamtveit, B. 2004. Formation of saucer-shaped sills. 215-227.

Martinsen, O. J. & Dreyer, T. 2001. Sedimentary environments offshore norway - palaeozoic to recent: an introduction. *Norwegian Petroleum Society Special Publications,* 10**,** 1-5.

Mathieu, L.,Van Wyk De Vries, B.,Holohan, E. P. & Troll, V. R. 2008. Dykes, cups, saucers and sills: Analogue experiments on magma intrusion into brittle rocks. *Earth and Planetary Science Letters,* 271**,** 1-13.

Mattos, N. H.,Alves, T. M. & Omosanya, K. O. 2016. Crestal fault geometries reveal late halokinesis and collapse of the Samson Dome, Northern Norway: Implications for petroleum systems in the Barents Sea. *Tectonophysics,* 690**,** 76-96.

Mihut, D. & Müller, R. D. 1998. Volcanic margin formation and Mesozoic rift propagators in the Cuvier Abyssal Plain off Western Australia. *Journal of Geophysical Research: Solid Earth,* 103**,** 27135-27149.

Mjelde, R.,Shimamura, H.,Kanazawa, T.,Kodaira, S.,Raum, T. & Shiobara, H. 2003. Crustal lineaments, distribution of lower crustal intrusives and structural evolution of the Vøring Margin, NE Atlantic; new insight from wide-angle seismic models. *Tectonophysics,* 369**,** 199-218.

Mohammedyasin, S.,Lippard, S.,Omosanya, K.,Johansen, S. & Harishidayat, D. 2016. Deep-seated faults and hydrocarbon leakage in the Snøhvit Gas Field, Hammerfest Basin, Southwestern Barents Sea. *Marine and Petroleum Geology,* 77**,** 160-178.

Muraoka, H. & Kamata, H. 1983. Displacement distribution along minor fault traces. *Journal of Structural Geology,* 5**,** 483-495.

NPD 2015. Norwegian Petroleum Directorate FactPages. 1-7.

Omosanya, K.,Johansen, S. & Abrahamson, P. 2016. Magmatic activity during the breakup of Greenland-Eurasia and fluid-flow in Stappen High, SW Barents Sea. *Marine and Petroleum Geology,* 76**,** 397-411.

Omosanya, K. O.,Eruteya, O. E.,Alves, T. M.,Johansen, S. E.,Siregar, E.,Waldmann, N. D. & Zieba, K. J. in press. Three-Dimensional [3-D] seismic imaging of radial faults associated with hydrothermal vent complexes [Vøring Basin, Offshore Norway]. *American Geophysical Union.*

Omosanya, K. O.,Johansen, S. E.,Eruteya, O. E. & Waldmann, N. 2017. Forced folding and complex overburden deformation associated with magmatic intrusion in the Vøring Basin, offshore Norway. *Tectonophysics,* 706–707**,** 14-34.

Osagiede, E. E.,Duffy, O. B.,Jackson, C. a.-L. & Wrona, T. 2014. Quantifying the growth history of seismically imaged normal faults. *Journal of Structural Geology,* 66**,** 382-399.

Planke, S.,Rasmussen, T.,Rey, S. S. & Myklebust, R. 2005. Seismic characteristics and distribution of volcanic intrusions and hydrothermal vent complexes in the Vøring and Møre basins. *Petroleum Geology: North-West Europe and Global Perspectives,* 6**,** 833-844.

Pochat, S.,Castelltort, S.,Van Den Driessche, J.,Besnard, K. & Gumiaux, C. 2004. A simple method of determining sand/shale ratios from seismic analysis of growth faults: An example from upper Oligocene to lower Miocene Niger Delta deposits. *AAPG bulletin,* 88**,** 1357-1367.

Pollard, D. D.,Muller, O. H. & Dockstader, D. R. 1975. The form and growth of fingered sheet intrusions. *Bulletin of the Geological Society of America,* 86**,** 351-363.

Randen, T.,Pedersen, S. I. & Sønneland, L. 2001. Automatic extraction of fault surfaces from three-dimensional seismic data. *SEG Technical Program Expanded Abstracts 2001.* Society of Exploration Geophysicists.

Rateau, R.,Schofield, N. & Smith, M. 2013. The potential role of igneous intrusions on hydrocarbon migration, West of Shetland. *Petroleum Geoscience,* 19**,** 259-272.

Reynolds, P.,Planke, S.,Millett, J. M.,Jerram, D. A.,Trulsvik, M.,Schofield, N. & Myklebust, R. 2017. Hydrothermal vent complexes offshore Northeast Greenland: A potential role in driving the PETM. *Earth and Planetary Science Letters,* 467**,** 72-78.

Rickwood, P. C. 1990. The anatomy of a dyke and the determination of propagation and magma flow directions. *Mafic dykes and emplacement mechanisms; proceedings of the Second international dyke conference,* 2:**,** 81-100.

Riis, F. & Fjeldskaar, W. 1992. On the magnitude of the Late Tertiary and Quaternary erosion and its significance for the uplift of Scandinavia and the Barents Sea. *Structural and Tectonic Modelling and its Application to Petroleum Geology.* Elsevier.

Rohrman, M. 2007. Prospectivity of volcanic basins: Trap delineation and acreage de-risking. *AAPG bulletin,* 91**,** 915-939.

Rowan, M. G.,Jackson, M. P. & Trudgill, B. D. 1999. Salt-related fault families and fault welds in the northern Gulf of Mexico. *AAPG bulletin,* 83**,** 1454-1484.

Schofield, N.,Brown, D. J.,Magee, C. & Stevenson, C. T. 2012. Sill morphology and comparison of brittle and non-brittle emplacement mechanisms. *Journal of Structural Geology,* 169**,** 127-141.

Schofield, N.,Stevenson, C. & Reston, T. 2010. Magma fingers and host rock fluidization in the emplacement of sills. *Geology,* 38**,** 63-66.

Sheriff, R. E. & Geldart, L. P. 1995. Exploration Seismology, Second Edition.

Skogly, O. P. 1998. Seismic characterization and emplacement of intrusives in the Vøring Basin.

Skogseid, J.,Pedersen, T.,Eldholm, O. & Larsen, B. T. 1992a. Tectonism and magmatism during NE Atlantic continental break-up: the Vøring basin. *Magmatism and the Causes of Continental Break-up,* 68**,** 305-320.

Skogseid, J.,Pedersen, T. & Larsen, V. B. 1992b. Voring Basin: subsidence and tectonic evolution. *Structural and tectonic modelling and its application to petroleum geology***,** 55-82.

Smallwood, J. R. & Maresh, J. 2002. The properties, morphology and distribution of igneous sills: modelling, borehole data and 3D seismic from the Faroe-Shetland area. *Geological Society, London, Special Publications,* 197**,** 271-306.

Stewart, S. A. 2006. Implications of passive salt diapir kinematics for reservoir segmentation by radial and concentric faults. *Marine and Petroleum Geology,* 23**,** 843-853.

Svensen, H.,Jamtveit, B.,Planke, S. & Chevallier, L. 2006. Structure and evolution of hydrothermal vent complexes in the Karoo Basin, South Africa. *Journal of the Geological Society,* 163**,** 671-682.

Svensen, H.,Planke, S.,Jamtveit, B. & Pedersen, T. 2003. Seep carbonate formation controlled by hydrothermal vent complexes: A case study from the Vøring Basin, the Norwegian Sea. *Geo-Marine Letters,* 23**,** 351-358.

Swiecicki, T.,Gibbs, P. B.,Farrow, G. E. & Coward, M. P. 1998. A tectonostratigraphic framework for the mid-Norway region. *Marine and Petroleum Geology,* 15**,** 245-276.

Thomson, K. 2007. Determining magma flow in sills, dykes and laccoliths and their implications for sill emplacement mechanisms. *Bulletin of Volcanology,* 70**,** 183-201.

Thomson, K. & Hutton, D. 2004. Geometry and growth of sill complexes: Insights using 3D seismic from the North Rockall Trough. *Bulletin of Volcanology,* 66**,** 364-375.

Thomson, K.,Schofield, N.,Thomson, K. E. N. & Schofield, N. 2008. Lithological and structural controls on the emplacement and morphology of sills in sedimentary basins Lithological and structural controls on the emplacement and morphology of sills in sedimentary basins. 31-44.

Travis, C. J.,Harrison, H.,Hudec, M. R.,Vendeville, B. C.,Peel, F. J. & Perkins, B. F. 1995. Origin of minibasins by multidirectional extension above a spreading lobe of allochthonous salt. *Salt, sediment and hydrocarbons: SEPM Foundation, Gulf Coast Section.* 16th Annual Research Conference Program with Papers.

Valentine, G. A. & Krogh, K. E. 2006. Emplacement of shallow dikes and sills beneath a small basaltic volcanic center–The role of pre-existing structure (Paiute Ridge, southern Nevada, USA). *Earth and Planetary Science Letters,* 246**,** 217-230.

Walker, R. J. 2016. Controls on transgressive sill growth. *Geology,* 44**,** 99-102.

Walsh, J. E. & Timlin, M. S. 2003. Northern Hemisphere sea ice simulations by global climate models. *Polar Research,* 22**,** 75-82.

Walsh, J. J. & Watterson, J. 1989. Displacement gradients on fault surfaces. *Journal of Structural Geology,* 11**,** 307-316.